Time-Frequency Analysis Based on Wavelets for Hamiltonian Systems

Thesis by
Luz Vianey Vela-Arevalo

In Partial Fulfillment of the Requirements
for the Degree of
Doctor of Philosophy

California Institute of Technology
Pasadena, California

2002

(Defended August 14, 2001)

Acknowledgements

I would like to express my gratitude to those who contributed throughout all my years as a graduate student and, particularly, made this thesis possible.

I first would like to greatly thank my advisor Prof. Jerrold E. Marsden, for the most valuable academic and personal advising. His deep and insightful guidance was the best thing any grad student can hope for from an academic advisor. He exceeded by far any obligations that an advisor would have in providing support and I would like to express my gratitude for that.

My deepest thanks to my examination committee members: Emmanuel J. Candes, John Doyle, George Haller, Richard M. Murray and again Jerrold E. Marsden, first for accepting being part of the committee, and mainly for their very helpful and insightful comments during the revisions of the thesis and final defense.

This is a good opportunity to acknowledge the advice of Joaquín Delgado Fernández and Ernesto Pérez Chavela during my undergraduate and master's work in the Universidad Autónoma Metropolitana-Iztapalapa. Thanks to them I became interested in dynamical systems in the first place, and I am very grateful for their guidance and friendship.

I would also like to thank Stephen Wiggins for his guidance in the initial steps of this work. I thank Laurent Wiesenfeld for interesting discussions during the year he spent as a visitor faculty at Caltech. I would like to express my gratitude to Turgay Uzer for numerous and fruitful discussions.

Many people accompanied me during the years I have spent in the CDS department at Caltech. I am very grateful to my friends Monica Giannelli, Alfredo Martinez, Pablo Parrilo, Sergey Pekarsky, Mauricio Barahona, Federico Spedalieri and Fidel Santamaría, with whom I have had unforgettable experiences, and who definitely enriched the academic and many other aspects of my life here. Many thanks to Charmaine Boyd, our department secretary, who made our lives much simpler with her amazing administrative capabilities. I would also like to mention that the Club Latino of Caltech provided a good excuse to work in a different envi-

ronment and meet many people during the time I was its president and organizer of Semana Latina.

I will never express enough gratitude to my parents Elodia and Francisco, my sister Christy, and my brothers Paco and Omahar, for their unconditional love, endless support and inspiration.

And most of all, I want to thank and dedicate this thesis to Thanos. His presence in my life has represented the most important motivation.

My Ph.D. work was supported by the Consejo Nacional de Ciencia y Tecnología (CONACYT, México); the National Science Foundation, and a Special Tuition Award of Caltech.

Time-Frequency Analysis Based on Wavelets for Hamiltonian Systems

by

Luz Vianey Vela-Arevalo

In Partial Fulfillment of the
Requirements for the Degree of
Doctor of Philosophy

Abstract

In this work, we present the method of time-frequency analysis based on wavelets for Hamiltonian systems and demonstrate its applications and consequences in the general dynamics of higher dimensional systems.

By extracting instantaneous frequencies from the wavelet transform of numerical solutions, we can distinguish regular from chaotic motions, and characterize the global structure of the phase space. The method allows us to determine resonance areas that persists even for high energy levels. We can also show how the existence of resonant motion affects the dynamics of the chaotic motion: we detect when chaotic trajectories are temporarily trapped around resonance areas, or undergo transitions between different resonances. This process is a good indicator of intrinsic transport in the phase space.

The method can be applied to a large class of systems, since it is not restricted to nearly integrable systems expressed in action-angle variables, which is the traditional framework for the definition of frequencies.

The main contribution of this method is that we have included the time variable in the analysis. We can determine exactly when the trajectories exchange between different regions by keeping records of resonance trappings. This allows us to analyze chaotic trajectories and not only quasiperiodic trajectories. And, we do not require any assumption about the regularity of chaotic trajectories.

We present three different applications of the method.

The first application consists of the analysis of dynamics and global phase space structure of the classical version of a quantum Hamiltonian for the water molecule. In the second application, we study the planar circular restricted three body problem, and show how resonance transitions of chaotic orbits are related to transport between different regions of the Solar system. Finally, we applied our method to a vibrational three-degrees-of-freedom Hamiltonian of the planar OCS molecule. We study the global dynamics at an energy level close to dissociation, which corresponds to a highly excited state of the molecule.

Contents

List of Figures

List of Tables

Chapter 1

General Introduction

The coexistence of chaos and order is a common feature of nonintegrable Hamiltonian systems. For systems of two degrees of freedom, it is possible to construct a two-dimensional Poincaré map, where commonly we observe islands of quasiperiodic motion surrounded by a chaotic ocean. However, the generalization of this picture beyond two degrees of freedom is far from being understood, in part for the lack of techniques of analysis available; but essentially for the different dynamical features of higher dimensional systems. For instance, in the case of three degrees of freedom, invariant tori are objects of dimension at most three in a five-dimensional energy surface; therefore, they are no more barriers in the phase space.

In this work, we propose a new method of time-frequency analysis based on wavelets. With this method, we generalize the notion of frequency map traditionally defined for completely or nearly integrable Hamiltonian systems. We are able to compute a frequency map for systems that are not nearly-integrable, or that are not given in action-angle coordinates.

The method is based on the extraction of time-varying (instantaneous) frequencies from the wavelet transform of the numerical solutions. With this assignment of frequencies, we are able discern chaotic from regular regions, and determine resonant and non-resonant quasiperiodic trajectories and resonance channels. Furthermore, the good accuracy in the determination of the time-varying frequencies allows us to determine when chaotic trajectories are temporarily trapped in a

resonance, providing a mechanism for intrinsic transport in the phase space.

The method is successfully applied to a large variety of problems, ranging from molecular systems to celestial mechanics. In this work, we present a detailed analysis of two molecules, water and OCS; and the application to a comet capture problem represented by the planar circular restricted three body problem in celestial mechanics.

The computation of frequencies from numerical solutions of dynamical systems has been used as an analytical tool in fields as diverse as galactic dynamics [6, 7], chemical physics [34], celestial mechanics [24] and molecular dynamics [33, 51, 52, 30]. Since the existence of quasiperiodic solutions for integrable and nearly integrable systems is guaranteed by the KAM theorem [4, 8], the approximation of the solutions by (truncated) Fourier series is justified for a large set of trajectories, that is, the quasiperiodic trajectories that remain on Diophantine tori. Therefore, this procedure calls for constructing an approximation of the solutions by trigonometric polynomials in terms of the n basic frequencies of a system of n degrees of freedom.

We have extended this analysis to systems in which highly chaotic dynamics exists next to quasiperiodic trajectories. We use the method of time-frequency analysis based on wavelets to compute the evolution in time of the basic frequencies of the trajectories. This allows us to identify quasiperiodic trajectories with constant frequencies with respect to time; and chaotic trajectories featuring great time-variation of their frequencies.

We will argue that our method has several advantages over other available techniques for higher dimensional systems, specially with respect to the frequency analysis based of the Fourier transform that has been extensively used in Hamiltonian systems.

Technically speaking, the main difference between wavelet and Fourier analyses is the introduction of a time parameter in the wavelet transform. In this way, the wavelet transform produces an expansion over the time-frequency space, unlike the frequency-domain expansion that Fourier analysis yields. Our method takes

advantage of the automatic localization in time and frequency that the wavelets provide, thereby avoiding the "averaged" results that Fourier analysis can give when applied to functions which are not quasiperiodic.

Time-frequency analysis based on wavelets turns out to improve the resolution of the time evolution of the fundamental frequencies when compared with Fourier-based methods. Indeed, our analysis has resulted in a number of surprising findings; e.g., we can observe how chaotic trajectories can be trapped temporarily in a single resonance or in resonance junctions. This is one of our main results.

As a further consequence of the superior accuracy of the time-evolution of the frequencies, we can determine exactly the time interval when a chaotic trajectory is temporarily trapped in a resonance, meaning that the trajectory remains close to a lower dimensional torus during that time-interval. When a resonance transition occurs, the trajectory has evolved from being trapped around one resonant torus to another one, indicating an exchange between different regions of the phase space. We use this fact to explain transport in phase space.

We believe that the main contribution of time-frequency analysis based on wavelets is that chaotic trajectories are included in the analysis besides the quasi-periodic trajectories. In this way, we can provide a detailed description of the global dynamics without any assumptions regarding the measure of the chaotic zones.

1.1 Organization of thesis

The thesis is organized in six chapters. The first chapter is a general introduction where the motivation and main results are presented.

In Chapter 2 we describe the necessary background in the definition of a more general frequency map for Hamiltonian systems. We also present the general theory for definition and extraction of time-varying frequencies and their use in analysis of Hamiltonian systems.

In the three following chapters we present different applications of time-frequen-

cy analysis based on wavelets. In Chapter 3, the classical version of the quantum Hamiltonian of the water molecule is analyzed. This is a three degrees of freedom (dof) system in action angle coordinates, that due to symmetries and a second integral of the motion, can be reduced to 2-dof.

In Chapter 4, the transport mechanism in the planar restricted three body problem is explained in terms of resonance transitions.

In Chapter 5, we describe the phase space dynamics of the 3-dof Hamiltonian for a vibrational model of the OCS molecule, in a highly excited state.

Finally, we present general conclusions, main achievements and future work in Chapter 6.

Chapter 2

Time-Frequency Analysis Based on Wavelets for Hamiltonian Systems

2.1 Introduction

The purpose of this chapter is to describe the use of the wavelet transform in the definition and computation of a frequency map for a more general class of Hamiltonian systems. The main idea of the method is to introduce the time variable in the analysis, and this is done by computing time-varying or *instantaneous* frequencies, extracted from the numerical solutions.

First, in Section 2.2, we recall the definition of the frequency map in completely integrable Hamiltonian systems, since is the traditional framework for the association of frequencies with the quasiperiodic solutions of the system, as a way to characterize the dynamics in phase space. We also describe the theory of quasiperiodic solutions for Hamiltonian system, based on a result by Moser regarding the number of independent frequencies. The frequencies of quasiperiodic solutions can be computed numerically using standard techniques of Fourier analysis, but the treatment of chaotic trajectories requires a different approach. In Section 2.3, we introduce the wavelet transform and its main properties, and describe how it can be used to obtain the time variation of the frequency of a signal. A definition of instantaneous frequency determined as the time derivative of the instantaneous phase of an analytic signal will be discussed in Section 2.4. We also discuss the

applicability of this concept in real signals such as numerical trajectories. The wavelet transform of analytic signals can be used to extract the instantaneous frequency of an analytic signal, this is discussed in Section 2.5. This algorithm is generalized to extract the instantaneous frequency from signals featuring oscillatory behavior. In Section 2.6, we point out that the case of multiple frequency components can be treated in a practical way since the formal definition of instantaneous frequency does not apply. This will be important for Hamiltonian systems in which the coupling between dynamical variables produces the existence of two or more frequencies varying in time. Finally, in Section 2.7, we compare the method of time-frequency analysis based on wavelets with other available methods.

2.2 Frequency map in completely and nearly integrable systems

2.2.1 Definition of the frequency map

The frequency map is traditionally defined in the context of completely integrable Hamiltonian systems, that is, systems for which there is a set of independent integrals of motion which are in involution, and the number of integrals is the same as the number of degrees of freedom. If this is the case, the Liouville-Arnol'd theorem [4, 8] assures that it is formally possible to find a canonical transformation that allows us to express the Hamiltonian system in action-angle variables in each bounded component of the constant energy manifold. Therefore, the frequency map is defined in these regions. Knowledge of the frequency map for such systems is sufficient to completely describe the dynamics.

Consider a completely integrable Hamiltonian system with n degrees of freedom expressed in action-angle coordinates I, θ,

$$H(I, \theta) = H_0(I),$$

where $I = (I_1, I_2, \ldots, I_n)$, $\theta = (\theta_1, \theta_2, \ldots, \theta_n)$.

The equations of motion are given by

$$\begin{aligned} \dot{I}_k &= 0, \\ \dot{\theta}_k &= \frac{\partial H_0}{\partial I_k}(I) =: \omega_k(I). \end{aligned} \tag{2.1}$$

The solutions can be easily obtained as functions of time,

$$\begin{aligned} I_k(t) &= I_k^0, \\ \theta_k(t) &= \omega_k(I^0)t + \theta_k^0, \qquad k = 1, \ldots, n. \end{aligned}$$

Therefore, the motion takes place on a n-dimensional torus parameterized by the vector I_0. The trajectories are quasiperiodic functions in each of the planes of motion, this is, the complex functions

$$z_k(t) = \sqrt{2I_k^0}\, e^{i\,\omega_k(I^0)t+\theta_k^0}$$

are quasiperiodic functions of t.

The frequency map is defined as

$$I \to \omega(I), \tag{2.2}$$

and ω_1, ω_2,..., ω_n are said to be the frequencies of the torus. If the frequency map is invertible, we can use the frequencies ω_k instead of the actions I_k as the coordinates.

The frequencies determine completely the dynamics on the torus: if the frequencies are *non-resonant*, this is, if

$$m_1\omega_1 + m_2\omega_2 + \cdots + m_n\omega_n \neq 0,$$

for all integer numbers m_k, then the motion is quasiperiodic and all trajectories

are dense on the torus. On the other hand, if an equation of the form

$$m_1\omega_1 + m_2\omega_2 + \cdots + m_n\omega_n = 0$$

is satisfied for some integer vector $(m_1, m_2, \ldots, m_n)$ with not all the components zero, then we call the torus *resonant* and in that case the trajectories lie on lower-dimensional tori, the dimension depending on the multiplicity of the resonance; this is, the dimension is the same as the dimension of the frequency module.

The definition of the frequency map (2.2) is basically attached to the representation in action-angle coordinates of a completely integrable system. This idea can be extended to any quasiperiodic solution, since it is possible to extract the frequency vector from any representation of a quasiperiodic solution. This is important since the aim is to construct a frequency map (as in 2.2) independently of the coordinate representation of the system.

The method of frequency analysis calls for reversing the procedure: to extract the frequencies from the solutions, and then to obtain a characterization of the dynamics of the system based on the resonance relations of the frequencies.

Although the extraction of frequencies of quasiperiodic solutions is achieved with standard techniques of Fourier analysis, we will see that the generalization of the procedure to chaotic trajectories is not valid, even in the case of near-integrable systems.

In the following, we discuss the definition of quasiperiodic solutions and the use of Fourier analysis for the extraction of frequencies.

2.2.2 Quasiperiodic solutions

Consider a Hamiltonian system (not necessarily integrable) of n degrees of freedom (n-dof), with Hamiltonian given by

$$H(x, y), \qquad x = (x_1, \ldots, x_n),\ y = (y_1, \ldots, y_n), \tag{2.3}$$

where x and y are general canonical position and momentum coordinates (and not action-angle coordinates). Assume that a quasiperiodic solution is known to exist, and is expressed as a complex variable $z_k(t) = x_k(t) + i\, y_k(t)$, $k = 1, \ldots, n$.

In general, quasiperiodic functions are a special class of almost-periodic functions. A complex function $f(t)$ is almost-periodic if it can be represented in the form

$$f(t) = \sum_{j=0}^{\infty} c^j\, e^{i\,\lambda^j\, t} \tag{2.4}$$

where the coefficients c^j are complex numbers. The numbers λ^j are called the frequencies of f. A vector function $f = (f_1, \cdots, f_n)$ is almost-periodic if all its components are almost periodic.

The sub-class of quasiperiodic functions is characterized by expansions of the form (2.4) but in terms of a finite number of frequencies, i.e., they can be expressed as convergent Fourier series:

$$f(t) = \sum_{m \in Z^n} d^m\, e^{i\, m\cdot\omega\, t},$$

where $m = (m_1, \ldots, m_n)$ is an integer vector, $\omega = (\omega_1, \omega_2, \ldots, \omega_n) \in \mathbb{R}^n$ is called the frequency vector, and $m \cdot \omega = m_1\omega_1 + \cdots + m_n\omega_n$.

Almost-periodic solutions of an n-dof Hamiltonian system (2.3) are in fact quasiperiodic due to a result by Moser [37] showing that the number of basic frequencies is at most n, the number of degrees of freedom. This is a consequence of the exactness of the symplectic form of the Hamiltonian system (see [37] and also [8], p. 125). Quasiperiodic solutions are characterized by the frequency vector, which is also associated to the n-dimensional invariant torus where the quasiperiodic solution lies.

A quasiperiodic solution of (2.3) can therefore be expressed as

$$z_k(t) = \sum_{m \in Z^n} d_k^m\, e^{i\, m\cdot\omega\, t}, \quad k = 1, \ldots, n. \tag{2.5}$$

The frequency vector ω is unique in the sense that, if there is another canonical

coordinate representation x', y' with frequency vector ω', then there is a linear map L such that $\omega = L\omega'$, where L is a constant matrix with integer entries and determinant ± 1 [44].

Therefore, in the approximation of a quasiperiodic solution of (2.3) as

$$z_k(t) \approx \sum_{j=0}^{p} c_k^j \, e^{i\,\lambda_k^j\, t}, \quad k = 1, \ldots, n, \tag{2.6}$$

the numbers λ_k^j are integer linear combinations of the components of the frequency vector $(\omega_1, \ldots, \omega_n)$.

The computation of λ_k^j can be achieved using techniques of Fourier analysis, and from them we can extract the basic frequencies $\omega_1, \ldots, \omega_n$ and provide an approximation of the solutions of the form (2.5). Once we know the frequencies associated to a particular quasiperiodic torus, we can describe the motion on the torus as resonant or non-resonant.

2.2.3 Computation of the frequency map in near integrable systems using Fourier analysis

The procedure described above can be used for completely integrable systems, where all the bounded solutions are known to be quasiperiodic, and hence, Fourier analysis techniques apply. We can proceed in the same way for nearly integrable systems (this is, when a small perturbation is added), since the KAM theorem ensures the existence of quasiperiodic trajectories lying on slightly deformed invariant tori with the same frequency vectors as in the unperturbed Hamiltonian, provided that Diophantine and non-degeneracy conditions are satisfied [1, 2, 8].

Laskar's frequency analysis [25, 27, 26] provides an efficient algorithm for this case, by extending the Fourier basis to a more general set of complex exponentials. He proved that his method for approximating quasiperiodic solutions of nearly integrable systems provides the exact value of the frequencies with a certain convergence rate.

The use of Fourier analysis to approximate trajectories as in Equation (2.6)

relies heavily on the fact that for systems that are integrable or near-integrable, there are many quasiperiodic trajectories for which the frequencies are well defined. An immediate concern is the treatment of chaotic trajectories generated by the perturbation. The generalization of the procedure to chaotic trajectories is frequently expressed as a negative statement: if we cannot assign frequencies to a particular solution, then the trajectory is deemed chaotic.

A common argument of Laskar [25], and Martens *et al.* [33], to justify the use of Fourier analysis in the case of chaotic trajectories is that for near-integrable systems, the behavior of its chaotic solutions is "regular enough" when viewed in short intervals of time. They assume that chaotic trajectories are close to quasiperiodic locally, but this cannot be justified. The method we propose disregards this assumption.

2.3 Time-frequency analysis based on wavelets

As seen in Section 2.2, Fourier methods are justified for completely integrable systems, and even allows one to examine the behavior of many solutions of nearly integrable systems. However, chaotic trajectories in a very large class of non-integrable systems cannot be adequately examined.

Our main interest is to generalize the assignment of frequencies to solutions of Hamiltonian systems that feature oscillatory behavior. Although Fourier analysis provides a frequency representation of a time dependent signal, all Fourier methods require that the signal is periodic or quasiperiodic. Furthermore, this frequency representation does not reflect at all any change in time of the spectral information of the function. Therefore, frequency analysis based on the Fourier transform does not apply for systems that are not near integrable, even in principle.

We will present a new method to define a frequency map for a much larger class of Hamiltonian systems. One of the key points in achieving this is developing the concept of time-varying or *instantaneous frequency*. With the assignment of time-varying frequencies we are able to extend the frequency map analysis to

Hamiltonian systems that are not nearly integrable, or that are not given in action-angle coordinates.

Advantages. The method we propose is time-frequency analysis based on wavelets. We compute the instantaneous frequency associated with time series representing numerical solutions of the Hamiltonian system, producing the frequency evolution of the dynamical variables in the system. This will allow us to differentiate between regular and chaotic trajectories, since for quasiperiodic trajectories the frequencies are constant and coincide with the Fourier frequency. We can also identify resonance channels due to the good accuracy in the assignments of frequencies. Furthermore, the time evolution of the frequencies allows us to detect temporary resonance trapping of chaotic trajectories and their implications in transport in the phase space.

This methodology is inclusive, meaning that it can be applied on problems where Fourier methods apply, together with strongly chaotic systems.

2.3.1 Wavelet transform

An ideal method for analyzing functions that have time-varying frequencies is the *wavelet transform* [12]. The wavelet transform by design provides good localization in both time and frequency. With this new methodology we will be able to define a frequency map for a large class of Hamiltonian systems, by the assignment of instantaneous frequencies to the trajectories.

The wavelet transform is defined in terms of a function ψ, called the *mother wavelet*, as

$$L_\psi f(a,b) = \frac{1}{\sqrt{a}} \int_{-\infty}^{\infty} f(t)\overline{\psi}\left(\frac{t-b}{a}\right) dt. \tag{2.7}$$

The function $\psi \in L^2(I\!R)$ must satisfy the admissibility condition $0 < c_\psi = 2\pi \int_{-\infty}^{\infty} \frac{|\widehat{\psi}(\omega)|^2}{|\omega|} d\omega < \infty$, where $\widehat{\psi}$ is the Fourier transform of ψ; to be useful the mother wavelet must have compact support or decay rapidly to 0 for $t \to \infty$ and $t \to -\infty$.

The wavelet transform depends on two parameters: a is called the scale, and b

is the time parameter. The wavelet transform can be viewed as a time-frequency representation of a signal f in the following sense: If the wavelet ψ has compact support, the parameter b shifts the wavelets so that the local information of f around the time $t = b$ is contained in $L_\psi f(a, b)$; the scale parameter a is proportional to the inverse of the frequency; therefore, $L_\psi f(a, b)$ gives the frequency content of f over a small interval of time around $t = b$.

The wavelet transform (2.7) produces a complex surface as a function of the variables a and b. A common representation of this surface is a density plot of the modulus of $L_\psi f(a, b)$, with b as the horizontal axis (time) and $ln(a)$ as the vertical axis. However, since the frequency is proportional to the inverse of the scale $(1/a)$, we opted for the frequency ω as the vertical axis.

2.3.2 A first example: the chirp

For motivation, and to show the capability of the wavelet transform to yield the variation in time of the frequency, consider the example given by a chirp; this is, a function with "increasing frequency." In Figure 2.1 we present such example. In part a), the real part of a function with increasing frequency is represented, and in b) is the density plot of the modulus of its wavelet transform. We note that the density plot is "concentrated" or has the maximum along the line that corresponds to the time-varying frequency; this region is called the ridge of the wavelet transform.

In part c) of Figure 2.1, we plotted the frequency producing the maximum modulus as a function of time, and we observe that it coincides with the line that we expect to be the instantaneous frequency. Note that there is some discrepancy at the beginning and at the end of the time interval studied. This is caused by the finite interval considered in the analysis; this is, in the beginning and end of evolution, we do not possess enough information of the signal to perform the analysis. This is a normal limitation due to the finite time analysis.

We note also that the ridge of the wavelet transform (in Figure 2.1 b) has a larger spread as the frequency increases. This is caused by the constant area of the

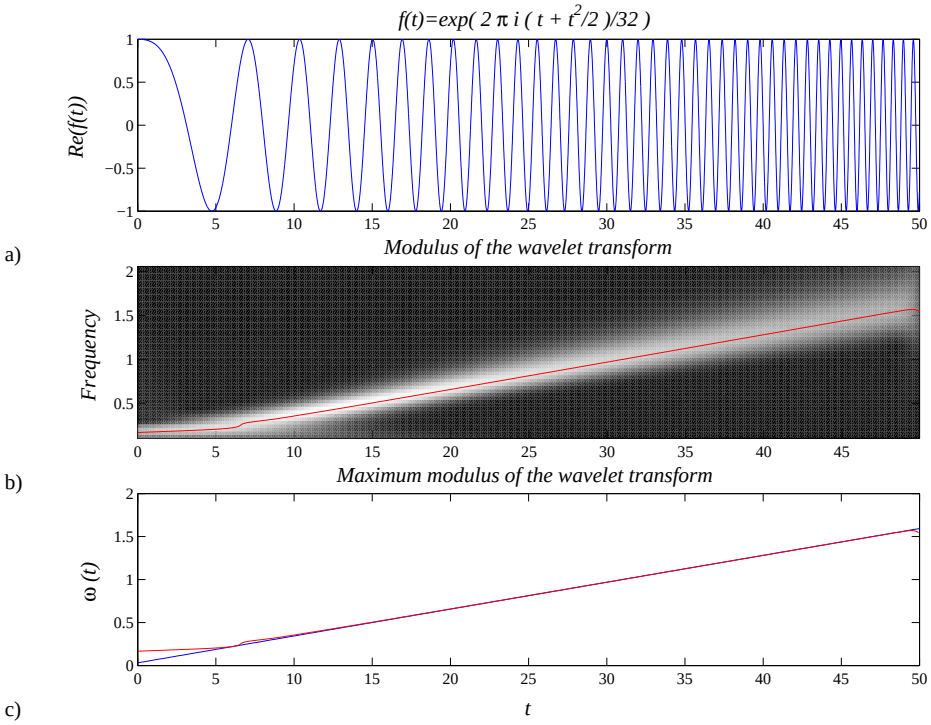

Figure 2.1: Density plot of the modulus of the wavelet transform of a function with linearly increasing frequency. Note that the ridge of the wavelet transform goes along the instantaneous frequency.

time-frequency window in which the wavelet transform localizes the signal. Since our physical systems have bounded frequencies, this does not represent a problem in our analysis. This characteristic of the wavelet transform is reminiscent of the Heisenberg uncertainty principle: The localization in both time and frequency is limited. (See for instance [19]).

In the following, we describe the main properties of the wavelet transform in order to establish its convenience for time-frequency localization.

Zoom-in and zoom-out capabilities of the wavelet transform. We want to consider local information of f in time intervals that yield spectral information on any desirable range of frequencies (or frequency band). For high frequency the time interval should be small; for low frequency the time interval should be

wide. The wavelet transform possesses this property, called the "zoom-in" and "zoom-out" capabilities. This fact will be clear from the determination of the time window and frequency window on which the wavelet transform is localized; for this we need to introduce some concepts.

The center and radius of the wavelet are defined (respectively) by

$$t^* = \frac{1}{||\psi||_2^2}\int_{-\infty}^{\infty} x|\psi(x)|^2 dx, \quad \text{and} \quad \Delta_\psi = \frac{1}{||\psi||_2}\left(\int_{-\infty}^{\infty}(x-t^*)^2|\psi(x)|^2 dx\right)^{1/2}.$$

Assume ψ and its Fourier transform $\widehat{\psi}$ are wavelets, with centers and radius $t^*, \omega^*, \Delta_\psi, \Delta_{\widehat{\psi}}$. Then, the wavelet transform 2.7 localizes the function within a time window of the form

$$A = [b + at^* - a\Delta_\psi \ , \ b + at^* + a\Delta_\psi].$$

Since the value of the frequency is proportional to $1/a$, the time window automatically narrows for high frequency (a small) and widens for low frequency (a large); these are the zoom-in and zoom-out capabilities that we mentioned above.

Now, let $\eta(\omega) = \widehat{\psi}(\omega + \omega^*)$, the center of η is 0 and its radius is $\Delta_{\widehat{\psi}}$. Using Parseval's identity, we obtain that

$$L_\psi f(a,b) = \frac{\sqrt{a}}{2\pi}\int_{-\infty}^{\infty}\widehat{f}(t)e^{i\omega b}\overline{\eta}\left(a(\omega - \frac{\omega^*}{a})\right)d\omega,$$

then the same quantity $L_\psi f(a,b)$ gives localized information of the spectrum $\widehat{f}(\omega)$ within a frequency window

$$B = \left[\frac{\omega^*}{a} - \frac{\Delta_{\widehat{\psi}}}{a} \ , \ \frac{\omega^*}{a} + \frac{\Delta_{\widehat{\psi}}}{a}\right],$$

(with the exception of multiplication by $\sqrt{a}/2\pi$ and a linear phase shift $e^{i\omega b}$). Therefore, $L_\psi f(a,b)$ localizes f in the time-frequency window $A \times B$.

Morlet-Grossman wavelet. The mother wavelet that we use throughout this work is the Morlet-Grossman wavelet [9], given by

$$\psi(t) = \frac{1}{\sigma\sqrt{2\pi}}\, e^{2\pi i\lambda t}\, e^{-t^2/2\sigma^2}.$$

The parameters λ and σ can be tuned to improve the resolution. This wavelet proved to be convenient for our computations, although the analysis can be done with other wavelets as well.

The simplest case. Consider a periodic function $f(t) = e^{i2\pi\omega_0 t}$, for which the wavelet transform can be obtained analytically as

$$\begin{aligned} L_\psi f(a,b) &= \frac{1}{\sqrt{a}} \int_{-\infty}^{\infty} e^{i2\pi\omega_0 t}\, \overline{\psi}\left(\frac{t-b}{a}\right) dt \\ &= \sqrt{a} \int_{-\infty}^{\infty} e^{i2\pi\omega_0 as}\, e^{i2\pi\omega_0 b} \overline{\psi}(s) ds \\ &= \sqrt{a}\, e^{i2\pi\omega_0 b}\, \overline{\widehat{\psi}}(\omega_0 a), \end{aligned}$$

where $\widehat{\psi}$ is the Fourier transform of ψ. As we should expect the modulus of $L_\psi f(a,b)$ depends only on the scale a, and it is independent of the time variable b.

Particularly for the Morlet-Grossman wavelet, the modulus of this transform is given by

$$\eta(a) = |L_\psi f(a,b)| = \sqrt{a}\, \overline{\widehat{\psi}}(\omega_0 a),$$

with $\widehat{\psi}(\omega) = e^{-2\pi^2\sigma^2(\omega-\lambda)^2}$. $\eta(a)$ has a global maximum, in other words, $\widehat{\psi}$ is well localized in frequency. The maximum is at $a\omega_0 = \frac{1}{2}\left(\lambda + \sqrt{\lambda^2 + \frac{1}{2\pi^2\sigma^2}}\right)$. Therefore, we can define the frequency variable (for the Morlet-Grossman wavelet) as

$$\omega = \frac{1}{2\,a}\left(\lambda + \sqrt{\lambda^2 + \frac{1}{2\pi^2\sigma^2}}\right), \tag{2.8}$$

and the value of the frequency ω_0 can be recovered from the scale a that maximizes the modulus of the wavelet transform. We will see below that this procedure can

be extended for functions that feature time-variation in frequency.

In the following, we will discuss the definition of instantaneous frequency and related concepts, and how they can be use to define a more general frequency map for Hamiltonian systems.

2.4 Instantaneous frequency

We want to use a definition of time-varying or instantaneous frequency that agrees with the intuitive notion of frequency as the "oscillation rate." This definition must agree with the usual notion of Fourier frequency for signals with constant amplitude and frequency. In this way, periodic and quasiperiodic functions will retain their constant frequencies in the new analysis, and the frequency map will coincide with (2.2) for completely and nearly integrable Hamiltonian systems expressed in action-angle variables. Of the available definitions for instantaneous frequency, the one that satisfies this condition is based on the concept of *analytic signal*.

Assume that a complex function $f(t)$ can be represented as a complex exponential with varying amplitude and phase,

$$f(t) = A(t)\, e^{i\,\phi(t)}. \tag{2.9}$$

Our intuition suggests that the frequency is given by time derivative of the phase:

$$\omega(t) = \frac{1}{2\pi}\phi'(t).$$

(From now on we adopt the convention of the factor 2π in the definition of frequency). However, the representation (2.9) is not unique. To illustrate this with a simple example, consider

$$f(t) = A(t)\cos(t),$$

where $A(t)$ is a bounded function. This is a function that oscillates as $\cos(t)$ inside the "envelope" given by the variable amplitude $A(t)$. Let $\tilde{A} = \sup|A(t)|$ and define

the new function

$$\tilde{f}(t) = (1/\tilde{A})f(t).$$

Since $|\tilde{f}(t)| \leq 1$, we can find $\tilde{\phi}$ such that $\tilde{f}(t) = \cos(\tilde{\phi}(t))$. Therefore,

$$f(t) = \tilde{A}\cos(\tilde{\phi}(t))$$

is another representation of f which would have a different frequency.

The instantaneous frequency cannot be obtained from a particular representation. We need to find a definition of instantaneous frequency that can be uniquely determined and that also corresponds to our physical intuition. Vakman [48] imposed three conditions that instantaneous amplitude, phase and frequency should satisfy:

a) The amplitude is continuous and differentiable. This means that if the original function f changes slightly in amplitude, then the instantaneous amplitude should increase or decrease accordingly.

b) The phase is independent of scaling, and the amplitude is homogeneous; this is, if $f(t)$ is replaced by $cf(t)$, then the frequency does not change and the amplitude is scaled by c.

c) The constant amplitude and frequency of a simple sinusoid should retain their values.

Other authors have added new conditions, for instance Loughlin and Tracer [31] proposed that *i*) the instantaneous amplitude of bounded functions should be bounded, and *ii*) if the signal has bounded Fourier spectrum, the instantaneous frequency should have the same bounds.

There have been several attempts to define variable amplitude, phase and frequency, some satisfying these conditions, and the discussion about their convenience has been long. We refer the reader to [40] and references therein.

2.4.1 Analytic signals

The most common definition of instantaneous frequency involves the concept of *analytic signal*, introduced by Gabor [18] and Ville [50]. This definition includes the notion of Fourier frequency for periodic or quasiperiodic signals. The concept of analytic signal is based on the Hilbert transform.

Definition 1 *A function $f(t) = u(t) + i\,\nu(t)$, expressed in terms of its real and imaginary parts, is an* analytic signal *if*

$$\nu(t) = H\,u(t),$$

where

$$H\,u(t) = -\frac{1}{\pi}\mathrm{P}\int_{-\infty}^{\infty}\frac{u(\eta)}{\eta - t}d\eta \tag{2.10}$$

is the Hilbert transform of $u(t)$. P denotes the Cauchy principal value integral. We also say that u and ν form a Hilbert pair. The inverse of the Hilbert transform is given by

$$u(t) = H^{-1}\,\nu(t) = \frac{1}{\pi}\mathrm{P}\int_{-\infty}^{\infty}\frac{\nu(\eta)}{\eta - t}d\eta. \tag{2.11}$$

We also say that the analytic signal associated to a real function $u(t)$ is $u(t) + i\,Hu(t)$.

The following theorem provides three possible characterizations of analytic signals.

Theorem 1 *Let $f(t) = u(t) + i\,\nu(t)$ be a piecewise continuous function with piecewise continuous derivative in any finite interval. Also, suppose $f \in L^1(\mathbb{R})$, and that f is bounded by decaying exponentials. The following are equivalent:*

1. *f is an analytic signal; i.e., $\nu(t) = H\,u(t)$.*
2. *The Fourier transform of f is one sided, i.e., it satisfies*

$$\widehat{f}(\xi) = \mathrm{F}f(\xi) = 0, \text{ for } \xi < 0.$$

3. *f is obtained as the restriction to the real axis of a complex function $f(t+i\,\tau)$ that is analytic for $\tau \geq 0$; this is, $f(t+i\,\tau) = u(t,\tau) + i\,\nu(t,\tau)$ is analytic in the complex upper half plane, and the signal satisfies*

$$f(t) = u(t,0) + i\,\nu(t,0), \quad t \in \mathbb{R}.$$

The proof of this theorem contains a review of the mathematical concepts involved in the definition of instantaneous frequency, and can be found in the Appendix A.1.

The concept of analytic signal is useful to define instantaneous frequency since for analytic functions the real and imaginary parts are uniquely defined; therefore, we are able to define the instantaneous phase and frequency in a unique way.

Definition 2 *Let $f(t) = u(t) + i\,\nu(t)$ be an analytic signal, where u and ν are the real and imaginary parts respectively. The instantaneous phase of f is defined by*

$$\phi(t) = \text{Arctan}\frac{\nu(t)}{u(t)},$$

and the instantaneous frequency is the time derivative of the phase:

$$\omega(t) = \frac{1}{2\pi}\phi'(t).$$

Identification of analytic signals. To determine if a function $f(t) = u(t) + i\,\nu(t)$ is an analytic signal is not an easy task. Theorem 1 gives three possible characterizations of analytic signals; however, they are hard to use in practice and the analysis must be done numerically in most cases.

In general, functions arising from solutions of differential equations are not analytic signals. Most Hamiltonian systems have solutions that are not analytic in the upper half plane even if the Hamiltonian is analytic. Consider for instance the one-degree-of-freedom pendulum, which is of course integrable; its solutions can be expressed explicitly in terms of inverse elliptic functions that have a lattice of singularities in the complex plane.

Among the few results about completeness of Hamiltonian systems in $\mathbb{C}^n$,

Forstneric [16] has shown that the only Hamiltonian system in $\mathbb{C}^2$ of the form

$$H(z_1, z_2) = \frac{1}{2}z_2^2 + Q(z_1) \tag{2.12}$$

that has analytic solutions in the entire complex plane is for Q quadratic. That is, if Q is not a quadratic function, every regular level set of (2.12) contains a point that flows to infinity in finite (complex) time.

In practical terms, the restriction of having a function of real time that has an analytic continuation to the upper half plane without any singularity is very strong.

The following examples illustrate some cases when analytic signals can be determined, and characterizations according to the definition or their spectral properties.

Example 1. A trivial example of an analytic signal is the function $f(t) = \exp(i\,2\pi\omega_0 t)$. To see this, note that the Fourier transform is one sided: $\mathrm{F}[f](\xi) = \delta(\omega_0 - \xi)$; therefore, the imaginary part is the Hilbert transform of the real part,

$$H[\cos(2\pi\omega_0 t)] = \sin(2\pi\omega_0 t) \quad \text{and} \quad H^{-1}[\sin(2\pi\omega_0 t)] = \cos(2\pi\omega_0 t),$$

and of course, the instantaneous frequency is ω_0.

This example shows that the definition of instantaneous frequency by means of analytic signals coincides with the definition of Fourier frequency for the case of constant frequencies. It is also clear that the Hilbert transform is linear and homogeneous, and that the instantaneous phase and frequency are independent of scaling. Therefore, this definition of instantaneous frequency satisfies the three conditions mentioned in the beginning of Section 2.4.

Example 2. $u(t)$ and $\dot{u}(t)$ (the derivative of u with respect to t) are not a Hilbert pair; i.e., $f(t) = u(t) + i\,\dot{u}(t)$ is not an analytic signal. To see this, consider the

Fourier transform of f,

$$\mathrm{F}[f](\xi) = \widehat{u}(\xi) + i\,\widehat{\tilde{u}}(\xi) = \widehat{u}(\xi) + i\,(2\pi i\xi)\widehat{u}(\xi) = (1 - 2\pi\xi)\widehat{u}(\xi),$$

which is not one sided due to the fact that $u(t)$ is real and then its Fourier transform satisfies $\widehat{u}(-\xi) = \overline{\widehat{u}}(\xi)$.

Example 3. Consider a function of the form $A(t)\exp(2\pi i\omega_0 t)$ with $A(t) \geq 0$. There is no *a priori* reason for this function to be an analytic signal. If this were the case, then we should have that

$$H[A(t)\cos(2\pi\omega_0 t)] = A(t)\sin(2\pi\omega_0 t) = A(t)H[\cos(2\pi\omega_0 t)].$$

Let $\widehat{A}(\xi)$ be the Fourier transform of A, then

$$\mathrm{F}[A(t)\exp(2\pi i\omega_0 t)] = \widehat{A}(\xi - \omega_0);$$

therefore, $A(t)\exp(2\pi i\omega_0 t)$ is an analytic signal if and only if $\widehat{A}(\xi) = 0$ for $|\xi| > \omega_0$.

This example can be seen as an application of the Bedrosian's theorem that we enunciate in the following (for a proof see [21], p. 88).

Bedrosian's Theorem. Let $f, g \in L^1(\mathbb{R})$, such that $\widehat{f}, \widehat{g} \in L^1(\mathbb{R})$ and

$$\widehat{f}(\xi) = 0, \quad \text{if } |\xi| > \xi_0,$$
$$\widehat{g}(\xi) = 0, \quad \text{if } |\xi| \leq \xi_0,$$

then $H[f(t)g(t)] = f(t)H[g(t)]$.

Consider again the function $A(t)\cos(2\pi\omega_0 t)$. If $\widehat{A}(\xi)$ vanishes for $|\xi| > \omega_0$, we can apply the Bedrosian's theorem to obtain that

$$H\left[A(t)\cos(2\pi\omega_0 t)\right] = A(t)H\left[\cos(2\pi\omega_0 t)\right] = A(t)\sin(2\pi\omega_0 t),$$

as we saw before.

Example 4. Bedrosian's theorem gives the conditions on the Fourier transforms of $A(t)$ and $\cos[\phi(t)]$ for which is valid

$$H[A(t)\cos\phi(t)] = A(t)H[\cos\phi(t)].$$

However, it is not clear that it should be $H[\cos\phi(t)] = \sin\phi(t)$. In general this is not the case, an example is the following (taken from [40]):

Consider

$$x(t) = \frac{\sin(2\pi Bt)}{2\pi Bt}\cos(2\pi\omega_0 t),$$

where $\omega_0 > B$. Since $|x(t)| \leq 1$, it is possible to introduce a function $\phi(t)$ uniquely defined such that $0 \leq \phi(t) \leq \pi$ and

$$x(t) = \cos\phi(t).$$

If it were true that $H[\cos\phi(t)] = \sin\phi(t)$, then we should have

$$[x(t)]^2 + [H\,x(t)]^2 = 1.$$

We will see that this is false. Since the Fourier transform of $\sin(2\pi Bt)/(2\pi Bt)$ is zero for $|\xi| > B$, we can apply Bedrosian's theorem to get

$$H\,x(t) = \frac{\sin(2\pi Bt)}{2\pi Bt}H[\cos(2\pi\omega_0 t)] = \frac{\sin(2\pi Bt)}{2\pi Bt}\sin(2\pi\omega_0 t),$$

and then

$$[x(t)]^2 + [H\,x(t)]^2 = \left(\frac{\sin(2\pi Bt)}{2\pi Bt}\right)^2.$$

Example 5. We can apply the Bedrosian's theorem to compute the Hilbert transform of $A(t)\cos(2\pi\omega_0 t + \phi_0)$ only if the Fourier transform of $A(t)$ vanishes for $|\xi| \geq \omega_0$. Its analytic signal is in this case $A(t)\exp(i2\pi\omega_0 t + \phi_0)$. In general the spectrum $\widehat{A}(\xi)$ exists for both $\xi < \omega_0$ and $\xi > \omega_0$; therefore, Bedrosian's theorem

does not apply directly.

An asymptotic result can be obtained for ω_0 large [21]. When $\omega_0 \to \infty$ we have that

$$H[A(t)\cos(2\pi\omega_0 t + \phi_0)] = A(t)\sin(2\pi\omega_0 t + \phi_0)$$

for almost every t.

Example 6. As we mentioned before, is not true in general that $H[\cos(\phi(t))] = \sin(\phi(t))$. If the function $\exp[i\phi(t)]$ is an analytic signal, $\phi(t)$ must have the following form [40]:

$$\phi(t) = \theta + \omega_0 t + \phi_b(t),$$

where θ is arbitrary, $\omega_0 \geq 0$ and $\phi_b(t)$ is the argument of a Blaschke function $b(t)$,

$$b(t) = \prod_{k=1}^{N} \frac{t - z_k}{t - \overline{z}_k}, \qquad Im(z_k) > 0;$$

i.e., $\phi(t)$ is the argument of a function of modulus 1 that has all its poles in the lower half complex plane.

A function with constant amplitude $c\exp[i\phi(t)]$ is an analytic signal only if $\phi(t)$ takes this particular form. This strong condition is very difficult to satisfy. In general, we should expect that analytic signals have the form $A(t)\exp[i\phi(t)]$.

2.4.2 Asymptotic analytic signal

We have seen that the concept of analytic signal is very restrictive. In practice, we deal with functions that are close to an analytic signal. Delprat *et al.* [13] introduced the concept of asymptotic analytic signal.

Vaguely, a function $u(t) = A(t)\cos(\phi(t))$ is called asymptotic analytic signal if its analytic signal associated,

$$Z_u(t) = u(t) + i\,H[u(t)],$$

is close to $A(t)\exp\left[i\phi(t)\right]$.

The following lemma shows that a function is an asymptotic analytic signal if the oscillations due to the term $\cos[\phi(t)]$ are much more important than the variations of the modulus $A(t)$. The proof can be found in the Appendix A.3, and it follows from the computation of the Hilbert transform using the stationary phase method (see Appendix A.2).

Lemma 1 *Given $u(t) = A(t)\cos[\lambda\phi(t)]$ with λ large, the analytic signal associated $Z_u(t) = [I + i\,H]u(t)$ satisfies*

$$Z_u(t) = A(t)\exp[i\lambda\phi(t)] + O(\lambda^{-3/2}).$$

This result is used in practice rather loosely, since in general there is not a parameter λ controlling the rate of oscillation. However, we expect that functions with oscillatory behavior with a representation $A(t)\exp[i\lambda\phi(t)]$ are close enough to an analytic signal in such a way that the definition of instantaneous frequency applies.

2.5 Instantaneous frequency and the wavelet transform

In the previous Section, we reviewed the definition of instantaneous frequency for analytic signals, and the difficulties to use it in practice since in general we deal with functions that are only close to an analytic signal.

In this Section, we study the relation of the wavelet transform with instantaneous frequency of an analytic signal, and generalize this procedure towards numerical algorithms that allow us to extract time-varying frequencies.

All the arguments follow closely [13] and [9], and are explained here for completeness.

The wavelet transform of f provides the expansion of a function f in terms of basis functions ψ_{ab} that are constructed as dilations and translations of the mother

wavelet ψ:

$$\psi_{ab}(t) = \frac{1}{\sqrt{a}}\psi\left(\frac{t-b}{a}\right), \quad b \in \mathbb{R}, \quad a > 0.$$

The coefficients of this expansion are given by the wavelet transform of f,

$$L_\psi f(a,b) \;=\; \langle f, \psi_{ab}\rangle \;=\; \frac{1}{\sqrt{a}}\int_{-\infty}^{\infty} f(t)\overline{\psi}\left(\frac{t-b}{a}\right)dt.$$

Let $f(t) = A_f(t)\exp[i\,\phi_f(t)]$ be an analytic signal. If the wavelet ψ is an analytic signal itself, and it is written in the form

$$\psi(t) = A_\psi(t)\exp[i\phi_\psi(t)],$$

then the wavelet transform coefficients can be computed as

$$L_\psi f(a,b) = \frac{1}{\sqrt{a}}\int_{-\infty}^{\infty} M_{ab}(t)\exp[i\Phi_{ab}(t)]dt, \tag{2.13}$$

where

$$M_{ab} = A_f(t)A_\psi\left(\frac{t-b}{a}\right),$$
$$\Phi_{ab}(t) = \phi_f(t) - \phi_\psi\left(\frac{t-b}{a}\right).$$

In order to obtain an asymptotic expression for the integral in Equation (2.13), we note that if the integrand oscillates greatly due to the term $\exp[i\Phi_{ab}(t)]$, then the function $M_{ab}(t)$ appears as constant and the contributions of successive oscillations effectively cancel. However, if the phase $\Phi_{ab}(t)$ is constant, i.e., there is a stationary point, this effect is reduced. Therefore, the coefficients of the wavelet transform will "concentrate" around the stationary points.

Let t_0 be a unique point such that $\Phi'_{ab}(t_0) = 0$ and $\Phi''_{ab}(t_0) \neq 0$. t_0 is called a stationary point. We can apply the method of stationary phase (see Appendix

A.2) to obtain the expression,

$$L_\psi f(a,b) \approx \frac{1}{\sqrt{a}} f(t_0)\overline{\psi}\left(\frac{t_0-b}{a}\right)\sqrt{\frac{2\pi}{|\Phi''_{ab}(t_0)|}}\, e^{i\,\mathrm{sgn}\Phi''_{ab}(t_0)\pi/4}. \tag{2.14}$$

Note: $t_0 = t_0(a,b)$. Then the equation $t_0(a,b) = b$ gives a curve in the time-scale plane. This leads to the following definition:

Definition 3 *The ridge of the wavelet transform is the collection of points for which* $t_0(a,b) = b$.

From the equation $\Phi'_{ab}(t_0) = 0$, we have that

$$\Phi'_{ab}(t_0) = \phi'_f(t_0) - \frac{1}{a}\phi'_\psi\left(\frac{t_0-b}{a}\right) = 0, \tag{2.15}$$

and then, by definition, the points on the ridge satisfy

$$a =: a_r(b) = \frac{\phi'_\psi(0)}{\phi'_f(b)}.$$

Therefore, the instantaneous frequency $\phi'_f(b)$ of the function f can be obtained from this equation once we have determined the ridge of the wavelet transform.

2.5.1 Extraction of the ridge of the wavelet transform

(*i*) From the modulus of the wavelet transform. In Figure 2.1 we showed with an example that the modulus wavelet transform has a maximum along the ridge. The ridge of the wavelet transform can be obtained by computing the maximum modulus of the wavelet transform (with respect to scale) for each point in time. Therefore, the maximum in scale for each time $t = b$ corresponds to the instantaneous frequency of f, using the relation (2.8) (or an analogous one if a different mother wavelet is used).

The pseudocode of the numerical algorithm for this approach can be found in the Appendix A.4.

***(ii)* From the phase of the wavelet transform.** Delprat *et al.* [13] described an algorithm is to extract the ridges from the phase of the wavelet transform. This is explained in the following:

Define the phase of the wavelet transform of f (2.13) as

$$\Psi(a,b) = \mathrm{Arg}(L_\psi f(a,b)).$$

From the asymptotic approximation in (2.14), we obtain

$$\Psi(a,b) \approx \Phi_{ab}(t_0) \pm \frac{\pi}{4}.$$

Note that, from the definition of the ridge of the wavelet transform, $t_0 = t_0(a,b)$, i.e., $\Phi_{ab}(t_0)$ is a function of the variables a and b. Then, computing the partial derivative with respect to b we have

$$\begin{aligned}
\frac{\partial \Psi}{\partial b} \approx & \frac{\partial \Phi_{ab}}{\partial b} \\
= & \frac{\partial}{\partial b}\left\{\phi_f(t_0(a,b)) - \phi_\psi\left(\frac{t_0(a,b)-b}{a}\right)\right\} \\
= & \phi_f'(t_0)\frac{\partial t_0}{\partial b} - \phi_\psi'\left(\frac{t_0-b}{a}\right)\left(\frac{\frac{\partial t_0}{\partial b}-1}{a}\right) \\
= & \left[\phi_f'(t_0) - \frac{1}{a}\phi_\psi'\left(\frac{t_0-b}{a}\right)\right]\frac{\partial t_0}{\partial b} + \frac{1}{a}\phi_\psi'\left(\frac{t_0-b}{a}\right) \\
= & \frac{1}{a}\phi_\psi'\left(\frac{t_0-b}{a}\right).
\end{aligned}$$

(In the last step, the quantity in brackets is equal to zero due to Equation (2.15)).

Evaluating at $b = b_0$ (and then $t_0(a,b_0) = b_0$) we obtain

$$\begin{aligned}
\left.\frac{\partial \Psi}{\partial b}\right|_{b=b_0} \approx & \frac{1}{a}\phi_\psi'\left(\frac{t_0-b_0}{a}\right) \\
= & \frac{1}{a}\phi_\psi'(0).
\end{aligned}$$

This equation provides an algorithm to extract the scale $a_r(b_0)$ that solves the ridge equation $t_0(a_r(b_0), b_0) = b_0$, for each time-value b_0. The algorithm consists of finding the fixed point a that solves the equation

$$a = \frac{\phi'_\psi(0)}{\partial_b \Psi(a, b)},$$

for each b fixed. Therefore, given an initial approximation a^0, we can produce a sequence of points $a^{j+1} = \frac{\phi'_\psi(0)}{\partial_b \Psi(a^j, b)}$ that converges to the solution a^*.

In this work we use a combination of the two approaches discussed above: the initial approximation is obtained from the maximum modulus of the wavelet transform evaluated on a series of test-frequencies, and then we use the fixed point algorithm to obtain an exact value of the frequency at each time.

2.6 Two or more frequency components

The definition of instantaneous frequency using the analytic signal has a physical meaning only for signals that have a single frequency component varying in time (monochromatic). Although it seems intuitively plausible to consider functions with more than one frequency component varying in time, the definition of instantaneous frequency is an ill posed problem in this case, as it has been pointed out often (see for instance [53]). In the case of two components $f(t) = a_1 \exp i\,\phi_1(t) + a_2 \exp i\,\phi_2(t)$, several physical restrictions lead to the definition of the instantaneous frequency as the average of the derivatives of the two phases, but only in the case that $a_1 = a_2$. Oliveira and Barroso [38] introduce a heterodyne definition of frequency to obtain the average of the two frequencies agreeing with the definition of instantaneous frequency in the case $a_1 \neq a_2$, and also give conditions for the case of n components.

In practice when two frequency time-dependent components are present, we would like to determine both components, and not only the average. In Hamiltonian systems, the coupling between the different dynamical variables produces that several frequency components are present in each degree of freedom of the

trajectory, and we want to obtain the exact value of at least one of them. For us, the case of multicomponent signals can be addressed with a useful definition of instantaneous frequency, rather than a rigorous one.

Consider the signal $f(t) = (2 - .0005(t-45)^2)\exp(2\pi\, i\,(.5t + .6\sin(t/4)))$. This is a monochromatic function with variable phase and amplitude. We see that the variation of the amplitude is not as important as the oscillations due to the complex exponential; therefore, the definition of the instantaneous frequency as the derivative of the phase coincides with our intuition of what the frequency should be. This turns out to be correct since the function f, as a function of complex time t, is entire and therefore it satisfies the definition of analytic signal (Definition 1). In Figure 2.2 a) we plotted the real part of f, and the density plot of the modulus of its wavelet transform is represented in b); note that the maximum of this surface for each time value b corresponds to the instantaneous frequency at that given time, as it can be seen in c).

Consider now the function with two frequency components represented in Figure 2.3. The function to analyze is $f(t) = (1 - .0001(t-45)^2)\exp(2\pi\, i\,(.5t + .6\sin(t/4))) + .6\exp(2\pi\, i\,(1.2t + .6\cos(t/4)))$. Note in the density plot of the modulus of the wavelet transform (Figure 2.3 b) that there are two ridges corresponding to two frequency components; the one with highest intensity corresponds to the component with higher amplitude (around frequency .5), and the band with less intensity corresponds to the component with lower amplitude (around frequency 1.2). This is, the modulus of the wavelet transform has two local maxima for each point in time. In this case, we consider as "the dominant frequency" the one with higher amplitude, corresponding to the absolute maximum. Hence, we define the instantaneous frequency as the one producing the absolute maximum of the modulus of the wavelet transform for each time.

This procedure seems to be appropriate for the computation of the instantaneous frequency of numerical solutions of Hamiltonian systems. When dealing with solutions of a general Hamiltonian system (2.3) we want to assign an instantaneous frequency to a complex time-series of the form $z_k(t) = x_k(t) + i\, y_k(t)$ $(k = 1, \ldots, n)$.

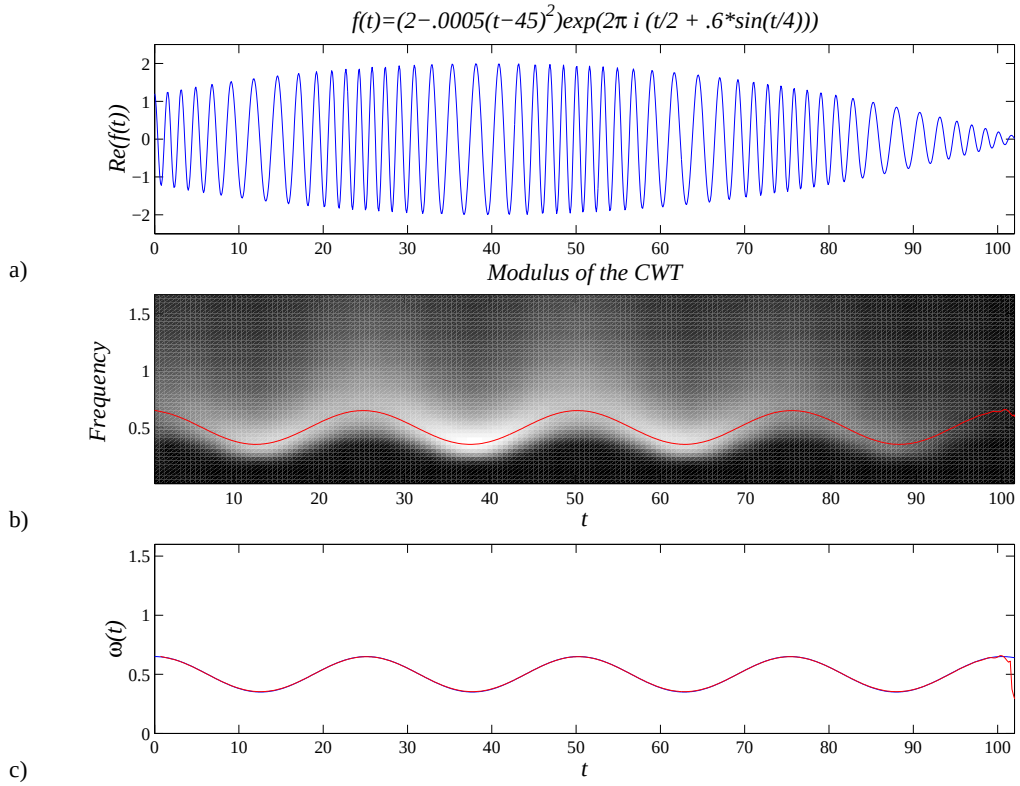

Figure 2.2: a) Analytic signal with variable phase and amplitude, and b) modulus of its wavelet transform. In c), we can see that the maximum of the modulus of the wavelet transform coincides with the instantaneous frequency of the function defined as the derivative of the instantaneous phase.

Due to the coupling terms, these time-series generally have several frequency components. Our aim is to identify n basic frequencies that describe quasiperiodic motions, and to determine how the frequencies vary in time for the case of chaotic trajectories. Therefore, in our heuristic solution for the multicomponent case, we consider only the absolute maximum of the modulus of the wavelet transform of z_k to obtain just one time-varying frequency, and disregard other local maxima. Although it seems that we lose information by doing this, usually the location of other local maxima corresponds to the absolute maximum of another variable of the trajectory, z_l. Therefore, we will end up with as many time-varying frequencies

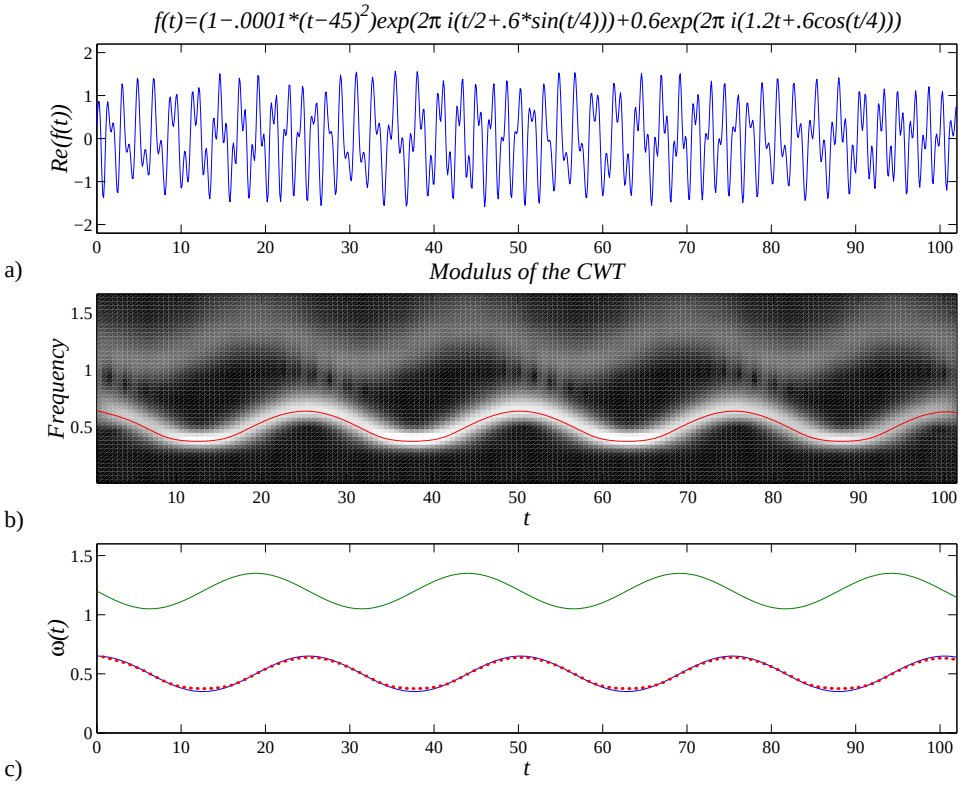

Figure 2.3: a) Two frequency components with variable phase and amplitude, and b) modulus of its wavelet transform. In c), we show how the instantaneous frequency is determined by the absolute maximum (in frequency) for each point in time.

as degrees-of-freedom of the system.

2.7 Other methods

There are other methods available in the literature to analyze dynamical systems; particularly to distinguish chaotic from regular trajectories in nearly integrable Hamiltonian systems. We can mention the method of Lyapunov exponents [29], frequency analysis [25], and the method of twist angles [11]. We refer the reader to [17] for an application of these methods to the standard map and a discussion of the results.

The main advantage of our time-frequency analysis over other methods is that, besides the determination of quasiperiodic and chaotic trajectories, it provides detailed information regarding the order of the resonances in case of quasiperiodic trajectories; furthermore, the treatment of chaotic trajectories is done in a suitable way and we are able to detect resonance trappings and resonance transitions of chaotic trajectories. This information yields good picture of transport in the phase space. Also the applicability of time-frequency analysis is not restricted to near-integrable systems, but it can be used to analyze strongly non-integrable Hamiltonian systems.

Here, as a point of comparison, we outline the method of frequency analysis by Laskar, that can be seen as a special case of the Gabor transform. We refer the reader to [27, 25] for a detailed description and the numerical implementation of the method of Laskar; also see [26] for the analysis of the algorithm and its convergence.

2.7.1 Gabor transform

To include the time variation in the computation of frequency a second parameter is introduced in the Fourier transform, that will localize the spectral information around a given point in time. This results into the *Gabor transform* [12, 9], in which the analyzing function is the usual complex exponential of the Fourier transform, multiplied by a Gaussian function that acts like a time-window:

$$Ff(q,p) = \int_{-\infty}^{\infty} f(t)\, e^{-2\pi i q t}\, e^{-(t-p)^2/2\sigma^2}\, dt$$

The parameter q is the frequency variable, and the parameter p slides continuously the Gaussian window that localizes the signal (other windows can be used as well). In Figure 2.4 a), we represented the analyzing function for two different frequencies. Note that the shape and size of the window is the same for any value of the frequency. Since the size of the time window has to be predetermined, this may produce poor localization and rapid transitions can be missed.

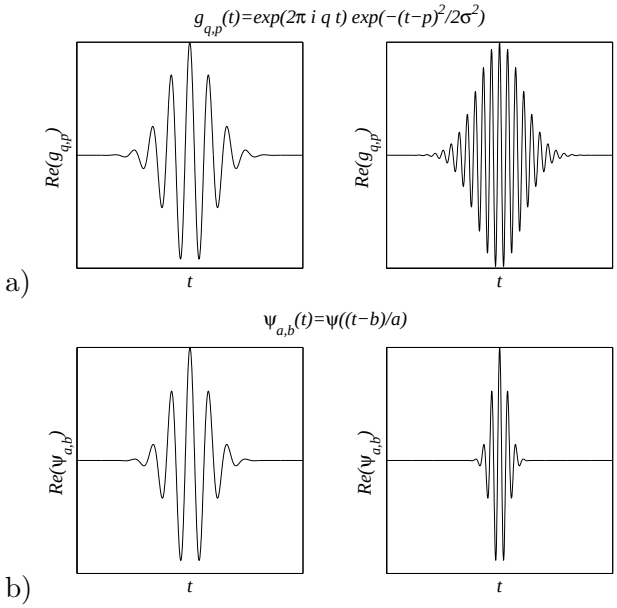

Figure 2.4: Analyzing functions in a) the Gabor transform, and b) the wavelet transform. The plots correspond to low frequency and high frequency.

On the other hand and for comparison, in Figure 2.4 b) we represented the analyzing function in the wavelet transform for different frequencies. Note that the time window automatically contracts for higher frequencies and expands for low frequencies, according to the zoom-in and zoom-out capabilities of the wavelet transform described before. This is the main advantage of the wavelet transform over the Gabor transform, since this capability of adapting the time window to the frequency range produces better localization in time of the spectrum information of the signal.

Laskar's frequency analysis

The method of frequency analysis by Laskar [27, 25] uses Fourier analysis to obtain approximations of quasiperiodic solutions by finite series of complex exponentials of the form $\sum_{j=0}^{N} c_j e^{2\pi i \omega_j t}, \quad c_j \in \mathbb{C}$.

For a nearly integrable system of n degrees of freedom in the action-angle-like coordinates (I, θ), $I = (I_1, \ldots, I_n)$ and $\theta = (\theta_1, \ldots, \theta_n)$, Laskar's frequency analysis

consists of the numerical computation of the fundamental frequency ω_k associated to each degree of freedom $z_k = \sqrt{2I_k}e^{i\theta_k}$ of a given trajectory $(z_1, z_2, \ldots, z_n)(t)$, and of the approximation of the solution by an iterative scheme, giving

$$z_k(t) \approx c_1 e^{2\pi i \omega_k t} + \sum_{j=2}^{N} c_k^j e^{2\pi i \omega_k^j t}.$$

If the given solution is quasiperiodic, a good approximation can be achieved and the value of the frequency vector $\omega = (\omega_1, \ldots, \omega_n)$ is close to the actual rotation vector of the trajectory. Thus, with this method we can determine and analyze quasiperiodic motions in the phase space. For instance one can identify resonant regions when we have a set of initial conditions for which their frequency vector ω satisfies a resonance equation $\mathrm{k} \cdot \omega = 0$ for some integer vector k.

On the other hand, if the trajectory is chaotic the approximation with a quasiperiodic series is compromised due to the evolution in time of the fundamental frequencies. The main idea of Laskar's approach when dealing with chaotic trajectories is to compute the fundamental frequencies in disjoint time intervals of the form $[\tau, \tau + T]$ for different values of τ, and observe how they evolve. This approach has been used extensively in the literature: Chaotic regions are thus detected when the frequencies associated to a set of initial conditions vary greatly with respect to time and with respect to initial conditions. However, the selection of τ and T is a very sensitive part of the procedure, because we have to assume that the trajectory is regular enough in each interval $[\tau, \tau + T]$ to obtain reliable information from the complex exponential expansions.

Chapter 3

Time-Frequency Analysis of Classical Trajectories of the Water Molecule

Abstract

We present a new method of frequency analysis for Hamiltonian Systems of three degrees of freedom and more. The method is based on the concept of instantaneous frequency extracted numerically from the continuous wavelet transform of the trajectories. Knowing the time-evolution of the frequencies of a given trajectory, we can define a frequency map, resonances, and diffusion in frequency space as an indication of chaos. The time-frequency analysis method is applied to the Baggott Hamiltonian to characterize the global dynamics and the structure of the phase space in terms of resonance channels. This three-degree-of-freedom system results from the classical version of the quantum Hamiltonian for the water molecule given by Baggott [5]. Since another first integral of the motion exists, the so called Polyad number, the system can be reduced to two degrees of freedom. The dynamics is therefore simplified and we give a complete characterization of the phase space, and at the same time we could validate the results of the time-frequency analysis.

3.1 Introduction

The Baggott Hamiltonian is a quantum model of the water molecule which was originally developed by Baggott [5] using spectroscopic methods. It is a three-mode vibrational Hamiltonian featuring 1:1 Darling-Dennison resonance between the stretch modes and 2:1 Fermi resonance between the bend and stretches, where the symmetric x, K constraints have been relaxed to obtain better fitting to the experimental data. It has been used extensively in the literature in classical, semiclassical and quantum contexts. The same kind of model has been used for the description of triatomic symmetric molecules such as D_2O, NO_2, ClO_2, O_3 and H_2S [32]. In these models there exists a constant of the motion known as the *Polyad number*, which will translate into an independent first integral in the classical regime.

The classical version of the Baggott Hamiltonian is obtained using the Heisenberg correspondence principle. It is a three degrees of freedom (dof) Hamiltonian given in action-angle variables, and as the quantum version, contains 1:1 and 2:1 resonance couplings. The existence of the Polyad number allows the reduction of the system to 2-dof, and the global dynamics can be studied more easily.

In this work, we were interested in the case of Polyad number P=34.5, which corresponds to the quantum Polyad 16. This value is used in [22] to study the quantum-classical correspondence of highly exited states of the molecule.

In [22], a description of the classical phase space was given in terms of resonant two-dimensional tori and resonance channels calculated with the Chirikov resonance analysis. This procedure uses the integrable limits of the Hamiltonian obtained when only one resonance coupling is considered. The location of the resonance channels was the basis for the classification of the eigenstates of the Baggott Hamiltonian.

With the method of time-frequency analysis presented in this work, we are able to locate exactly the resonance channels and to show their angular dependence. Therefore, the Chirikov analysis gives only an approximation and the treatment

of the Baggott Hamiltonian as a near integrable one is not so obvious.

We can also identify chaotic trajectories that are trapped temporarily around a resonant channel, suggesting the concept of time-varying resonances. This notion can explain how the energy of the system is distributed and how it is transported along the resonances during the evolution in time.

With the information of the resonances channels and the diffusion of the trajectories, we give a complete characterization of the dynamics in the phase space.

The organization of this chapter is as follows: In Section 3.2 we present the Baggott Hamiltonian, and describe the reduction of the system to 2-dof. The time-frequency analysis based on wavelets was used to analyze the classical trajectories of this system; this is presented in Section 3.3 together with the description of how the resonance structures determine the dynamics of the system. We also identify the chaotic zones in the phase space by numerically computing the diffusion of the system. The conclusion is found in Section 3.4. In the Appendix A.5, we describe the transformations to obtain the 2-dof Baggott Hamiltonian.

3.2 Baggott Hamiltonian

The classical version of the quantum Hamiltonian for the water molecule by Baggott [5] is given by

$$H = H_0 + H^{1:1} + H^{2:2} + H_1^{2:1} + H_2^{2:1}, \tag{3.1}$$

$$\begin{aligned}
H_0 =& \Omega_s(I_1 + I_2) + \Omega_b I_3 + \alpha_s(I_1^2 + I_2^2) + \alpha_b I_3^2 + \varepsilon_{ss} I_1 I_2 + \varepsilon_{sb} I_3(I_1 + I_2),\\
H^{1:1} =& (\beta_{12} + \lambda'(I_1 + I_2) + \lambda'' I_3)(I_1 I_2)^{1/2} \cos(\theta_1 - \theta_2),\\
H^{2:2} =& \beta_{22} I_1 I_2 \cos 2(\theta_1 - \theta_2),\\
H_1^{2:1} =& \beta_{sb}(I_1 I_3^2)^{1/2} \cos(\theta_1 - 2\theta_3),\\
H_2^{2:1} =& \beta_{sb}(I_2 I_3^2)^{1/2} \cos(\theta_2 - 2\theta_3),
\end{aligned}$$

where $(I_1, I_2, I_3, \theta_1, \theta_2, \theta_3)$ are action-angle coordinates.

The Baggott Hamiltonian is a three-degree-of-freedom (dof) system exhibiting 2:1 resonance between the bend and stretch modes, and 1:1 and 2:2 resonances between the two stretch modes. There is a permutation symmetry between the indices 1 and 2, and also note that the Hamiltonian is not differentiable at $I_1 = 0$ or $I_2 = 0$. The values of the parameters are obtained to fit the experimental spectra. We used here the notation in [22]. See Table 3.1.

Ω_s	3885.57 (cm^{-1})
Ω_b	1651.72
α_s	-81.99
α_b	-18.91
ε_{ss}	-12.17
ε_{sb}	-19.12
β_{12}	-112.96
λ'	6.04
λ''	-0.16
β_{22}	-1.82
β_{sb}	18.79

Table 3.1: Parameters of the Baggott Hamiltonian.

The system possesses a first integral which is the classical expression of the quantum Polyad number of the system. It is given by

$$P = 2(I_1 + I_2) + I_3. \tag{3.2}$$

This constant of motion P is related to the quantum Polyad $\mathtt{P}$ by $P = 2\mathtt{P} + 5/2$ [22]. Equation (3.2) implies that the values of the actions are bounded: $0 < I_1 < P/2$, $0 < I_2 < P/2$ and $0 \leq I_3 < P$.

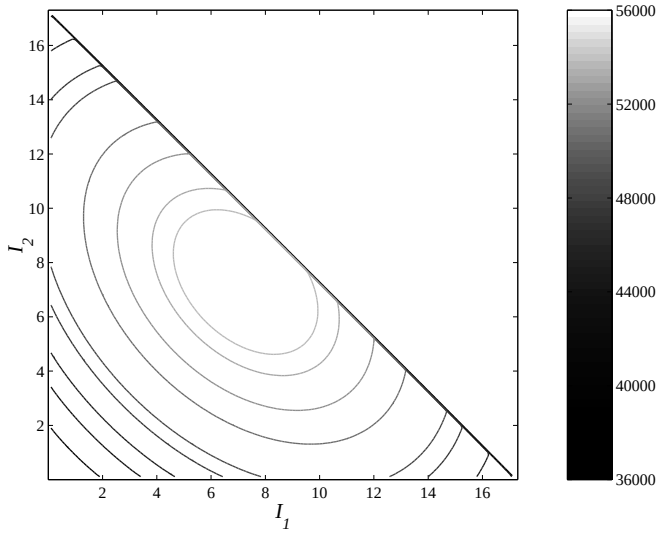

Figure 3.1: Energy levels for a slice of the phase space corresponding to $\theta_1 = \theta_2 = \theta_3 = 0$, projected onto the action plane (I_1, I_2), with $I_3 = P - 2(I_1 + I_2)$, and $P = 34.5$.

In this work, we study the Polyad number $P = 34.5$, that corresponds to the quantum Polyad number $\mathtt{P} = 16$. This is the same value used in [22] to study highly excited states of the molecule. We will use time-frequency analysis based on wavelets to give a more accurate and complete characterization of the phase space for this Polyad number.

Taking the angles $\theta_1 = \theta_2 = \theta_3 = 0$, the intersection of the energy surfaces $H = H_0$ with the plane $P = 34.5$ can be drawn as contours projected to the plane I_1, I_2, since I_3 is obtained from Equation (3.2). These contours are represented in Figure 3.1.

Equation (3.2) will allow us to reduce the Baggott Hamiltonian to a 2-dof system. Via successive canonical transformations we obtain first the Hamiltonian in normal coordinates, and then a system in action-angle variables $(N_1, N_2, N_3, \psi_1, \psi_2, \psi_3)$ for which the third action satisfies

$$N_3 = P,$$

and the conjugate angle ψ_3 does not appear explicitly in the Hamiltonian, as we should expect. The details of these transformations can be found in the Appendix A.5.

Therefore, for a fixed value of P, the system can be considered as a 2-dof system in the variables $(N_1, N_2, \psi_1, \psi_2)$, and afterwards we can solve for the third angle ψ_3.

The 2-dof Hamiltonian is given by

$$\begin{aligned} H =& \alpha_1 N_1 + \alpha_2 N_2 + \alpha_3 + \beta_3 N_1^2 + \beta_4 N_1 N_2 + \beta_5 N_2^2 \\ &+ \beta_1 \sqrt{N_1 + N_2}(-2N_2 + P)\cos\psi_2 \\ &- \beta_2 (N_1^2 + N_1 N_2)\cos 2\psi_1. \end{aligned} \tag{3.3}$$

For the Polyad number $P = 34.5$, the values of the parameters are given in Table 3.2.

α_1	$-112.96 - .16\,P \quad = -118.48$
α_2	$525.65 + 56.44\,P \quad = 2472.83$
α_3	$1651.72\,P - 18.91\,P^2 \quad = 34476.71$
β_1	26.5731
β_2	−76.8150
β_3	73.1750
β_4	79.5350
β_5	−78.7125

Table 3.2: Parameters of the 2-dof Hamiltonian (in cm^{-1}) for $P = 34.5$.

Since the Baggott Hamiltonian can be reduced to a 2-dof system, it is possible to construct Poincaré maps to obtain a global view of the dynamics for P fixed and a particular value of the energy $H = H_0$.

In action-angle coordinates $(N_1, N_2, \psi_1, \psi_2)$, the Poincaré section we defined is

$$\Sigma = \{(N_2, \psi_2) : H(N_1, N_2, \psi_1, \psi_2) = H_0, \psi_1 = 0, \dot{\psi}_1 > 0\}.$$

The plots of the Poincaré maps for $P = 34.5$ and different values of the energy H_0 are shown in Figure 3.2. We can observe alternation between chaotic and regular motions, and the chaotic motion predominates for higher values of the energy.

3.3 Wavelet time-frequency analysis of the Baggott Hamiltonian

For completely integrable Hamiltonian systems in action-angle variables $H(I, \theta) = H_0(I)$ the frequency map is defined by

$$I \to \omega(I) = \frac{\partial H_0}{\partial I}.$$

This map characterizes trajectories for nearly integrable systems as well, since the non-resonant tori are preserved under small perturbations, according to the KAM theorem.

The computation of time-varying frequencies enables the assignment of frequencies even for non-nearly-integrable cases. The time-frequency analysis we present relies on a frequency map computed numerically with the wavelet approach described in Chapter 2, particularly in Sections 2.3 and 2.5.

We perform time-frequency analysis of the Baggott Hamiltonian for the case $P = 34.5$.

To define the frequency map, we proceed as follows: constrain the initial con-

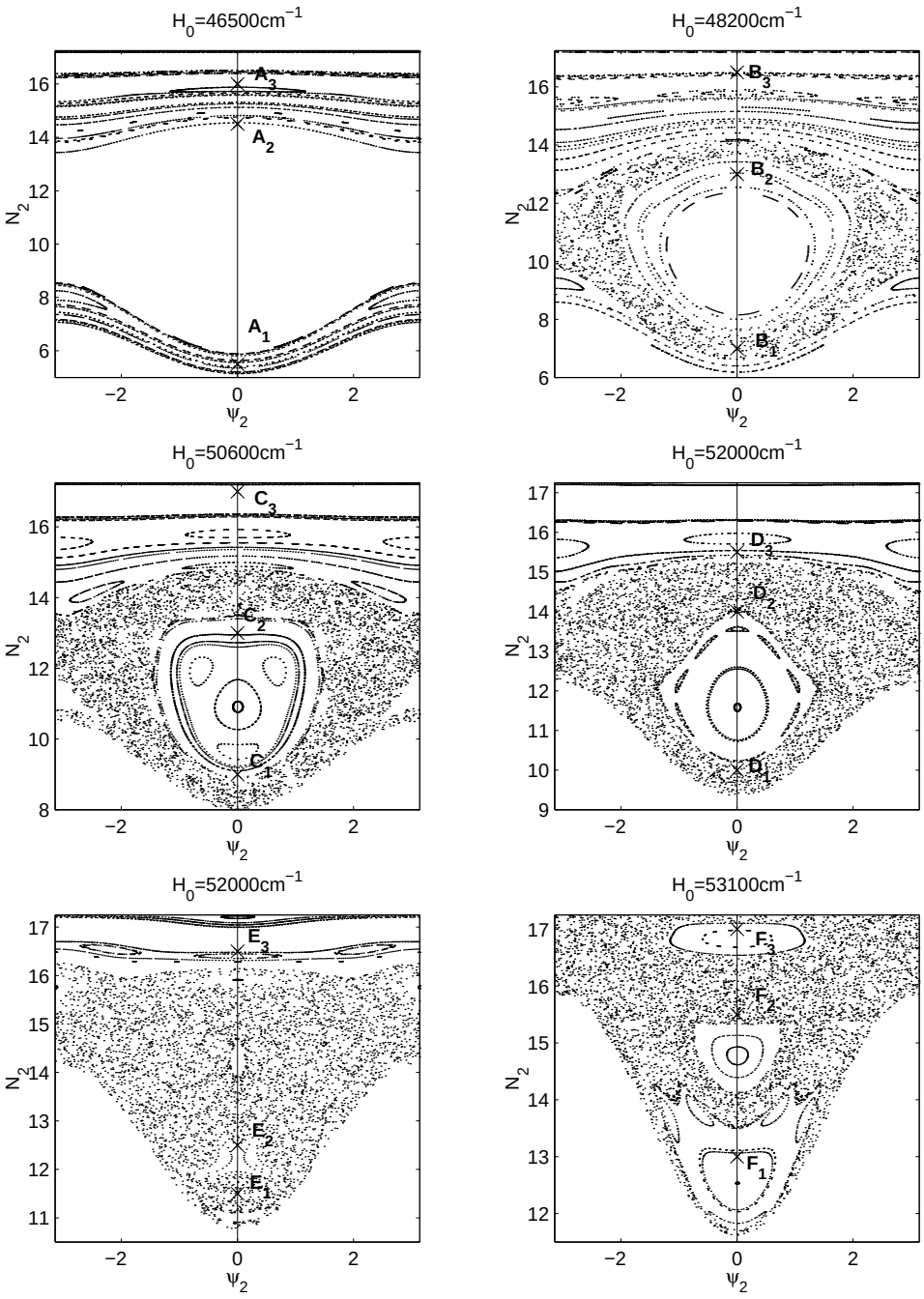

Figure 3.2: Poincaré sections for $P = 34.5$, $\psi_1 = 0$, $\dot{\psi}_1 > 0$.

ditions to a particular slice of the phase space given by

$$\begin{aligned} &0 < I_1 < P/2, \quad 0 < I_2 < P/2, \quad I_1 + I_2 \leq P/2, \\ &I_3 = P - 2(I_1 + I_2), \\ &\theta_1 = \theta_2 = \theta_3 = 0, \end{aligned} \tag{3.4}$$

(see Figure 3.1).

For a given initial condition (I_1^0, I_2^0) in this slice, we obtain numerically the trajectories over the time interval $[0, T]$ and express them in complex coordinates $z_k(t) = \sqrt{2I_k(t)}\, e^{i\theta_k(t)},\ k = 1, 2, 3$, for $t \in [0, T]$. We then obtain the evolution in time of the associated fundamental frequencies $\omega_k(t)$ for $t \in [0, T]$, by computing the maximum of the modulus of the wavelet transform (see Section 2.5). The frequency map is then defined as

$$(I_1^0, I_2^0, I_3^0) \longrightarrow (\omega_1, \omega_2, \omega_3)(t),\ t \in [0, T].$$

The procedure for the computation of the frequency map can be summarized as follows:

1. Grid of initial conditions.

   The initial conditions in the slice (3.4) are evenly spaced in the coordinates (I_1, I_2) in the form:

   $$\begin{aligned} I_1^0 &= 0.1 * k, \quad k = 1, \ldots, 172 \\ I_2^0 &= 0.1 * m + .01, \quad m = 1, \ldots, 172 - k. \end{aligned}$$

2. Numerical integration of the trajectories.

   For each initial condition, the trajectory is numerically integrated over a time interval $[0, T]$, $T = 5.7$. We use a Runge-Kutta method of order 7-8, with automatic step size control (approx. 100,000 iterations). The trajectory is

expressed in complex coordinates:

$$z_j = \sqrt{2I_j}e^{i\theta_j}, \quad j = 1, 2, 3.$$

The step size is small to ensure small error of the integration method. For the computation of the frequency, the complex time series z_1, z_2, z_3 are sampled leaving their lengths of approximately 10000 points not equally spaced in time. This sampling does not have an effect on the accuracy of the method, and reduces the computational time due to less multiplications in the evaluation of the wavelet transform.

3. Computation of the frequencies.

   For each time series z_1, z_2 and z_3, we compute a series corresponding to the evolution in time of the fundamental frequencies ω_1, ω_2, ω_3. The frequency is obtained from the scale producing the maximum modulus of the wavelet transform at each time point. This was done with the routines in Appendix A.4.

Some examples of time-frequency analysis for the Baggott Hamiltonian are shown in Figure 3.3.

The reduction to 2-dof of the Baggott Hamiltonian allows us to compare the frequency map analysis with the Poincaré map for each trajectory. In this way we can decide whether a given trajectory is quasiperiodic or chaotic, and see that there is an exact correspondence with time-frequency analysis: quasiperiodic trajectories have frequencies that remain constant in time, whereas chaotic trajectories have frequencies with large variation in time.

Time-frequency analysis based on wavelets has the obvious advantage over Poincaré maps of being applicable to any number of degrees of freedom; besides it provides a quantitative as well as a qualitative method to characterize quasiperiodic, resonant and chaotic motions. The advantage over the Laskar approach of frequency analysis, described in Section 2, is the improved resolution of the evolution in time of the frequencies associated with the trajectory. Due to the "zoom-in"

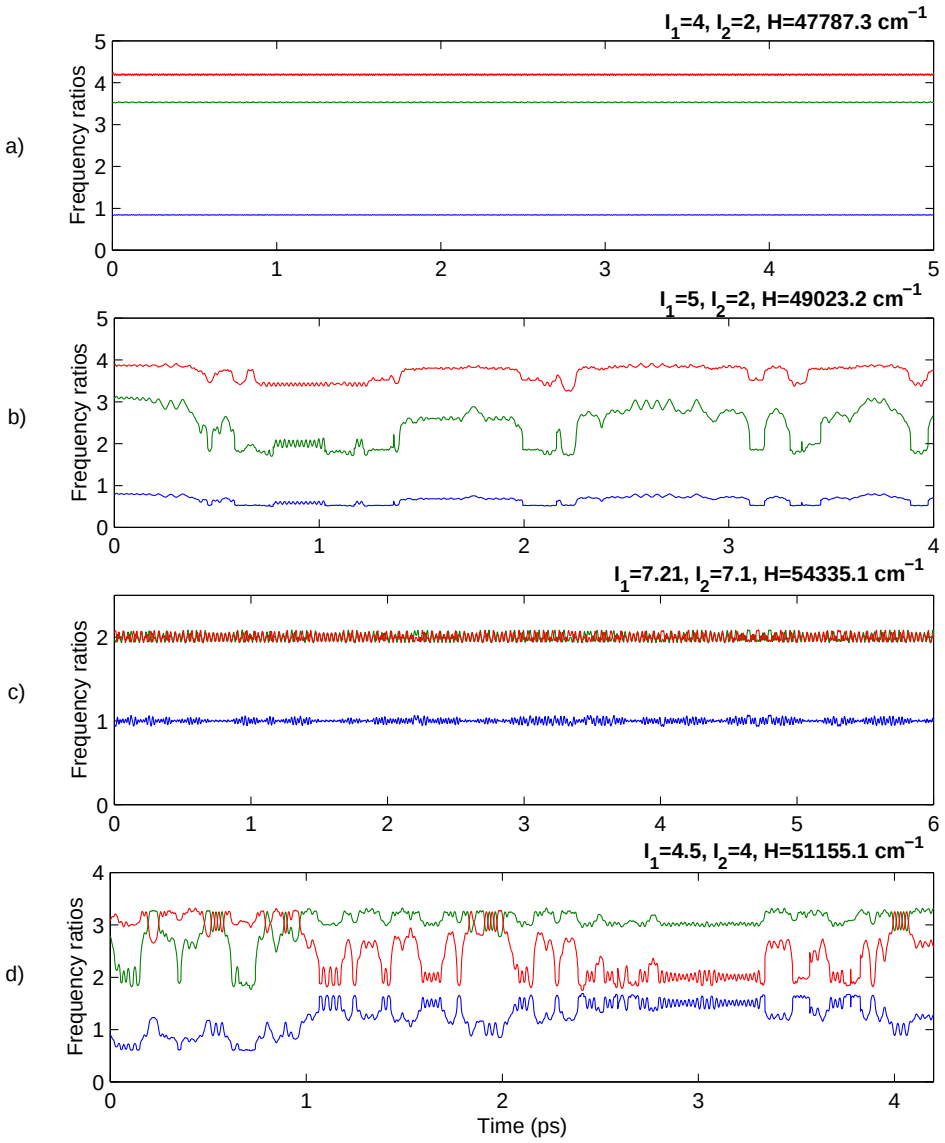

Figure 3.3: Time-frequency analysis for some trajectories of the Baggott Hamiltonian, ω_1/ω_2 is blue, ω_1/ω_3 is green, and ω_2/ω_3 is red. a) corresponds to a quasiperiodic trajectory, meanwhile b), c) and d) correspond to chaotic trajectories.

and "zoom-out" capabilities of wavelets (see Section 2.3), we do not have to assume slow transition of the frequencies or to propose *a priori* the size of the interval in which the trajectory behaves close to quasiperiodic, which is a sensitive part of the Laskar approach.

With time-frequency analysis, quasiperiodic trajectories can be identified due to the small deviation of $\omega_k(t)$ from its mean value $\widetilde{\omega}_k$. This mean value is actually the value that we would obtain with the method of Laskar; thus we can recover the results obtained with that approach. We can define a "mean frequency vector" $(\widetilde{\omega}_1, \widetilde{\omega}_2, \widetilde{\omega}_3)$ that corresponds to the fundamental frequency in the case of quasiperiodic solutions.

With this in mind we can compute the Arnol'd web, which is the mapping of the actions to the frequency ratios:

$$(I_1^0, I_2^0) \longrightarrow \left(\frac{\widetilde{\omega}_1}{\widetilde{\omega}_3}, \frac{\widetilde{\omega}_2}{\widetilde{\omega}_3} \right).$$

For a grid of evenly spaced initial conditions (I_1^0, I_2^0) in the slice (3.4), we performed time-frequency analysis and plotted the Arnol'd web in Figure 3.4.

We can observe the lines corresponding to resonance equations:

$$k_1\widetilde{\omega}_1 + k_2\widetilde{\omega}_2 + k_3\widetilde{\omega}_3 = 0,$$

for some integers k_1, k_2, k_3. Therefore, the main resonances found are the ones we expected for the form of the Hamiltonian: 1:1 resonance between I_1 and I_2 (stretches), and 2:1 resonance between I_1 and I_3, and between I_2 and I_3 (stretch-bend). We found also higher order resonances, all of them intersecting at the same point. See Figure 3.4.

Note in Figure 3.4 that the resonance line $\widetilde{\omega}_1 = \widetilde{\omega}_2$ (the 45^o line) is rather isolated, yielding to the conjecture that this resonance exists, but it does not have a large effect on the quasiperiodic motion nearby. On the contrary, the 2:1 resonance lines (the vertical line $\widetilde{\omega}_1/\widetilde{\omega}_3 = 2$ and the horizontal line $\widetilde{\omega}_2/\widetilde{\omega}_3 = 2$) are surrounded by many dots, indicating that the 2:1 resonance has a strong effect on

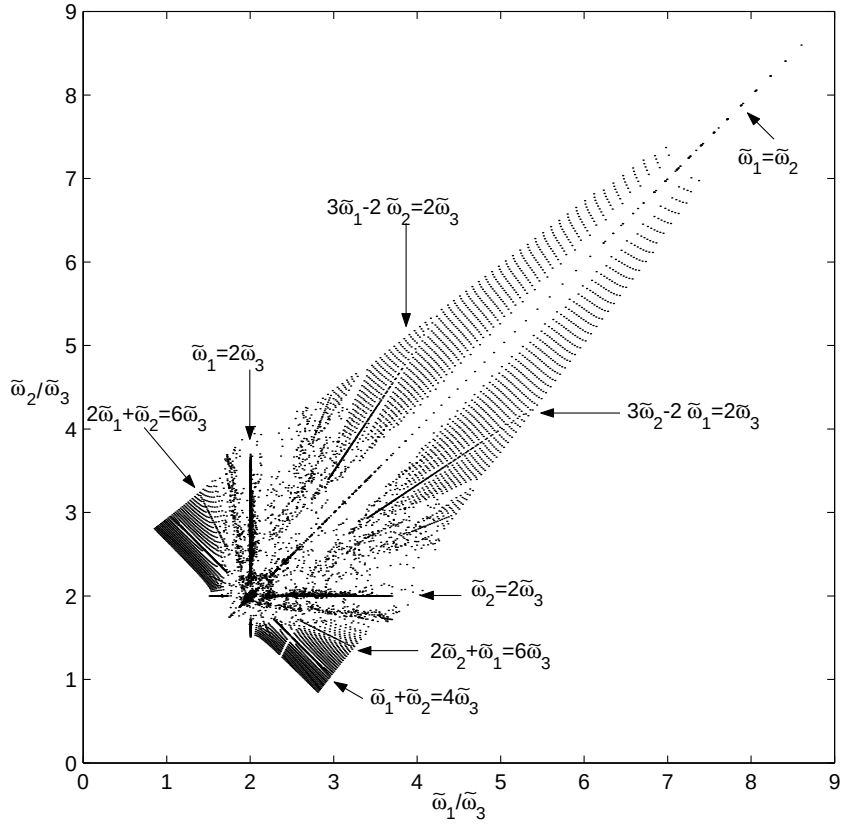

Figure 3.4: Arnol'd web of the Baggott Hamiltonian for $P = 34.5$.

the motion for this particular slice of the phase space.

3.3.1 Resonance channels

With time-frequency analysis we can locate the resonant trajectories, i.e., initial conditions for which their mean frequencies satisfy a given resonance equation up to certain accuracy. Inverting the frequency map, we can find the resonant regions in the phase space; the results for the Baggott Hamiltonian are presented in Figure 3.5. We can see that the predominant resonances are in three areas, one corresponding to 1:1 resonance on the symmetry line $I_1 = I_2$, and two regions corresponding to the 2:1 resonances. There are also higher order resonances, as indicated in the Figure 3.4.

We also plotted in Figure 3.5 some invariant two-dimensional stable tori with initial conditions in the slice. The tori were found as stable fixed points of the Poincaré maps of the 2-dof system (3.3): these points correspond to stable periodic orbits for the four-dimensional system, and these periodic orbits correspond to stable 2-tori of the six-dimensional Baggott Hamiltonian (3.1). We can see in Figure 3.5 that the resonant tori are at the center of the so called resonance channels, i.e., initial conditions strongly affected by the existence of the resonance.

In [22], Keshavamurthy and Ezra consider the H_0 part of (3.1) as the unperturbed Hamiltonian, and the remaining terms as *small* perturbations. Then, they define the frequencies as in the near-integrable case, i.e., as the partial derivatives of H_0 with respect to the actions. These frequencies were used to determine the classical resonances. They also obtained the resonance channels using the Chirikov analysis, a procedure that uses the integrable limits of the Hamiltonian, i.e., when some terms are neglected.

Figure 1 in [22] has some similarities with our Figure 3.5, regarding the location of the main resonances, the resonant tori, and the resonance channels. However, the results of the time-frequency analysis we present correspond to the full Hamiltonian (3.1), and not only to the integrable approximations used in [22].

We can observe in Figure 3.4 that all the resonances intersect at the same point. This can be seen also in Figure 3.5, since around the point $(I_1, I_2) = (7.2703, 7.2703)$ the resonance channels overlap. We will show in Section 4.2 that there is a periodic orbit passing through this point, that corresponds to the intersection of the two main resonances, 1:1 and 2:1.

3.3.2 Diffusion

The concept of diffusion of a trajectory is used generally to describe a drift in the action variables and characterize unstable motion in the phase space. This concept can be translated to a variation in frequencies using the method of time-frequency analysis.

We explained before that the chaotic motion is characterized by the variation in

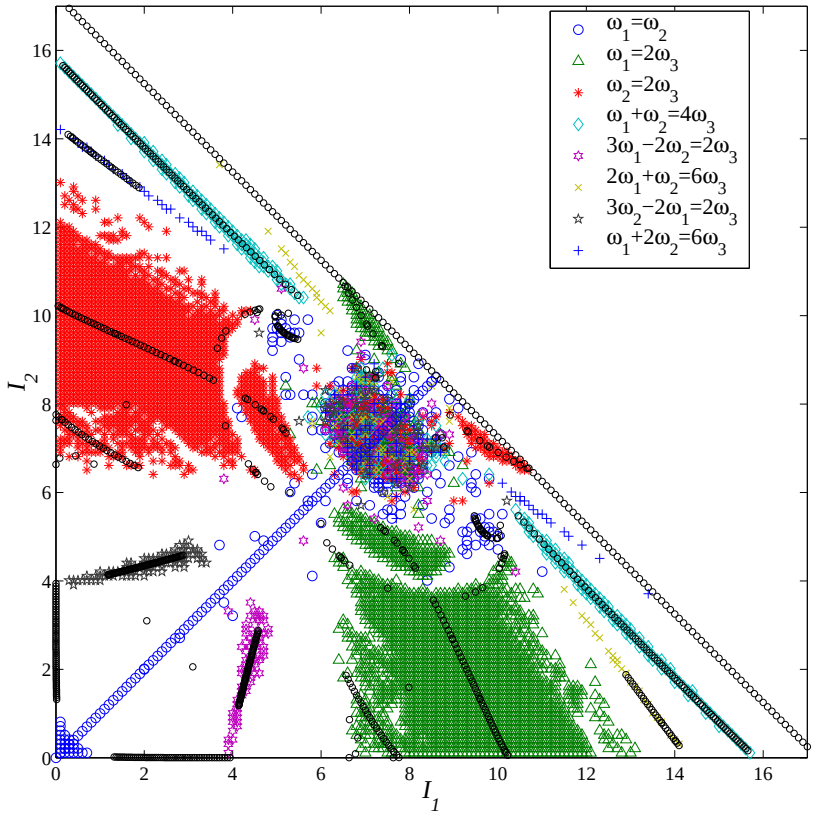

Figure 3.5: Resonance channels. Stable two-tori are indicated in black circles.

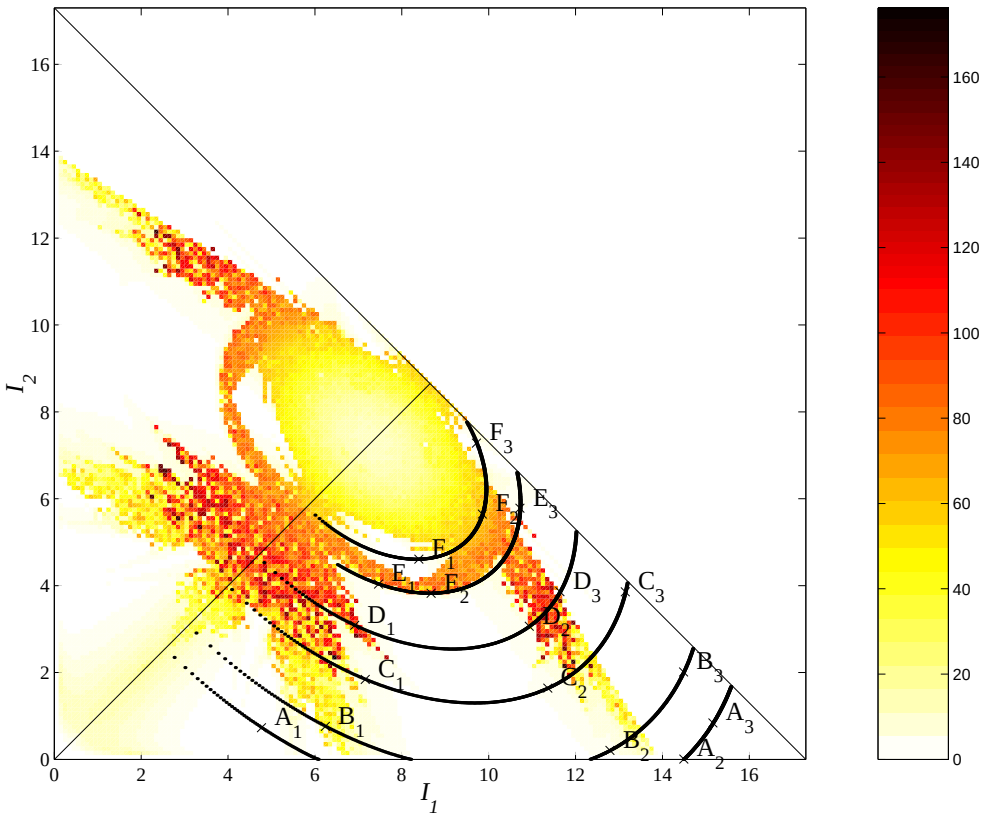

Figure 3.6: Diffusion plot of the Baggott Hamiltonian. The points marked on the energy contours correspond to the points in the Poincaré sections of Figure 3.2.

time of the frequencies with respect to their mean value. The size of this variation is closely related to the drift of the trajectory in action space, this is something that we can check again by looking at the Poincaré map. If the trajectory is strongly chaotic, i.e., if it fills up a big area of the Poincaré section in a short time, there is a large deviation of the frequencies from their mean value. This motivated our definition of diffusion of a trajectory in terms of the frequencies:

Definition 4 *For a trajectory with initial conditions* (I^0, θ^0)*, time-frequency analysis provides the evolution in time of its fundamental frequencies:* $\omega_1, \omega_2, \omega_3$ *in* $[0, T]$*. Then we define the diffusion of the trajectory over the interval* $[0, T]$ *by*

$$\text{diffusion}(I^0, \theta^0) = dev_1 + dev_2 + dev_3,$$

where

$$dev_k = \frac{1}{T} \int_0^T |\omega_k(t) - \widetilde{\omega}_k| dt.$$

Laskar [25] used an approximation of the second derivative of the frequency map with respect to initial conditions as an indicator of the chaotic behavior of the trajectory. He also showed some examples for which this approximation is proportional to the derivative of the frequency map with respect to time, calculated as the difference of the frequency in two successive intervals of time. Arguing that this relation is characteristic of diffusion, he used these approximations interchangeably as a measure of the diffusion of the trajectory in frequency space.

Our definition of diffusion also makes use of this correspondence between chaotic trajectories and variation of the frequencies. However, we include all the spectral information of the trajectory in the interval $[0, T]$, given by the frequency map. Meanwhile, Laskar used only the "mean frequencies" in two successive intervals. It is clear that the better resolution we achieve with frequency analysis based on wavelets yields a more dynamic indicator of the diffusion.

We compute the diffusion of the Baggott Hamiltonian in the slice (3.4) with the frequency map described above. Therefore, to each initial condition in the slice,

we associate the diffusion and plot a density graph corresponding to this slice of the phase space. The results of these computations are shown in Figure 3.6. This figure renders the symmetry of the system with respect to I_1 and I_2 (recall that the initial conditions were taken symmetric, $\theta_1 = \theta_2$). The quasiperiodic areas (low diffusion) and chaotic areas (high diffusion) are well distinguished. We can observe that for low values of the energy (see also Figure 3.1), most initial conditions have low diffusion; however, as the energy increases, we observe alternation between low and high diffusion, showing the coexistence of regular motion and strongly chaotic motion. When the energy is close to the maximum (around the point $(I_1, I_2) = (7.2703, 7.2703)$), large diffusion predominates but it is not as large as in some other regions, indicating that all trajectories are chaotic but they do not have much room to wander.

Figure 3.6 confirms the results in Figure 3.5: The resonance channels have zero or very low diffusion, that is, the values of the frequencies remain fairly constant in time and therefore the motion is quasiperiodic in those areas. The symmetry line $I_1 = I_2$, corresponding to the 1:1 resonance, is surrounded by quasiperiodic motion for low values of the energy (up to $46500\,\mathrm{cm}^{-1}$). For higher values of the energy, the symmetry line is surrounded by trajectories with large diffusion (strongly chaotic); therefore, the 1:1 resonance channel is very thin in this slice. Basically it includes only the line $I_1 = I_2$. On the contrary, the 2:1 resonance channels correspond to a large region with low diffusion, then the resonant 2-tori are surrounded by quasiperiodic trajectories strongly affected by the resonance.

All the results in the diffusion plot correspond exactly to the analysis of the Poincaré maps (Figure 3.2). We have picked some points in Figure 3.2 on the line $\psi_2 = 0$, and the same points have been plotted in the original coordinates in Figure 3.6 with their corresponding energy contours. This allows us to compare the dynamics in both figures, as we do in the following. Note we only plotted points with $I_1 < I_2$; the symmetric points with $I_1 > I_2$ correspond to a different Poincaré section and the analysis is analogous.

For low values of the energy H_0, all the trajectories are quasiperiodic (see

points A_1, A_2, A_3). When H_0 increases, chaotic motion appears (see the point B_1) alternating with regular motion.

In the Poincaré sections we can observe quasiperiodic trajectories for large values of N_2 (points B_3, C_3, D_3), some of them in resonant islands (points A_3, E_3). For all these trajectories, the value of I_3 is small, or equivalently $I_1 + I_2 \approx P/2$; physically this corresponds to initial conditions with the bend mode close to equilibrium.

The 2:1 resonance channel corresponds to the large regular area at the center of the Poincaré sections, appearing for the first time around $48800\,\mathrm{cm}^{-1}$. This regular area remains up to values of the energy around $53100\,\mathrm{cm}^{-1}$, for instance between the points C_1 and C_2 and between the points D_1 and D_2; the closed curves we see in the Poincaré sections between these points correspond to quasiperiodic trajectories lying on invariant 3-tori of the 3-dof system; these trajectories form the resonance channel, since they have frequencies close to the 2:1 resonance.

Note in both Figure 3.5 and 3.6 that the boundary of the 2:1 resonance channel has some "fingers" or gaps. These are consequence of the alternation between small regular islands and chaotic regions that we can observe in the Poincaré sections. The islands correspond to higher order resonances that we did not plot.

At the point E_2 in Figure 3.6 the 2:1 resonance channel breaks. This can be seen also in the Poincaré section for $H_0 = 53100\,\mathrm{cm}^{-1}$: Instead of the regular region, there is a saddle point surrounded by chaotic trajectories. The corresponding 2-torus is unstable.

For $H_0 = 53600\,\mathrm{cm}^{-1}$ we find several resonances, the point F_1 is in the 2:1 resonance between I_1 and I_3, and the point F_3 is in the 2:1 resonance between I_2 and I_3. There is also a small quasiperiodic region with 1:1 resonance. All these resonances alternate with chaotic trajectories.

The quasiperiodic regions disappear completely around $53900\,\mathrm{cm}^{-1}$, and from here to the maximum ($54340\,\mathrm{cm}^{-1}$) all trajectories have large diffusion, corresponding to Poincaré sections filled with chaotic trajectories.

Comparing the resonance plot and the diffusion plot (Figures 3.5 and 3.6), we

observe some quasiperiodic areas which are not close to resonance (for instance the region around points B_3 and C_3). These areas may act as boundaries for the diffusion of trajectories. To explain this with an example, in Figure 3.7 we plot different representations of one chaotic trajectory: a) the Poincaré map, b) its frequency evolution in time, and c) the frequency ratios (dark line) on top of the Arnol'd web (dots). Note there is an accumulation of points around a resonant island of the Poincaré section, corresponding in b) to the beginning where the trajectory is close to the 2:1 resonance. After certain time the trajectory leaves this resonance, but we can observe that it wanders around the resonances 2:1 and 1:1. This is more clear in c), the trajectory passes by the three main resonance lines; however, it remains around the point $(\widetilde{\omega}_1/\widetilde{\omega}_3,\ \widetilde{\omega}_2/\widetilde{\omega}_3) = (2, 2)$, and never goes to the regions corresponding to quasiperiodic trajectories.

This particular trajectory is not the exception; it can be observed in many chaotic trajectories that their frequencies wander around the main resonances when they evolve in time. This suggests the concept of time-varying resonances, i.e., trajectories for which their frequencies are trapped temporarily around a resonance, but they leave for another resonance and so forth. Energy transport between the different modes of the motion can occur in this way via chaotic trajectories.

3.3.3 Two more slices of the phase space

All the analysis that we have done so far was for the particular slice of the phase space given in (3.4). We have shown how frequency analysis allows a complete description of the phase space for initial conditions in that particular slice.

To obtain a more complete analysis of the phase space, we consider two different slices, and perform time-frequency analysis on them with the same procedure as before. Figures 3.8 and 3.9 show the resonance channels and the diffusion plot for initial conditions evenly spaced in action space, and angles given by

$$\theta_1^0 = \pi,\ \ \theta_2^0 = 0,\ \ \theta_3^0 = 0,$$

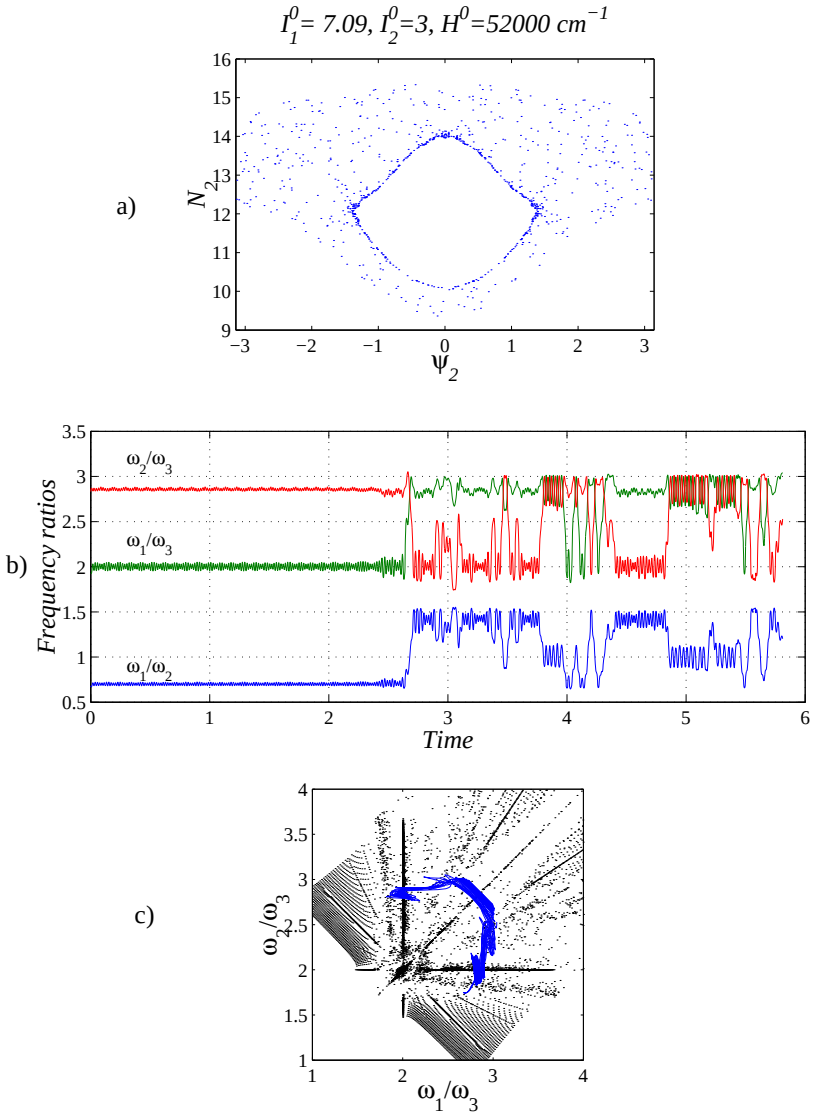

Figure 3.7: One chaotic trajectory showing first low diffusion around the 2:1 resonance, and then wandering around the main resonance channels. See text for explanation.

and

$$\theta_1^0 = \pi, \;\; \theta_2^0 = \pi, \;\; \theta_3^0 = 0,$$

respectively.

Observe that Figure 3.8 is no longer symmetric as a result of nonsymmetric initial conditions. In this slice we can observe that the 1:1 resonance between the stretches (I_1 and I_2) is predominant, and the 2:1 resonance between I_1 and I_3 is not present. This shows how the Chirikov resonance analysis performed in [22] disregards the angular dependence of the resonance channels. The structure of the phase space can hardly be understood with the integrable approximations of the Hamiltonian. The Baggott Hamiltonian cannot be treated as nearly integrable without losing important features of the dynamics.

In Figure 3.9 the initial conditions are symmetric; however, we can observe new higher order resonances occupying large regions of the slice, showing a different structure from that of (3.4).

3.3.4 Some more phase space structure

It is still interesting to look at the symmetry line $I_1 = I_2$. This line corresponds to $N_1 = 0$ in the reduced coordinates (3.3) and is invariant under the 2-dof flow. In the full six-dimensional phase space, this invariant surface is two-dimensional when the energy is fixed.

We can study the flow on this surface by looking at the intersection of the set $N_1 = 0$ with a constant energy surface $H = H_0$. The intersection can be expressed as the invariant curve

$$Q_1 = \{(0, N_2, 0, \psi_2) : \alpha_3 + \alpha_2 N_2 + \beta_5 N_2^2 + \beta_1 \sqrt{N_2}(-2N_2 + P)\cos\psi_2 = H_0\}$$

(where to avoid the indefinition of the angle ψ_1 for $N_1 = 0$, we have fixed it arbitrarily as 0). The curves for several values of H_0 can be observed in Figure 3.10.

Note that the fixed points of the 2-dof system in Q_1 correspond to periodic

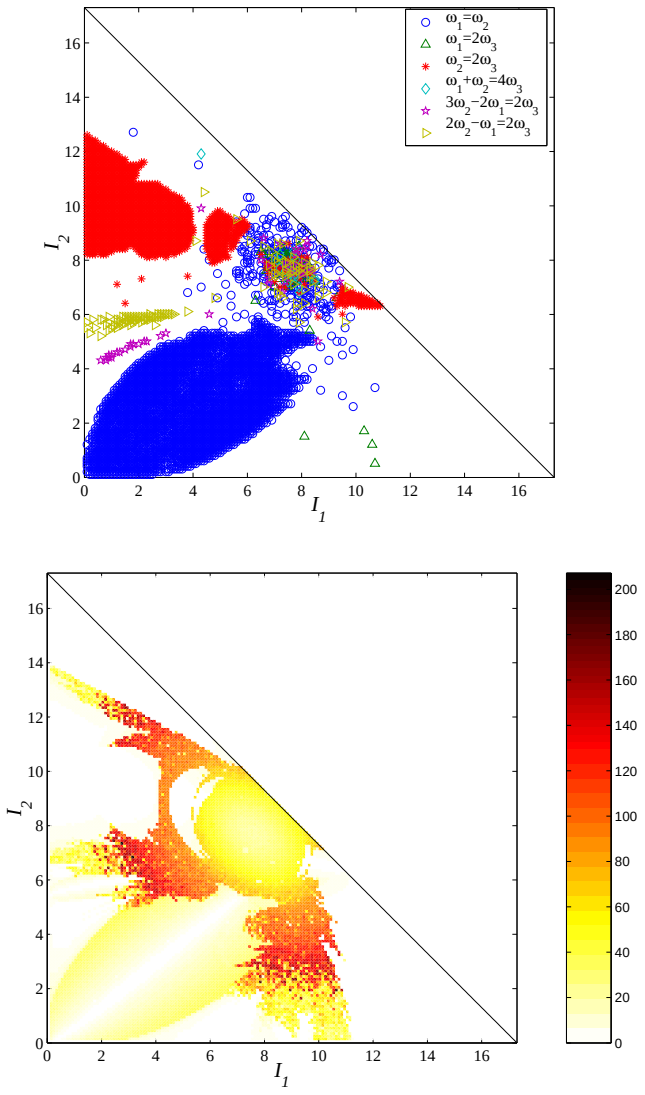

Figure 3.8: Resonance channels and diffusion plot for the slice $\theta_1 = \pi$, $\theta_2 = \theta_3 = 0$, $I_3 = P - 2(I_1 + I_2)$, $P = 34.5$.

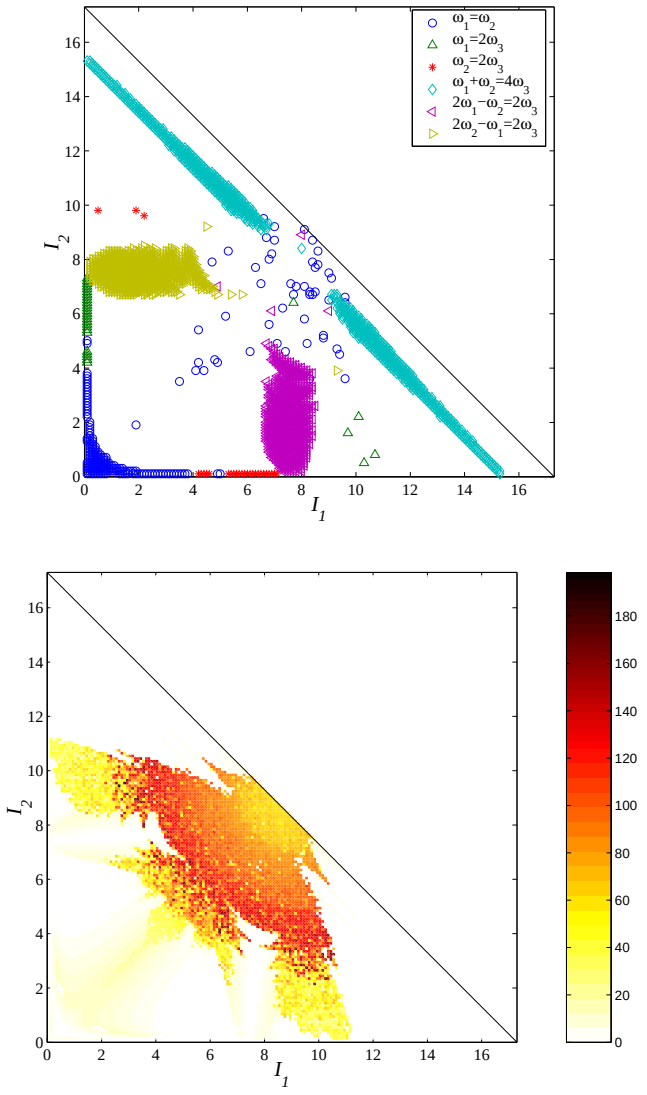

Figure 3.9: Resonance channels and diffusion plot for the slice $\theta_1 = \theta_2 = \pi$, $\theta_3 = 0$, $I_3 = P - 2(I_1 + I_2)$, $P = 34.5$.

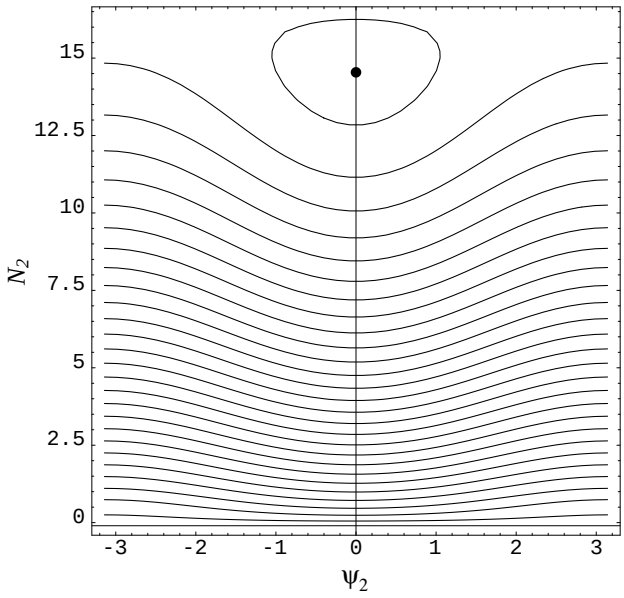

Figure 3.10: Invariant curve $Q_1 = \{N_1 = 0\}$. Each curve corresponds to a particular value of the energy H_0.

orbits when the third angle ψ_3 is considered; therefore, they are periodic orbits of the full 3-dof system (3.1). The fixed point at $\psi_2 = 0$, $N_2 = 14.5406$ is a center-saddle point for the 2-dof system; therefore, the corresponding periodic orbit of the 3-dof system has a three-dimensional center manifold, a two-dimensional unstable manifold and a two-dimensional stable manifold. Its coordinates in the original variables are expressed as $I_1 = I_2 = N_2/2 = 7.2703$, $I_3 = P - 2N_2$, $\theta_1 = \theta_2 = 2\psi_3$, $\theta_3 = \psi_3$.

Furthermore, this periodic orbit can be found directly in the original coordinates (3.1) if we solve for the intersection of the resonance channels 1:1 and 2:1; that is, solving the equation $\dot{\theta}_1 = 2\dot{\theta}_3$ for I_1 considering $I_1 = I_2$ and $\theta_1 = \theta_2 = 2\theta_3$. We have to note that this periodic orbit is located at the global maximum of the energy H restricted to the slice (3.4).

Since most of the curves Q_1 are closed (ψ_2 is an angle in $[0, 2\pi]$), they correspond to two-dimensional tori in the six-dimensional system. Observing that the line $\psi_2 = 0$ in Figure 3.10 corresponds exactly to the line $I_1 = I_2$ with $I_1 = N_2/2$,

then we can conclude that this line is foliated with invariant 2-tori (with the exception of the periodic orbit we just mentioned above).

Another invariant surface of the 2-dof flow (3.3) is given by $N_2 = P/2$, since for this value $\dot{N}_2 = 0$. This surface corresponds to the invariant set $I_3 = 0$ in the original coordinates (3.1). In other words, the bend mode is in equilibrium. This is the case of a system with only the 1:1 stretch coupling that can be reduced to 1-dof, therefore completely integrable. In [54], this problem is studied and a complete characterization of the phase space in terms of P is given.

The intersection of the surface $N_2 = P/2$ with a constant energy manifold can be written as

$$Q_2 = \{(N_1, \frac{P}{2}, \psi_1, \psi_2) : \alpha_3 + \alpha_2\frac{P}{2} + \beta_5\frac{P^2}{4} + (\alpha_1 + \frac{\beta_4}{2}P)N_1 +$$

$$\beta_3 N_1^2 - \beta_2 N_1(N_1 + P/2)\cos 2\psi_1 = H_0\}.$$

The intersection of this surface for a given value of H_0 with a plane $\psi_2 = constant$ is represented by a curve in the Figure 3.11.

The expression of Q_2 we obtained here corresponds exactly to the normal mode representation of the Hamiltonian in [54]. In that work, they propose a reparametrization of the trajectories such that the phase space is a sphere with constant Polyad number. We refer the reader to that work for a detailed explanation of the bifurcations in the phase space.

We will see that Q_2 is a two-dimensional manifold in the phase space. Since $I_3 = 0$, the conjugate angle θ_3 must be fixed arbitrarily to avoid indefinition, say $\theta_3 = 0$. After the coordinate transformations, this implies $\psi_3 = 0$. For H_0 fixed, Q_2 is two-dimensional manifold when ψ_2 is considered. More precisely the closed curves in Figure 3.11 are two tori for the 2-dof system. Since the third angle $\psi_3 = 0$, they are also 2-tori in the full six-dimensional phase space.

The fixed points in Q_2 are actually periodic orbits of the 2-dof system ($\psi_2 \in [0, 2\pi]$). Again, since $\psi_3 = 0$, they are periodic orbits for the full six-dimensional

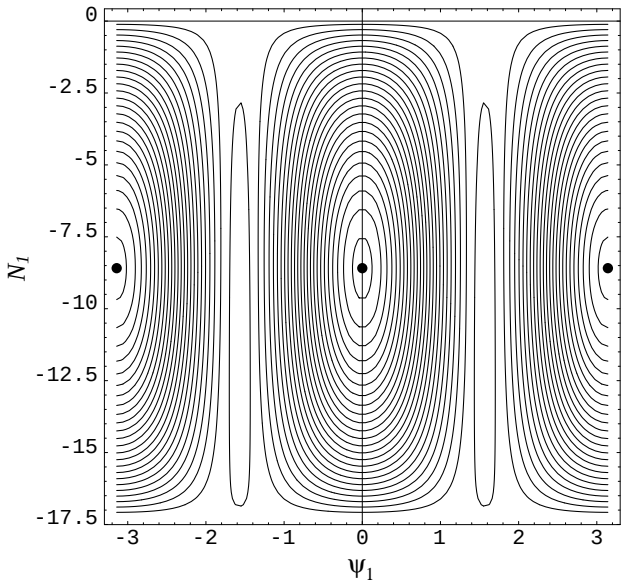

Figure 3.11: Intersection of the invariant surfaces $Q_2 = \{N_2 = P/2\}$ with a plane $\psi_2 = constant$, for different values of H_0.

system. The fixed points at $N_1 = -8.59$, $\psi_1 = 0, \pi$ are elliptic, then the corresponding periodic orbits are stable and they can be expressed in the original coordinates as $I_1 = 17.2499$, $I_2 = .00004$, $I_3 = 0$, $\theta_1 = \theta_2 = \psi_2$, $\theta_3 = 0$, and the symmetric point $I_1 = .00004$, $I_2 = 17.2499$.

In the intersection of Q_1 and Q_2 there is another periodic orbit, with coordinates $N_1 = 0$, $N_2 = P/2$, $\psi_1 = 0$ and $\psi_2 \in [0, 2\pi]$. The coordinates of this orbit in the six-dimensional phase space are $I_1 = I_2 = P/4$, $I_3 = 0$, $\theta_1 = \theta_2 = \psi_2$, $\theta_3 = 0$. This periodic orbit is unstable.

Some fixed points of (3.3) not lying in the invariant surfaces can be found solving numerically the equations $\dot{\psi}_1 = 0$, $\dot{\psi}_2 = 0$ with $\psi_1 = 0, \pi$ and $\psi_2 = 0$. These points correspond to periodic orbits for the six-dimensional phase space, since the third angle ψ_3 is a parameter in $[0, 2\pi]$. Their coordinates in the original variables are $I_1 = 10.27$, $I_2 = 0.0009$, $I_3 = 13.9504$, $\theta_1 = \theta_2 = 2\psi_3$, $\theta_3 = \psi_3$; and its corresponding symmetric point, $I_1 = 0.0009$, $I_2 = 10.27$; the orbits are stable.

3.4 Conclusion

The method of frequency analysis based on wavelets that we have presented is a good alternative to study a wide range of dynamical systems. Since wavelet analysis allows simultaneous localization in frequency and time, we can compute time-varying frequencies associated to trajectories, and in this way characterize the motion of systems with oscillatory trajectories.

Time-frequency analysis based on wavelets proved to be very suitable for the Baggott Hamiltonian due to the vibrational character of the solutions. For this system, the fundamental frequencies are obtained with great accuracy in the case of quasiperiodic solutions.

And due to the capability of adjusting the time window automatically for every frequency, with the wavelet approach we compute more reliable information about the variation in time of the frequencies of chaotic trajectories. This is the main advantage with respect to the frequency analysis of Laskar, where a fixed interval of time is used, disregarding the possibility of rapid transition in the frequencies.

Also, the definition of diffusion we present seems more adequate than the one given by Laskar. Since we are capable to compute the variation with respect to time of the frequencies, we obtain an indicator of the diffusion at every time.

With frequency analysis based on wavelets, we were able to characterize the phase space of the Baggott Hamiltonian for the Polyad number $P = 34.5$. We have located the resonance channels, the quasiperiodic motion and the regions with large diffusion, producing an exact picture of the global dynamics of the system. We also showed the angular dependence of the resonance channels, concluding that the system cannot be treated as a nearly integrable one.

Chapter 4

Transport and Resonance Transitions in the Restricted Three Body Problem

Abstract

Our method of time-frequency analysis based on wavelets is applied to the problem of transport between different regions of the Solar system, based on the model of the planar circular restricted three body problem. The method is based on the extraction of instantaneous frequencies from the wavelet transform of the numerical solutions. Time-varying frequencies provide a good diagnostic tool to discern chaotic trajectories from regular ones, and we can identify resonance islands that greatly affect the dynamics. Good accuracy in the calculation of time-varying frequencies allows us to determine resonance trappings of chaotic trajectories, and resonance transitions. We show the relation between resonance transitions and transport between different regions of the phase space.

4.1 Introduction

In Hamiltonian systems that feature chaotic dynamics, transport in the phase space is greatly affected by the existence of resonance islands: chaotic trajectories can be trapped around a resonance for a long time, or can wander around different islands.

The goal of this work. We propose the use of a wavelet-based method of time-frequency analysis to study the dynamics of Hamiltonian systems for which the trajectories display oscillatory behavior. This method was introduced in [49] to study the global dynamics of a molecular system; however, it can be applied in a large variety of systems. This chapter presents the application of this method to the well known planar circular restricted three body problem.

Wavelet-based time-frequency analysis. Time-frequency analysis is a numerical tool that allows us to distinguish between regular and chaotic trajectories by computing time-varying frequencies associated with the trajectories. Since quasiperiodic trajectories are characterized by constant frequencies, the variation in time of the frequency is a good indicator of chaos.

The method allows us to detect resonance islands that greatly affect the dynamics of the system in the sense that they "capture" temporarily chaotic trajectories nearby. We can show that chaotic trajectories that remain around a resonance island for some time have frequencies that satisfy the resonance equation during that interval of time. This process is what we call a *resonance trapping*. Since the method we propose yields good accuracy in the frequency evolution, we know exactly when a chaotic trajectory has been trapped, or has undergone a transition between resonances. We show how the resonance transitions are related to transport in the phase space.

The PCRTBP. The planar circular restricted three body problem (PCRTBP) has been a subject of extensive study in the disciplines of astrodynamics, celestial mechanics and dynamical systems. This is the problem that inspired H. Poincaré in the development of what we know now as the qualitative theory of dynamical systems.

The PCRTBP is a Hamiltonian system of two degrees of freedom, for the motion of a small body attracted by the gravitational forces of two other bodies orbiting in circles. The model can be applied to systems like the Sun-Jupiter-

comet, or the Earth-Moon-satellite, and the assumptions allow this model to be the starting point in the design of space missions. The PCRTBP has been as well a benchmark for testing dynamical systems techniques.

Application of time-frequency analysis. The main motivation to apply this technique to the PCRTBP arises in the context of the results of Koon *et al.* [23] that related the transport mechanism with resonance transitions. In particular, we found that the time-varying frequencies associated with the orbits in the inertial frame provide enough information to detect transitions between different regions of the phase space. In this work, time-frequency analysis is applied to the restricted three body problem to study the transport mechanism between the interior and exterior regions of the Solar System. This is why time-frequency analysis is so important for this problem.

Koon *et al.* [23] show the existence of heteroclinic connections between periodic orbits around the libration points L_1 and L_2 (the Lyapunov orbits) with the same energy. The heteroclinic connections are obtained as a result of the intersections of the invariant manifolds associated to the Lyapunov orbits, and these intersections occur in the regions corresponding to the 2:3 and 3:2 resonances. Since the invariant manifolds of the Lyapunov orbits are two-dimensional objects that form tubes in a three-dimensional energy surface in phase space, these tubes provide dynamical channels between different regions of the phase space. Therefore, by following the structure of these tubes, Koon *et al.* [23] were able to describe an important ingredient in transport in phase space.

With time-frequency analysis we are able to add the time component to the picture given by the invariant manifolds: by keeping track of the resonance transitions, we know where the system is at a given point in time; in other words, we know what trajectories are trapped in the different resonances during some period of evolution. Using this approach, we are able to detect key regions in the phase space in which rapid resonance transitions occur.

Since we know exactly when resonance transitions take place, we are able to

describe the occurrence of resonance transitions between the outer resonances and the inner resonances. This will provide an indication of transport between the exterior and interior regions of the Solar system in terms of time.

An additional advantage over the invariant manifold approach to study transport is the dimensionality of the problem. The computation of invariant manifolds can be extremely difficult, especially for higher dimensional systems and for long-time evolution. Time-frequency analysis provides a good and computationally efficient approach to study transport. Although the calculations in this work are done for the planar restricted three body problem, which is two degrees of freedom, by design time-frequency analysis based on wavelets is generalizable to systems of three degrees of freedom or more. The analysis of the spatial three body problem is promising work in progress.

The organization of this chapter is as follows. In Section 4.2 we describe the equations of motion and general aspects of the dynamics of the PCRTBP. The application of time-frequency analysis based on wavelets is described in 4.3, and the results are presented in Section 4.4. Finally, the conclusions are in Section rtb:conclusions.

4.2 Description of the PCRTBP

The planar circular restricted three body problem (PCRTBP) is a system in which a small body moves in a plane under the attraction of two primary bodies moving in circular orbits. For instance, the primaries can be the Sun and Jupiter, and the problem will consist of the description of the motion of a comet. The motion of the two primaries is restricted to a particular solution of the Kepler problem: the two bodies move in circular orbits around their center of mass. The third body is assumed to be a "point mass," i.e., it is small enough so that the motion of the primaries is not influenced by its presence.

When the time and position coordinates are normalized [45], the system has only one parameter μ, which is the ratio between the mass of one primary and the

total mass of the system. For instance, for the Sun-Jupiter system with masses m_S and m_J, the mass parameter is

$$\mu = \frac{m_J}{m_J + m_S} = 0.0009537.$$

The equations of motion of the third body are given in the coordinates (x, y) of a system of axes rotating at the same angular velocity as the primaries. In this frame, the primaries are fixed at the points $(-\mu, 0)$ and $(1-\mu, 0)$. The equations of motion can then be expressed as

$$\begin{aligned}
\dot{x} =& v_x, \\
\dot{v}_x =& 2v_y + x - \frac{(1-\mu)(x+\mu)}{r_1^3} - \frac{\mu(x-1+\mu)}{r_2^3}, \\
\dot{y} =& v_y, \\
\dot{v}_y =& -2v_x + y - \frac{(1-\mu)y}{r_1^3} - \frac{\mu y}{r_2^3},
\end{aligned} \tag{4.1}$$

where $r_1 = \sqrt{(x+\mu)^2 + y^2}$ and $r_2 = \sqrt{(x-1+\mu)^2 + y^2}$.

The equations of motion (4.1) are the Euler-Lagrange equations corresponding to the Lagrangian function given by

$$L = \frac{1}{2}\left((v_x - y)^2 + (v_y + x)^2\right) + \left[\frac{1-\mu}{r_1} + \frac{\mu}{r_2} + \frac{\mu(1-\mu)}{2}\right].$$

The corresponding conserved energy is given by

$$E = \frac{1}{2}(v_x^2 + v_y^2) - \left[\frac{1}{2}(x^2 + y^2) + \frac{1-\mu}{r_1} + \frac{\mu}{r_2} + \frac{\mu(1-\mu)}{2}\right]. \tag{4.2}$$

The energy is related to the Jacobi constant C [45] by $E = -C/2$.

In this work we are interested in the system Sun-Jupiter-Comet, for values of the energy close to that of comet Oterma, $E = -1.515$ (Jacobi constant $C = 3.03$). (For a description of the motion of comet Oterma, see [23]).

System (4.1) can also be expressed in Hamiltonian form via the Legendre trans-

formation from the Lagrangian L, with the momenta defined as

$$p_x = v_x - y, \qquad p_y = x + v_y,$$

and Hamiltonian function given by,

$$H = \frac{1}{2}[(p_x + y)^2 + (p_y - x)^2] - \frac{1}{2}(x^2 + y^2) - \frac{1-\mu}{r_1} - \frac{\mu}{r_2} - \frac{\mu(1-\mu)}{2}.$$

From the equation of conservation of energy (Equation 4.2), one immediately notices that

$$v_x^2 + v_y^2 \; = \; 2E + (x^2 + y^2) + 2\frac{1-\mu}{r_1} + 2\frac{\mu}{r_2} + \mu(1-\mu) \geq 0.$$

This inequality provides the values of the position coordinates x, y for which the motion is allowed; this region is known as the Hill's region. The boundary of the Hill's region is formed by the curves for which $v_x = v_y = 0$ for a specific value of the energy E.

The Hill's region for the Sun-Jupiter system is displayed in Figure 4.1. Note that the forbidden region defines three areas where motion is possible: the interior region around the Sun, the Jupiter region, and the exterior region.

Equilibrium points and their stability. The PCRTBP has five equilibrium points: the so called libration points L_1, L_2 and L_3, and the Lagrangian or equilateral points L_4 and L_5. The values of the energy that we study are slightly higher than the value of the energy at L_2. The corresponding Hill's region for these values divide the phase space in three areas: the interior region around the Sun, the Jupiter region, and the exterior region. See Figure 4.1 for a scheme of the Hill's region and the position of the libration points.

By analyzing the linear dynamics around the fixed points L_1 and L_2, it follows from Lyapunov's center theorem that there is a family of periodic orbits around each fixed point parameterized by the energy. These Lyapunov orbits are unstable;

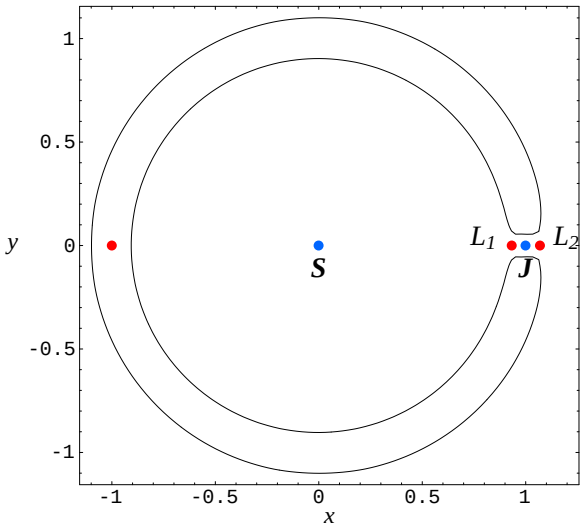

Figure 4.1: Hill's region of the Sun-Jupiter system. Motion is possible in the interior region around the Sun, the Jupiter region, and the exterior region.

therefore, they have two-dimensional stable and unstable invariant manifolds in the corresponding three-dimensional energy surface. The invariant manifolds intersect each other along the periodic orbit. These stable and unstable manifolds form tubes that give a nice template to describe the channels that produce an exchange of the particle between the interior and exterior regions.

Dynamics on the Poincaré section. Recall that for the Sun-Jupiter-Comet system, the mass parameter is $\mu = 0.0009537$, which is the largest μ in the Solar system. Notice that the value $\mu = 0$ corresponds to a system of two bodies: only one primary and the small body. Therefore, the case $\mu = 0$ is equivalent to the Kepler problem with one infinitesimal mass, hence is integrable. Although one might think that the value of μ for the system with the Sun and Jupiter as primaries is small, this system features highly chaotic behavior. This can be clearly seen from the computation of a Poincaré map. As the Poincaré section, we choose the plane $y = 0$ with $v_y > 0$. The Poincaré section obtained is shown in Figure 4.2. In this figure we can observe different resonance islands; in particular, in the

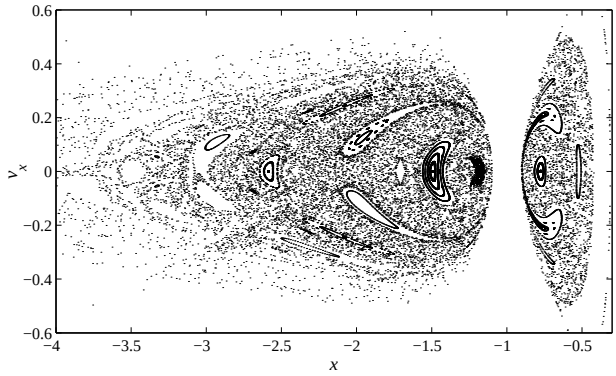

Figure 4.2: Poincaré section corresponding to $y = 0$, $v_y > 0$, and energy $E = -1.515$.

exterior region there is an island in 2:3 resonance with respect to the motion of Jupiter, and in the interior region there is the island in 3:2 resonance with Jupiter.

Figure 4.2 is a common picture of the dynamics of a non-integrable system with two degrees of freedom. Essentially two types of motion are identified: *i*) regular orbits forming "islands" of quasiperiodic motion, created by nonlinear resonances; and *ii*) chaotic areas surrounding them like an "ocean."

4.3 Time-frequency analysis of the PCRTBP

Time-frequency analysis based on wavelets allows us to reproduce the picture of the Poincaré section (Figure 4.2) in terms of the diffusion in frequency space associated to the trajectories. In the this section we will show the capability of time-frequency analysis based on wavelets to discern regular from chaotic motion. With time-frequency analysis we can also identify when the motion of the comet is in resonance with respect to the motion of the primaries. Finally, we are able to determine exactly when a chaotic trajectory "visits" a resonant area, by attaining its frequency very close to resonance for some period of time. We will see that the resonance transitions shed light of the mechanism of transport between the inner and outer regions of the Solar system, and reproduce the template that the

invariant manifolds of the Lyapunov periodic orbits provide.

The frequency of the solutions of the PCRTBP that we shall use is associated with the representation of the orbits in the configuration space in the inertial frame. The objective is to construct numerically a *frequency map*, by associating time-varying frequencies with the trajectories over a fixed time interval $[0, T]$.

4.3.1 Frequency map

We compute the frequency map for the PCRTBP (Equations 4.1) with the following procedure:

- The initial conditions are taken in the rotating frame (x, v_x, y, v_y) with a fixed value of the energy of $E = -1.515$ that corresponds to the energy of the comet Oterma. They are on an evenly spaced grid of points in the plane (x, v_x) corresponding to $y = 0$, $x < -1$, where $v_y > 0$ is chosen to fit the energy level. The initial conditions are located in the exterior region of the Solar system. In Figure 4.3, the initial conditions are represented by large dots, and the Poincaré map is plotted for reference in the background.

- For each initial condition (x^0, v_x^0), we numerically integrate the trajectory $(x, y, v_x, v_y)(t)$, $t \in [0, T]$. In this case, $T = 2000 \approx 318$ Jupiter years. We express the orbit in configuration space in inertial coordinates,

$$Z(t) = (X + iY)(t) = e^{-it}(x + iy)(t).$$

- We extract the instantaneous frequency $\omega(t)$ of $Z(t)$, $t \in [0, T]$, by computing the ridge of the wavelet transform of $Z(t)$.

Definition 5 *The frequency map is expressed as*

$$(x^0, v_x^0) \longmapsto \omega(t), \qquad t \in [0, T].$$

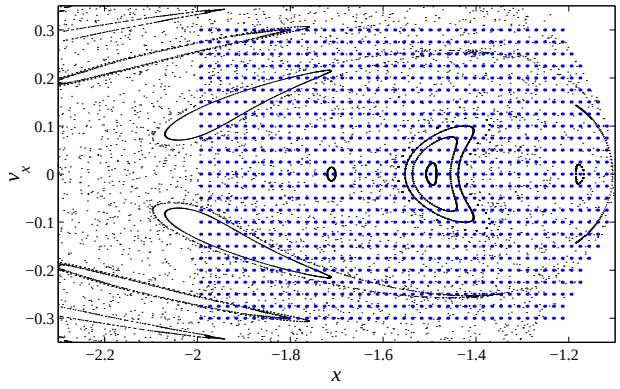

Figure 4.3: Initial conditions for the frequency map: they are in the plane x, v_x with $y = 0$ and $E = -1.515$. The background small dots correspond to the Poincaré map.

4.3.2 Computation of the instantaneous frequency

The general method is described in Chapter 2. The instantaneous frequency (Section 2.4) was obtained from the ridge of the wavelet transform of the orbit Z. We refer the reader to Section 2.5 for a detailed description of the algorithms for the computation of the instantaneous frequency.

In this work, we use the Morlet-Grossman wavelet [9],

$$\psi(t) = \frac{1}{\sigma\sqrt{2\pi}}\, e^{2\pi i\lambda t}\, e^{-t^2/2\sigma^2},$$

where σ and λ are parameters that can be tuned to obtain better resolution. For our case, $\sigma = 1$ and $\omega = .8$ proved to be convenient to detect rapid transitions in the frequency.

4.3.3 Diffusion

The variation in time of the frequency will be a good indicator of whether a trajectory is regular or not. A trajectory with regular motion will have a frequency that is constant in time. If the frequency varies greatly in time, this suggests that the orbit is chaotic.

If for a particular initial condition the frequency is constant in time, then the mean frequency $\widetilde{\omega}$ is equal to this constant value and coincides with the basic Fourier frequency of the orbit. For chaotic orbits, the mean frequency $\widetilde{\omega}$ does not have a physical meaning, but it can be used as reference to compute how much the frequency is varying in time. We consider the average variation of the frequency with respect to $\widetilde{\omega}$ as an indicator of how chaotic the trajectory is. We call this average variation the *diffusion*.

Definition 6 *The diffusion associated to a trajectory with initial conditions* (x^0, v_x^0) *is defined as*

$$\text{Diffusion} = \frac{1}{T}\int_0^T |\omega(t) - \widetilde{\omega}|dt. \tag{4.3}$$

4.4 Results

The results of the computation of the frequency map are represented in Figure 4.4. In a), we present the density plot of the mean frequencies $\widetilde{\omega}$ on the plane of initial conditions (x, v_x). The color code represents the mean frequency divided by the frequency of Jupiter; this is, a mean frequency of 1 represents a trajectory which has the same frequency as Jupiter. In b), the diffusion obtained with the formula in Equation (4.3) is represented in a similar way.

We see a resemblance between the Poincaré map (Figure 4.2) and the density plot of the mean frequency (Figure 4.4). The regions corresponding to chaotic trajectories have a significant mixture of frequencies, and high values of the diffusion. We can also easily identify in Figure 4.4 the regions for which the trajectories have the same frequencies and low diffusion, and see that they correspond to resonance islands. In particular, we can detect the island in 2:3 resonance with respect to the motion of Jupiter, and the islands in 1:2 and 3:5 resonances.

4.4.1 Results for individual trajectories

With time-frequency analysis we can also analyze individual trajectories. In Figure 4.5 we present two trajectories with interesting dynamics: they have large diffusion

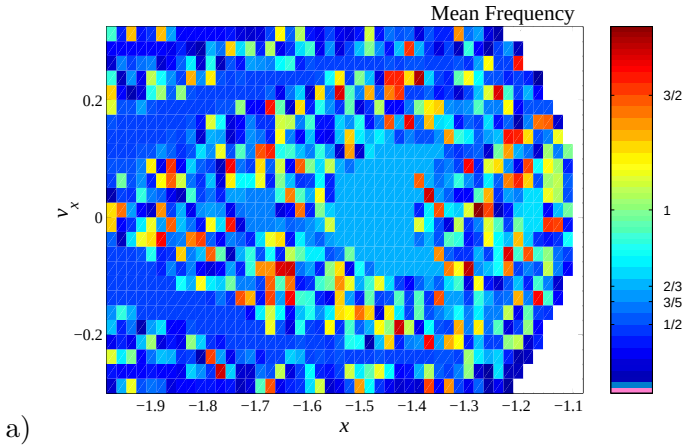

a)

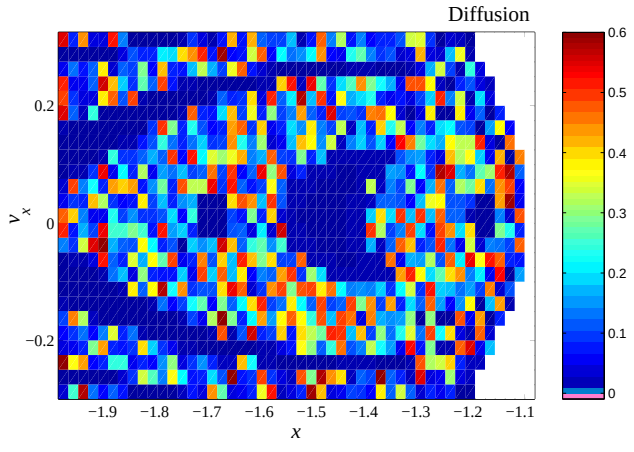

b)

Figure 4.4: Results of time-frequency analysis: a) mean frequency (in ratio with the frequency of Jupiter), and b) the diffusion plot.

but remain close to a resonance for some time. The orbit in inertial coordinates is represented in the first panel, and the time-varying frequency (in ratio with the frequency of Jupiter) is represented in the second panel. The lines labeled as 2:3 and 3:2 were plotted as a reference, and they correspond to the value of frequency that is in such resonance with the motion of Jupiter. Figure 4.5 a) displays a chaotic trajectory with frequency close to the 2:3 resonance; it remains there for a long time before it drifts away. In Figure 4.5 b), we see a trajectory that jumps from nearby the 2:3 resonance to nearby the 3:2 resonance; and jumps again to the 1:2 resonance.

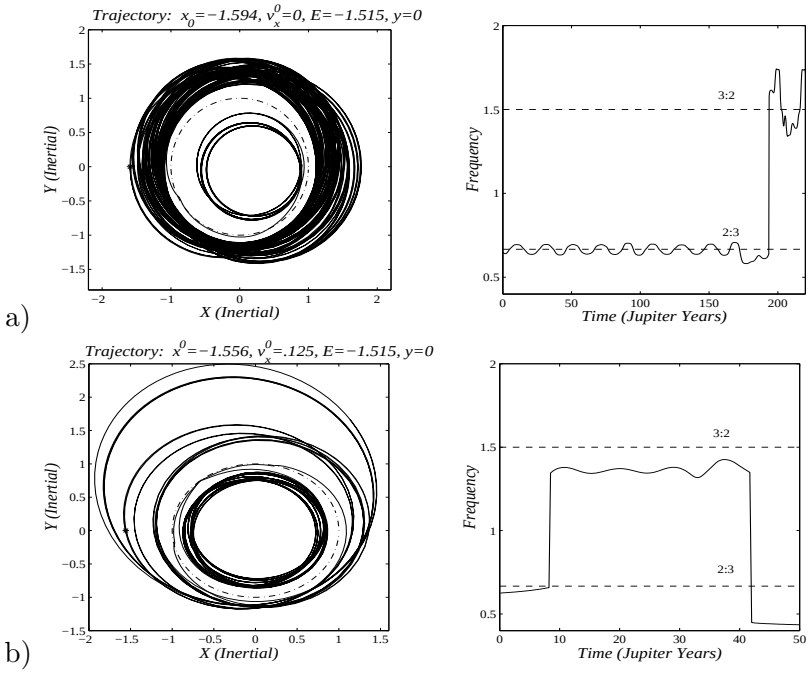

Figure 4.5: Examples of trajectories and the corresponding frequency evolution. The orbits are represented in the inertial frame. The dotted line is the orbit of Jupiter. The frequency evolution is in ratio with the frequency of Jupiter. We have indicated the lines of the 2:3 and 3:2 resonances for reference. Note that the trajectories that go from the exterior region to the interior region "visit" the previous resonances.

The time-varying frequency reflects accurately the behavior of the solution. Recall that the initial conditions were taken with $y = 0$ and $x < -1$ in the exterior region, on the opposite side to Jupiter (see Figure 4.1). The trajectory in Figure 4.5 a) corresponds to an initial condition close to the island of 2:3 resonance, that is "trapped" around the island for some time. During this period of time, the trajectory behaves almost regularly (as we can see in the plot of the orbit in inertial coordinates). But at some point in time around 170 Jupiter years, the trajectory is "released" from the resonance. We say that this trajectory featured a *resonance trapping*. Such concept is possible due to the good accuracy in the computation of the instantaneous frequencies of this method.

In the same way, we are able to determine *resonance transitions*. The trajectory in Figure 4.5 b) corresponds to an orbit that evolves from the exterior region, close to the island of 2:3 resonance, to the interior region, passing nearby the island of 3:2 resonance; and then to the exterior region again going towards the 1:2 resonance.

4.4.2 Resonance trappings, resonance transitions and transport

We see that many trajectories that evolve from the exterior region to the interior region of the Solar system also feature a resonance transition between the 2:3 and 3:2 resonance islands. This in fact can be seen as an implication of the transport mechanism between the exterior and interior region of the Solar system.

Therefore, by looking at the evolution of the frequency, we can determine which trajectories have been exchanged from the exterior region across the Jupiter region to continue evolving in the interior region, or vice versa. Since time-frequency analysis yields the precise time at which a resonance transition happened, we can determine how trajectories are being transported in different regions of the phase space.

In Figure 4.6, we marked in different patterns the initial conditions corresponding to chaotic trajectories that have undergone a resonance trapping during certain intervals of time. In a), the time interval corresponds to the beginning of the evolution; this is $0 < t < 8$ Jupiter years, and we can notice that the trajectories trapped

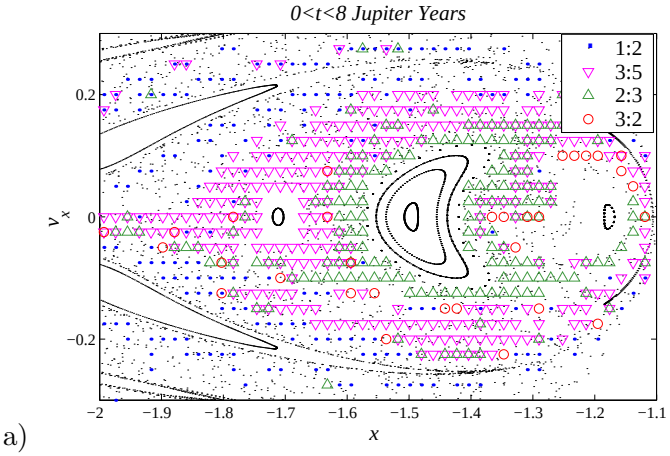

a)

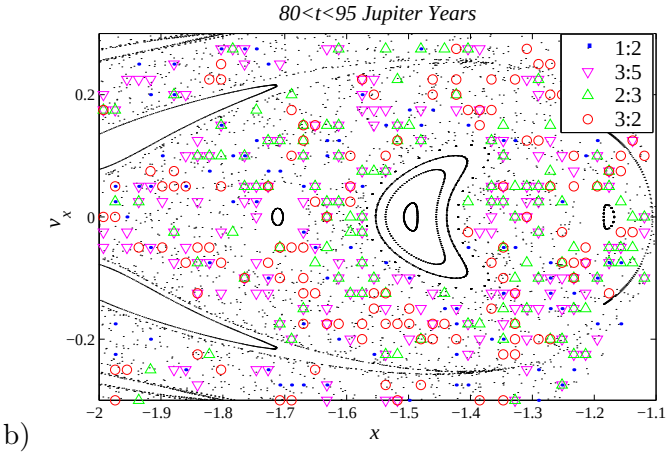

b)

Figure 4.6: Resonance trappings. The marks correspond to initial conditions of orbits trapped in the resonances in the time interval indicated. Recall that the 3:2 resonance is in the interior region. Therefore trapping in this resonance occurs when the trajectory exchanges from the exterior to interior regions.

lie in the region around the resonance islands of that particular resonance. In b), the time interval is $80 < t < 95$ Jupiter years and any trace of regularity has been erased. Note that if an initial condition is marked more than once, it means that a resonance transition has occurred during that time interval. We can also observe that up to this time many trajectories keep exchanging between the exterior and interior region and vice versa.

4.4.3 Rapid transitions

Transitions between the exterior region and the interior region occur when there is a sudden change in frequency. Remember that the frequency of Jupiter is 1. Therefore, a transition occurs when the frequency of the orbit changes from less than 1 to a frequency greater than 1, or vice versa. Therefore, with the frequency map we can detect these transitions.

In Figure 4.7, large dots represent the initial conditions corresponding to trajectories that transition between the exterior region and the interior region during three different intervals of time. The background dots represent the Poincaré map for reference. In part a), the transitions occur in less than three Jupiter years; this is, these are rapid transitions.

Koon *et al.* [23] have shown that the stable manifold of the Lyapunov orbit around L_2 serves as a dynamical channel for capturing orbits: all trajectories that transition from the exterior region to the Jupiter region must be in the interior of the tube formed by this manifold. The first intersection of this manifold in backward time with the Poincaré section $y = 0,\ v_y > 0$ is a closed curve (shown in Figure 4.7 as a thick curve) that we can use as the boundary of the region with the orbits that are going to be captured rapidly into the Jupiter region, and possibly into the interior region. Not all orbits captured in the Jupiter region transition to the interior region: some trajectories can swing around Jupiter and leave towards the exterior region again. Our results agree with the results in [23], since all the rapid transitions have initial conditions in the interior of this curve, as we can see in Figure 4.7 a), where transitions for less than three Jupiter years are represented.

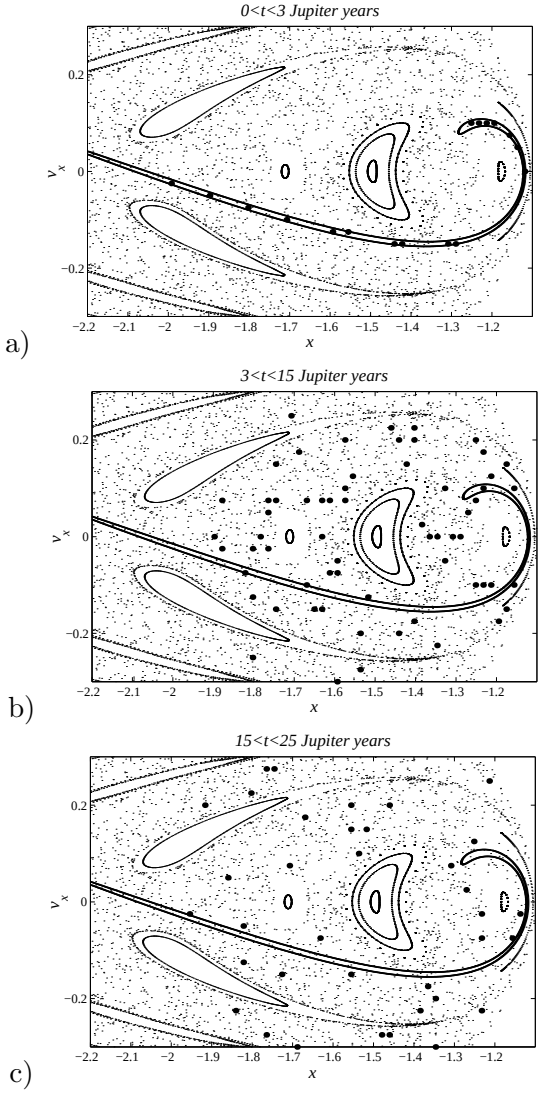

Figure 4.7: The large dots represent initial conditions of orbits that feature rapid transition from the exterior to the interior regions, during the time interval indicated. The thick curve represents the first backward intersection of the stable manifold of the Lyapunov orbit around L_2 with the Poincaré section. The dots in the background correspond to the Poincaré map.

We can observe in parts b) and c) of Figure 4.7 that the distribution of transitions in the time-intervals $3 < t < 15$ and $15 < t < 25$ (Jupiter years) is quite irregular. If we want to use the method of invariant manifolds to obtain all the trajectories that will get captured in the Jupiter region after a number of revolutions in the exterior region, we need to find the successive intersections of the stable manifold of the Lyapunov orbit around L_2 in backward time with the Poincaré section. This is computationally hard due to the extremely complicated dynamics. For instance, intersections of the stable and unstable manifolds of the Lyapunov orbit around L_2 produce foldings and swirls of the manifolds. Furthermore, there is an intrinsic difficulty in the computation of such invariant manifolds for long times.

4.4.4 Number of transitions vs time

Figure 4.8 displays the percentage of trajectories that experience a transition from the exterior to the interior region at a given time; we only considered the first transition of the orbit, and therefore each trajectory is counted only once, although it might evolve back and forth between the two regions afterwards. For this calculation, we divided the total evolution time into subintervals of 8 Jupiter years, and counted how many first transitions occurred in each subinterval. The percentage was calculated with respect to the total number of chaotic trajectories; this is, trajectories in the resonance islands (that remain there for all time) were not considered.

For comparison, the second panel shows the percentage of trajectories that feature a first transition from one of the exterior resonances (2:3, 1:2 and 3:5) to the interior resonance 3:2, as a function of time. Note that the two curves show the same decreasing tendency as time grows. Resonance transitions represent a clear indicator of transport between the two regions.

The decreasing trend of the plots yields a qualitative description of how transitions between the exterior and interior regions happen. If a comet happens to be in the distribution of our initial conditions, and it features a transition, then it is

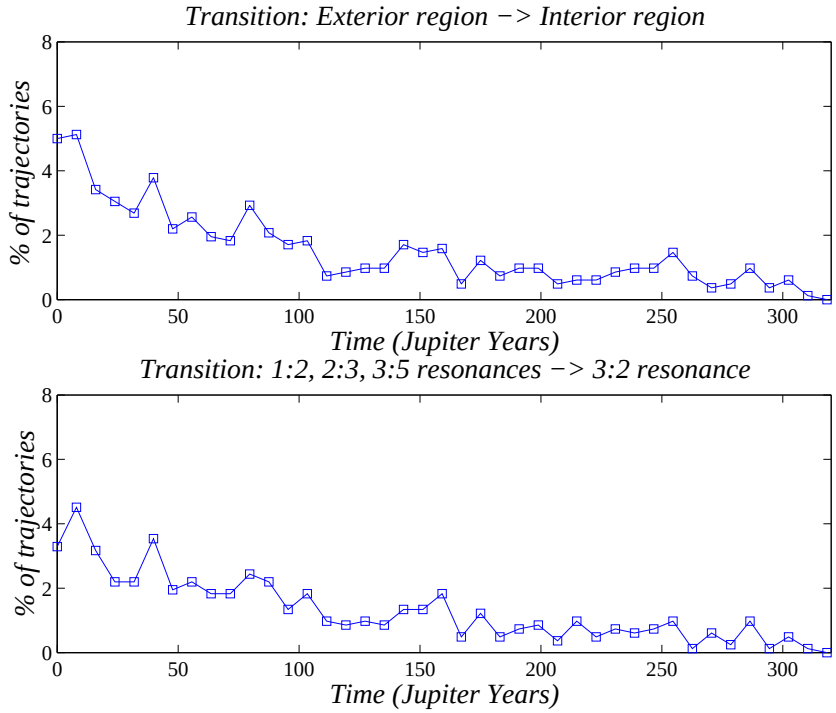

Figure 4.8: Percentage of trajectories that for the first time transition from the exterior region to the interior region as a function of time; and similarly from the outer resonances (2:3, 1:2 and 3:5) to the inner resonance 3:2.

more likely that the comet will exchange towards the interior region within a few Jupiter years; it is less likely that the comet will remain in the exterior region for more than 300 Jupiter years and then transition to the interior region.

4.5 Conclusions

Time-frequency analysis based on wavelets provides a powerful tool to evoke key dynamical features of a system from numerical solutions. From the variation in time of the frequencies calculated from the wavelet transform, we can distinguish quasiperiodic trajectories from chaotic ones. We are able to determine if a chaotic trajectory has been trapped in a resonance, or if it displays a resonance transition.

The method of time-frequency analysis allows us to detect resonance islands

that greatly affect the dynamics. For the PCRTBP, transport in the phase space between different regions was resolved by determining resonance transitions of chaotic trajectories. This was achieved by extracting time-varying frequencies of the orbits in configuration space in the inertial frame.

Our results implicate the same regions that Koon *et al.* [23] use in describing the transport mechanism between the exterior and interior regions of the Solar system and its relation with resonance transitions. However, since our method includes the time variable in the analysis, we are able to determine exactly when resonance transitions take place, and their distribution along the evolution of the system.

We showed that the resonance transitions between three exterior resonances 2:3, 1:2 and 3:5, and the interior resonance 3:2, reflect a great deal of the transitions between the exterior region and the interior region. Although the meaning of these results is limited by the finite number of trajectories considered, and by the bounded time interval that was used for the frequency map, we have shown the strong relation between transport in phase space and resonance transitions in the restricted three body problem. We believe that this work will open a course of research in many high dimensional problems for which the transport mechanism is still to be understood.

Chapter 5

Incomplete Vibrational Energy Redistribution in Highly Excited OCS

Abstract

We determine the dynamics and global phase space structure of the highly excited OCS (carbonyl sulphide) molecule using time-frequency analysis based on wavelets. We perform our study at an energy level close to dissociation in a three-degrees-of-freedom vibrational model of planar OCS. By assigning time-varying frequencies to the time-series representing the solutions, we are able to detect quasiperiodic motion where chaos was believed to be predominant. We show that all quasiperiodic trajectories at this energy are close to a resonance, and therefore they form resonance channels. Our method allows us to keep track of temporary resonance trappings of chaotic trajectories, and we are able to explain transport between different regions of the phase space in terms of trappings in the resonance junctions. We show that resonance trappings and resonance transitions occur even at long times, showing that the energy redistribution is not complete.

5.1 Introduction

Carbonyl sulphide, OCS, one of the most abundant sulphur-containing gases in the stratosphere, is also one of the major components of the overall sulphur cycle

influencing climate [43]. Its prominence in atmospheres is not restricted to the Earth because the infrared spectrum of OCS has been detected in Venus, and it has been associated with reactions with CO at the planetary surface [41]. Because it is such an important molecule, its intramolecular dynamics is of great interest to the scientific community.

Conventional wisdom -widely supported by experiments- asserts that intramolecular vibrational energy redistribution (IVR) is rapid, complete and statistical [28, 39]. It is therefore valuable to add to the few known cases [47] when it is not so. But perhaps, what matters even more are the reasons behind incomplete redistribution, especially beyond the well studied case of two degrees of freedom. This is the purpose of the present work. In the present work we will present evidence that the intramolecular vibrational dynamics of the carbonyl sulfide molecule, OCS, shows incomplete redistribution even when the molecule is excited within ten percent of its dissociation threshold.

The most popular potential energy surface of OCS was obtained by Carter and Brumer [10] from a force field which Foord, Smith and Whiffen [15] constructed to analyze highly excited intramolecular dynamics. The potential surface consists of Morse oscillators for each of the vibrations, and contains strong coupling terms. We perform our analysis on the planar and rotationless version of this molecule which amounts to working with a Hamiltonian with three degrees of freedom (3-dof).

This system is known to be chaotic at total energies close to dissociation [10]. The same model of OCS was analyzed by Martens *et al.* [33], by computing "local frequencies." To this end, they used a short-time (or windowed) Fourier transform. Their method requires that the size of the time-window be determined *a priori*, and as a result, some rapid transitions in frequency, which we will show to be crucial to the intramolecular dynamics, may remain undetected.

The coexistence of chaos and order ("soft chaos" [20]) is a common feature of nonintegrable Hamiltonian systems. The picture of a Poincaré section containing quasiperiodic trajectories and resonance islands surrounded by a chaotic sea is characteristic of systems with 2-dof or periodically forced systems of 1-dof. How-

ever, we lack of techniques for the detection of the global structure of the phase space in 3-dof. Although it is possible to construct a Poincaré map in a 3-dof system, the dimension of the section is four, therefore making it impossible to visualize when projected to three or two-dimensional planes. However, the main difference between 3-dof systems and the 2-dof case is that invariant tori are no longer barriers in the phase space: They are objects of dimension at most three in the five-dimensional energy surface. So, are there any barriers to energy flow beyond 2-dof? Indeed, Martens *et al.* [33] contains a number of speculations concerning the nature of energy flow, many of which are closely linked with the multidimensionality of the OCS model.

In contrast, we use the method of time-frequency analysis based on wavelets. Our method assigns time-varying (instantaneous) frequencies to the numerical solutions (the trajectories). The method is discussed in Chapter 2. With a frequency map so computed, it becomes possible to distinguish regular motion from chaotic motion.

Time-frequency analysis based on wavelets provides an improved resolution of the time evolution of the fundamental frequencies. Indeed, our analysis has resulted in a number of surprising findings; e.g., we can observe how chaotic trajectories can be trapped temporarily in a single nonlinear resonance or in resonance junctions. This is one of our main results.

As a further consequence of the superior accuracy of the time-evolution of the frequencies, we can determine exactly the time interval when a chaotic trajectory is temporarily trapped in a resonance, meaning that the trajectory remains close to a lower dimensional torus during that time-interval. When a resonance transition occurs, the trajectory is trapped by a different resonant torus, indicating an exchange between different regions of the phase space. We use this fact to explain transport in phase space.

Particularly for OCS, we have detected quasiperiodic regions at total energy level that corresponds to 90% of the dissociation energy. Such regions were not suspected before because chaos was assumed to be widespread.

By analyzing the frequencies of the quasiperiodic trajectories, we can see that all quasiperiodic trajectories at this energy belong to some resonance channel: They are located in areas strongly affected by a resonance. Therefore, we have detected the main resonances in the system which have a significant effect in the dynamics. The resonant tori turn out to be responsible for the resonance trappings of many chaotic trajectories; this is, chaotic trajectories can be temporarily trapped near the resonance channels. We study the evolution of the system for 30 ps (although we could observe it longer, too), and we can describe how the resonance trapping along single or double resonances occurs as the system evolves.

We have also detected intriguing motions near the resonance channels. Trajectories with positive Lyapunov exponents (and therefore chaotic) can remain near a resonance channel for long time, behaving almost regularly. This process is reminiscent of "stable chaos" in the Solar system [46].

We believe that the main contribution of time-frequency analysis based on wavelets is that chaotic trajectories are included in the analysis besides the quasiperiodic trajectories. Since we can extract the variation in time of the frequencies with good accuracy, we can determine how transport takes place in phase space. Also, the existence of resonance trappings of chaotic trajectories for long times shows that in some parts of the phase space, the relaxation time can be very long if not infinite.

The outline of this work is as follows. The planar vibrational model of OCS is briefly described in Section 5.2, together with the description of the use of the method of time-frequency analysis based on wavelets. In Section 5.3 we describe how the method allows us to determine the diffusion in the phase space, the resonance channels, the trajectories lying in resonance junctions, and trappings in resonance junctions. We show evidence of transport between the resonance zones and display how fast it takes place. Finally in Section 5.4 we discuss the differences between the method of time-frequency analysis and other methods used before, and the implications of the results for general dynamics of systems with three or more degrees of freedom.

5.2 Hamilton's equations of OCS and analysis of trajectories

5.2.1 The Hamiltonian of OCS

The planar OCS molecule can be modeled as a three body problem with masses m_1, m_2 and m_3 corresponding to the atomic masses of S, O and C (respectively), moving according to a potential function computed to fit spectroscopic data. It is a Hamiltonian system with three degrees of freedom, corresponding to the three variables: Two interatomic distances, and the angle formed by these segments (see Figure 5.1):

$$\begin{aligned} R_1 &= \text{distance C} - \text{S} = R_{\text{CS}}, \\ R_2 &= \text{distance C} - \text{O} = R_{\text{CO}}, \\ \alpha &= \text{angle (CS, CO)}. \end{aligned} \tag{5.1}$$

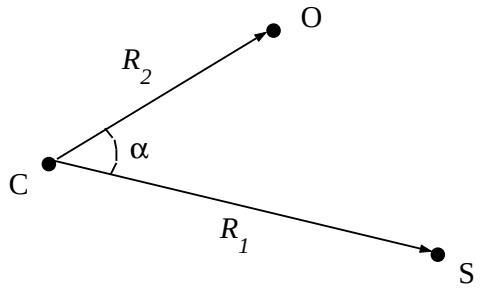

Figure 5.1: OCS molecule.

The third distance R_3 between O and S is given in terms of the previous variables as $R_3 = \sqrt{R_1^2 + R_2^2 - 2R_1R_2\cos\alpha}$.

In Hamiltonian form the system can be expressed as the sum of kinetic energy plus potential energy, where the angular momentum has been fixed as zero. Defining P_1, P_2 and P_α as the momenta conjugate to R_1, R_2 and α, respectively, the

kinetic energy is

$$T = \frac{\mu_1}{2}P_1^2 + \frac{\mu_2}{2}P_2^2 + \mu_3 P_1 P_2 \cos\alpha + P_\alpha^2\left(\frac{\mu_1}{2R_1^2} + \frac{\mu_2}{2R_2^2} - \frac{\mu_3\cos\alpha}{R_1R_2}\right) - \frac{\mu_3 P_1 P_\alpha \sin\alpha}{R_2} - \frac{\mu_3 P_2 P_\alpha \sin\alpha}{R_1}.$$

The parameters μ_i are related to the atomic masses of the system by

$$\mu_1 = \frac{m_1+m_3}{m_1m_3}, \qquad \mu_2 = \frac{m_2+m_3}{m_2m_3}, \qquad \text{and} \quad \mu_3 = \frac{1}{m_3}.$$

The potential energy function of OCS was obtained by Carter and Brumer [10] from a force field by Foord, Smith and Whiffen [15] used to analyze highly excited intramolecular dynamics. The potential surface includes Morse potentials for each diatomic and an interaction term,

$$V = V_1(R_1) + V_2(R_2) + V_3(R_3) + P(R_1,R_2,R_3)V_{I1}(R_1)V_{I2}(R_2)V_{I3}(R_3),$$

where $V_k(R_k) = D_k(1-e^{-\beta_k(R_k-Ri_k)})^2$, P is a quartic polynomial, and $V_{Ik}(R_k) = 1-\tanh[\gamma_k(R_k-\tilde{R}_k)]$; $\tilde{R}_k$ are the coordinates of the equilibrium position. This is a collinear configuration ($\alpha=\pi$) with $\tilde{R}_1 = 2.9508$, $\tilde{R}_2 = 2.2030$, and $\tilde{R}_3 = \tilde{R}_1+\tilde{R}_2$. In Figure 5.2, the contours of the potential function are shown for the collinear case, $\alpha=\pi$.

The equilibrium point with coordinates $P_k = 0$, $R_k = \tilde{R}_k$ is an elliptic fixed point of the system. The purely imaginary eigenvalues lead to the normal frequencies of 2089.14, 874.261 and 520.843 cm^{-1}.

5.2.2 Time-frequency analysis of OCS

In Chapter 2, we defined the instantaneous frequency and described how it can be extracted from a time series representing a numerical solution using the wavelet transform. We will use these concepts to extract the basic frequencies of the numerical solutions of planar OCS and compute a frequency map. With this, a characterization of the dynamics in phase space in terms of regular and chaotic

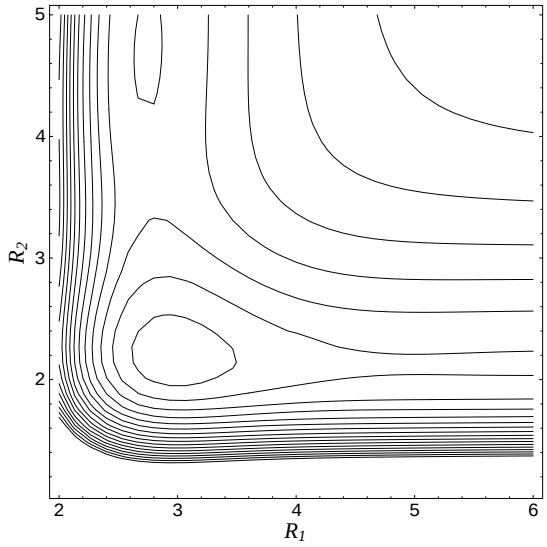

Figure 5.2: Contours of the potential energy function, for the collinear case $\alpha = \pi$.

motion, resonance channels, resonance trappings, and diffusion in phase space, becomes possible.

Frequency map

The frequency map for OCS is obtained by the following procedure.

- For a given initial condition (R_1^0, R_2^0, α^0), we obtain the solution as three time series corresponding to each dynamical variable of the system (5.1): $R_1(t)$, $R_2(t)$ and $\alpha(t)$, over a time interval $[0, T]$, in our case $T = 30\,\text{ps}$.

- Then we construct analytic signals for each of them by computing the Hilbert transform, obtaining three complex time-series: $z_1(t) = R_1(t) + i\,H[R_1](t)$, $z_2(t) = R_2(t) + i\,H[R_2](t)$, $z_3(t) = \alpha(t) + i\,H[\alpha](t)$ (see Equation (2.10)).

- For each $z(t)$, we extract the instantaneous frequency over the interval $[0, T]$ using the wavelet transform, obtaining the frequency-series $\omega_1(t)$, $\omega_2(t)$, $\omega_3(t)$.

- The frequency map is then

$$(R_1^0, R_2^0, \alpha^0) \Longrightarrow (\omega_1, \omega_2, \omega_3)(t), \quad t \in [0, T].$$

If the trajectory is quasiperiodic, the frequencies are constant in time, and this value is what Fourier analysis would give. On the other hand, if the trajectory is chaotic, the instantaneous frequency will show great variation in time with respect to its mean value.

The deviation of the frequency $\omega(t)$ from its mean value $\widetilde{\omega}$ yields a measure of how chaotic the trajectory is. We call this measure the "diffusion" of the trajectory over $[0, T]$:

$$\text{diffusion}\,(R_1^0, R_2^0, \alpha) = dev_1 + dev_2 + dev_3, \tag{5.2}$$

where

$$dev_k = \frac{1}{T}\int_0^T |\omega_k(t) - \widetilde{\omega}_k| dt.$$

Quasiperiodic trajectories will have zero diffusion, whereas chaotic trajectories will have high diffusion.

We performed time-frequency analysis at total energies close to dissociation, which is .1 a.u. The energies analyzed here were .085 a.u., and .09 a.u., which are 85 and 90% of the dissociation energy. Since the results obtained are qualitatively similar for both energies, we only show the computations at the energy level .09 a.u.

The initial conditions were chosen in a slice of the phase space corresponding to zero momenta, $P_1 = P_2 = P_\alpha = 0$. The values of R_1 and R_2 are chosen at a regular grid on the plane R_1, R_2 and α is calculated to fit the energy level. We used 100 grid-points in the R_1 axis and 80 grid points in the R_2 axis.

Note that we define the frequency map for OCS by computing the instantaneous frequency associated with the position coordinates R_1, R_2 and α, and this definition does not involve the momenta P_1, P_2 and P_α. The justification for proceeding this way is the following. Recall that for quasiperiodic trajectories, we can find an approximation by a trigonometric polynomial of the form (2.6). The

values λ_m^j are linear combinations of the basic frequencies ω_1, ω_2, ω_3 that describe the quasiperiodic torus (see Section 2.2). Our analysis consists of finding only the first frequencies λ_m^j associated with the position coordinates, and the frequencies associated to momenta P_k are implicitly included in these values; the exact values of the basic frequencies ω_k can be found by looking for all the frequency components and harmonics for each variable (we can apply Laskar's method [25] for this purpose, knowing in advance that the trajectory is quasiperiodic). Therefore, by considering only frequencies of the position coordinates and not the momenta, we simplify the analysis and, most of all, this allows us to assign time-varying frequencies to all trajectories, not only quasiperiodic ones.

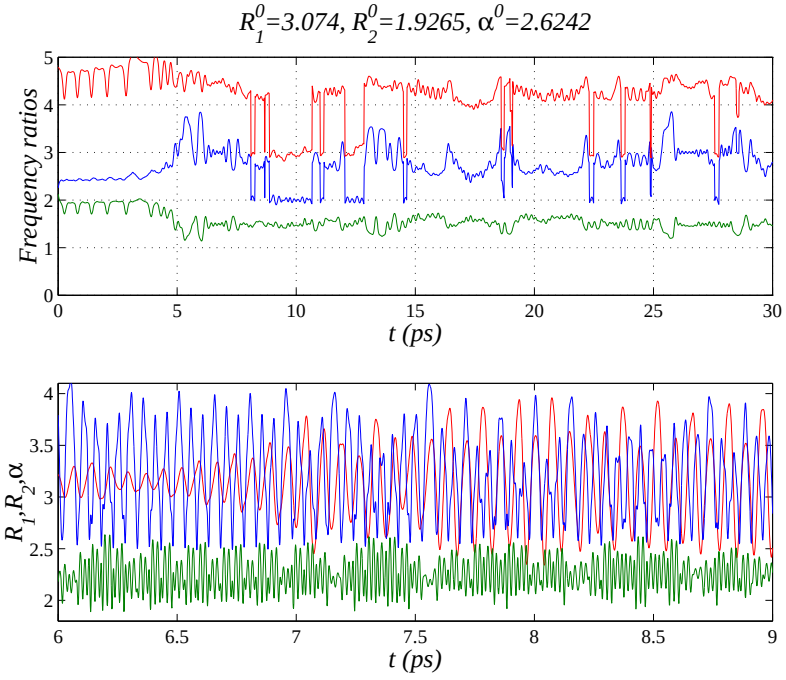

Figure 5.3: Typical chaotic trajectory with large diffusion. The first plot shows the frequency ratios, ω_2/ω_1 in blue, ω_1/ω_3 in green, and ω_2/ω_3 in red. In the second plot, a detail of the trajectory is shown, this is, the evolution of $R_1(t)$ (blue), $R_2(t)$ (green) and $\alpha(t)$ (red).

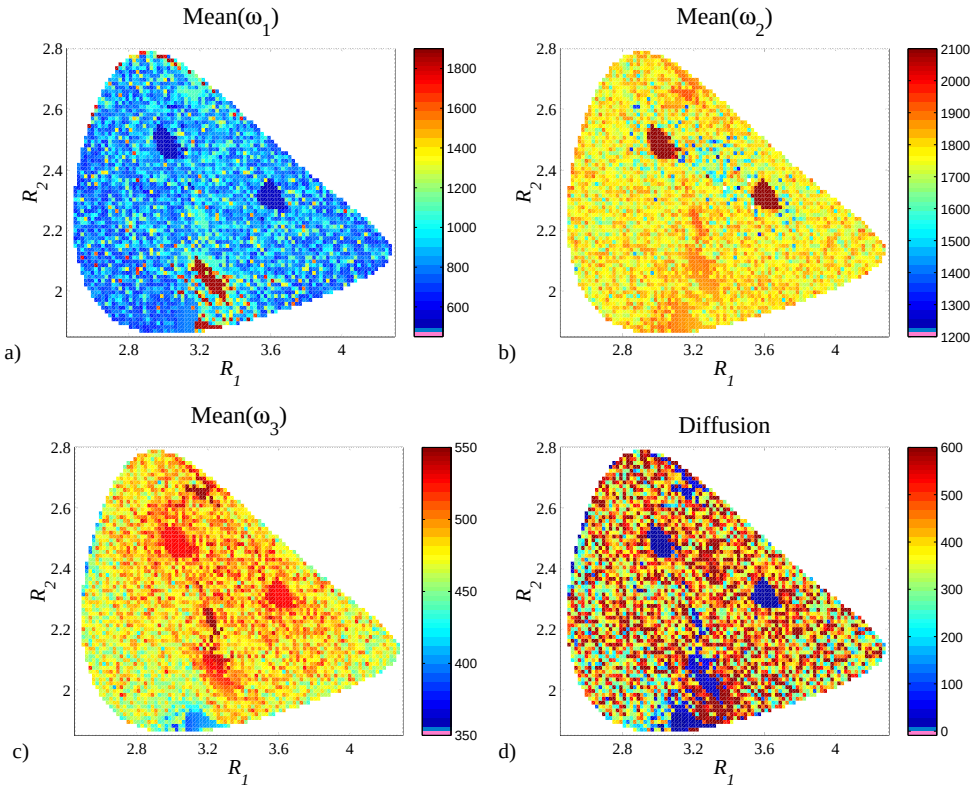

Figure 5.4: Mean frequencies $\widetilde{\omega}_1$, $\widetilde{\omega}_2$ and $\widetilde{\omega}_3$ (a-c) and diffusion (d) for the total integration time of 30 ps.

5.3 Results

5.3.1 Generic aspects of the phase space

At this high vibrational energy, the generic trajectory is chaotic. In Figure 5.3 we show the time evolution of the frequency ratios of a chaotic trajectory (ω_1/ω_2, ω_1/ω_3 and ω_2/ω_3), and in the second subplot a section of the evolution of R_1, R_2 and α is plotted. Notice the rapid and frequent changes of frequency in each of the motions.

The results of wavelet-frequency analysis are displayed collectively in Figure 5.4. Each initial condition is indicated in the plane R_1, R_2, in a), b) and c) we show in color code the mean value of the frequencies, $\widetilde{\omega}_1$, $\widetilde{\omega}_2$ and $\widetilde{\omega}_3$, associated with each variable $R_1(t)$, $R_2(t)$ and $\alpha(t)$, respectively; and d) shows the diffusion associated with the trajectory (Equation (5.2)).

We note from the diffusion plot in Figure 5.4 d) that most of the slice is filled with chaotic trajectories, some of them strongly chaotic: very large diffusion means that the frequencies vary greatly, and this can be interpreted as trajectories wandering through most of the phase space.

It is also possible to identify in Figure 5.4 some islands of stability, i.e., regions of initial conditions in which the diffusion is zero or very low and the frequencies have about the same mean value (see for instance a small spot around $(R_1, R_2) = (3.6, 2.3)$). These regions correspond to quasiperiodic trajectories, and by computing the frequency ratios we can determine if they are resonant or not.

Recall that for the quasiperiodic orbits the mean value of the instantaneous frequency corresponds to the fundamental frequency that Fourier analysis would render. Therefore, we can talk about resonances in the traditional sense: a resonance is determined when a trajectory has zero diffusion and its frequencies satisfy an equation of the form

$$k_1\widetilde{\omega}_1 + k_2\widetilde{\omega}_2 + k_3\widetilde{\omega}_3 = 0, \tag{5.3}$$

where k_1, k_2, k_3 are integers.

5.3.2 Resonance channels

Using time-frequency analysis we can find the initial conditions giving rise to trajectories with very low diffusion, and satisfying a resonance equation up to certain tolerance. We set the tolerance value to include trajectories that are strongly affected by the resonance. These trajectories form a resonance channel.

We tested for resonances using the following expression,

$$\left| \frac{\omega_k(t)}{\omega_j(t)} - \frac{p}{q} \right| < \varepsilon,$$

where ε is a tolerance value that we chose to be .15, and p, q are integers.

All quasiperiodic trajectories form resonance channels

Typically, KAM tori are half the dimension of the phase space. We found that all quasiperiodic trajectories (this is, trajectories with very low diffusion during the 30 ps of evolution) have frequencies which satisfy a resonance equation up to the tolerance value. This is, for OCS at this energy, all the invariant tori that remain are located around a resonance, and they form what we can identify as a higher dimensional resonance island.

The resonance channels of planar OCS are shown in the center of Figure 5.5. In this figure the most important resonances in the system are marked with different colors and symbols. We found single resonances and resonance junctions, that is, frequencies satisfying one or two independent resonance equations respectively (in the case of double resonance we wrote also a third non-independent relation between the frequencies for completeness). For instance the 1:1 resonance between R_1 and R_2, i.e., trajectories with frequencies satisfying $\widetilde{\omega}_1 = \widetilde{\omega}_2$ are marked with magenta stars. (From now on, we drop the tildes denoting the mean frequencies in the understanding that for quasiperiodic trajectories the mean value of the instantaneous frequency corresponds to the fundamental frequency).

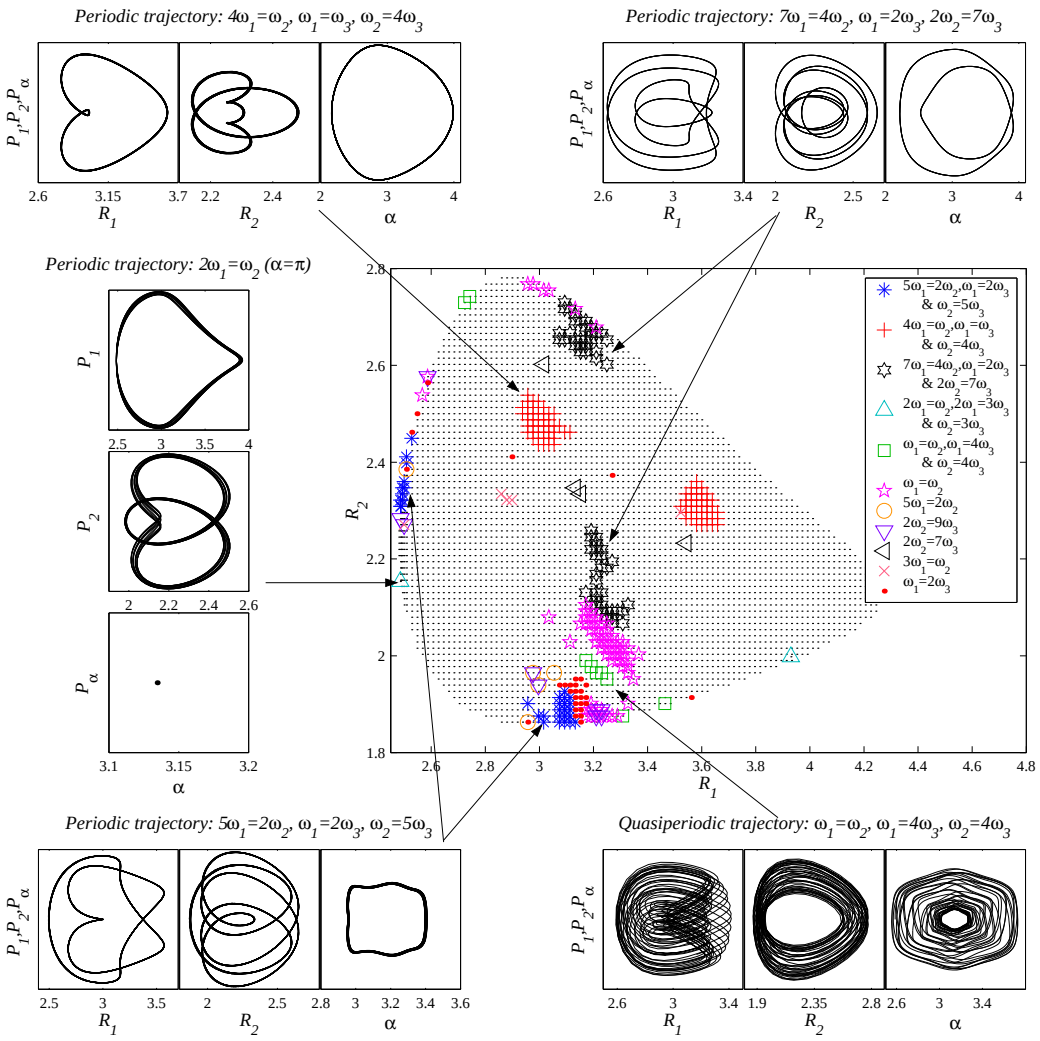

Figure 5.5: Resonance channels: Periodic and quasiperiodic trajectories with resonant frequencies. We show the most important resonance junctions and single resonances. Representative trajectories very close to the periodic orbits in the resonance junctions are plotted. See text for more details. The trajectories were projected on the planes of motion (R_1, P_1), (R_2, P_2), (α, P_α).

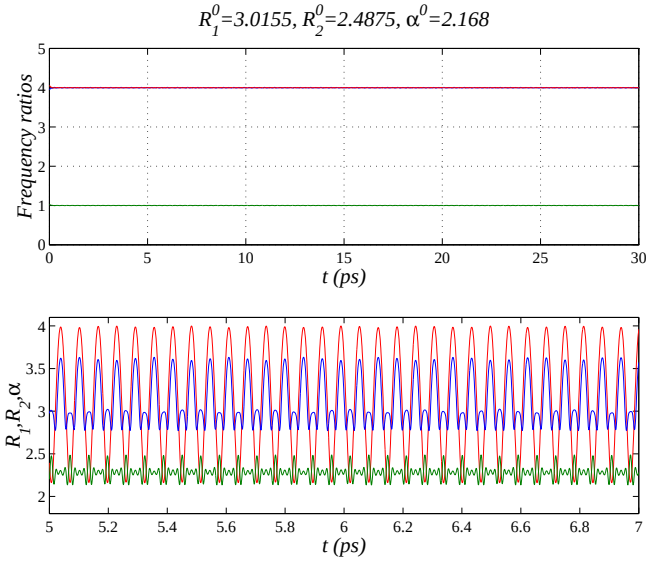

Figure 5.6: Trajectory satisfying $4\omega_1 = \omega_2$, $\omega_1 = \omega_3$ and $\omega_2 = 4\omega_3$ for 30 ps. The assignment of colors is the same as in Figure 5.3.

5.3.3 Trajectories in the resonance junctions: Long-time trapping

Resonance channels describe the quasiperiodic motions in the system. Lower dimensional tori are created by resonances, i.e., if a trajectory satisfies exactly a single resonance equation, then it lies on a two-dimensional torus. The surrounding quasiperiodic trajectories that are close to that resonance lie on tori of dimension three. On the other hand, if a trajectory satisfies exactly a double resonance, then it lies on a one-dimensional torus (a periodic orbit at the intersection of the resonances); and it is surrounded by a set of trajectories satisfying closely the double resonance. These trajectories lie on higher dimensional tori. Recall that when the energy is fixed, the phase space is five-dimensional, and 3-tori cannot be barriers of the motion. Therefore, the resonance channels do not divide the phase space, and chaotic trajectories can wander around them.

Stable periodic orbits of OCS are then found as trajectories lying on the resonance junctions. See, for instance, in Figure 5.6 the evolution in time of the

frequency ratios and the variables R_1, R_2, α. This particular trajectory lies almost exactly at the resonance junction $4\omega_1 = \omega_2$, $\omega_1 = \omega_3$ (and then it also satisfies closely $\omega_2 = 4\omega_3$).

The panels around the central panel in Figure 5.5 show some representative trajectories with frequencies satisfying closely the resonance junctions. In each case, the trajectories have been projected on each of the planes of motion (R_1, P_1), (R_2, P_2), and (α, P_α). We note that these trajectories are very close to the periodic solution that lies exactly at the resonance junction. Note, however, that the trajectory corresponding to $\omega_1 = \omega_2$, $\omega_1 = 4\omega_3$, $\omega_2 = 4\omega_3$ (marked with green squares) is closed to a quasiperiodic torus of dimension two instead. The discrepancy is a result of our simplification: We are only computing one frequency component for each degree of freedom (see Section 2.6), and in this case more components need to be taken into account to find another independent frequency; this trajectory has in reality a Fourier spectrum with two independent frequencies.

5.3.4 Are the resonances connected? The absence of a web

Note also in Figure 5.5 that the resonance channels are isolated. Indeed, this is an important difference from the so-called Arnol'd web [1], which is characteristic of near-integrable systems. At this energy level of OCS, we see that the resonances appear as separated spots in the phase space, and their pattern is not a web but an archipelago. As a consequence, the phase space structure here is fundamentally different from the typical Arnol'd web of nearly integrable systems.

A remarkable feature of OCS is how abruptly chaotic trajectories can jump between resonances. To see this, we show in Figure 5.7 the evolution of the frequency ratios of a particular trajectory, and in part b) we can see how the trajectory jumps from $\omega_1 = \omega_2 = 4\omega_3$ to the resonance $2\omega_1 = 3\omega_3$, and after that is captured also in the $\omega_2 = 3\omega_3$ resonance. Therefore, the diffusion in OCS does not occur slowly along the resonance channels, as would happen in a near-integrable system [3], but the diffusion involves almost instantaneous jumps in the frequencies from one resonance to another.

5.3.5 Analysis of resonance trappings

The analysis of chaotic trajectories is possible due to our superior accuracy in the tracking of the evolution of the frequencies. We observe that chaotic trajectories with large diffusion can be trapped temporarily in single resonances and resonance junctions.

For instance, Figure 5.8 shows the time evolution of the frequency ratios for two chaotic trajectories; in a), the trajectory is trapped temporarily in the 1:2 resonance between R_1 and R_2 ($2\omega_1 = \omega_2$) and simultaneously in the 3:2 resonance between R_1 and α ($2\omega_1 = 3\omega_3$). In b), the trajectory is trapped temporarily in the junction $\omega_1 = 2\omega_3$ and $2\omega_2 = 7\omega_3$.

Therefore, time-frequency analysis allows us to keep records of all the resonance trappings that the trajectories can sample during the time interval in question. Or, from a different point of view, it allows us to take a snapshot of the system at a given time in terms of the resonance trappings.

5.3.6 Evolution of resonance trappings

In Figure 5.9 we show how the resonance trappings due to the resonance junction $\omega_1 = 2\omega_3$, $2\omega_2 = 7\omega_3$ evolve in time. The way to read these figures is the following: If a particular trajectory happens to be trapped in a resonance junction during that interval of time, we mark the initial condition accordingly. In part a), the trappings correspond to the beginning of the evolution, this is for $0 < t < .5$ ps. Recall that the time-frequency analysis was performed for a total time interval of 30 ps, so here we are only considering the trappings at the very beginning of the evolution. Parts b) and c) correspond to the intervals $1 < t < 1.5$, $5 < t < 5.5$.

We see in Figure 5.9 that the distribution of resonance trappings varies considerably during the evolution of the system. Only 5 ps later, many of the initial conditions that were initially close to a resonance have drifted away from the resonance junction, and other trajectories that were initially away from the resonance junction have been trapped.

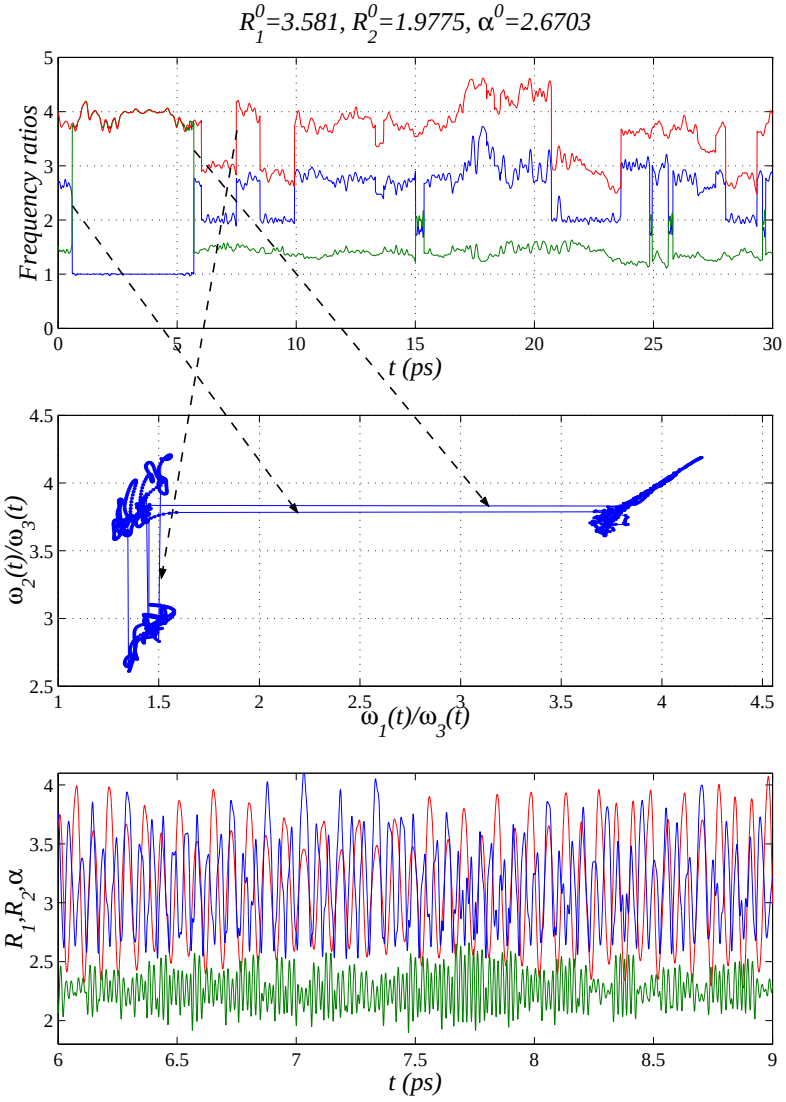

Figure 5.7: Trajectory with large diffusion temporarily trapped in the resonance junction $\omega_1 = \omega_2 = 4\omega_3$, and jumping close to the resonance junction $2\omega_1 = 3\omega_3$ and $\omega_2 = 3\omega_3$. In b) we can observe how the trajectory jumps almost instantaneously between the resonances. The assignment of colors is the same as in Figure 5.3.

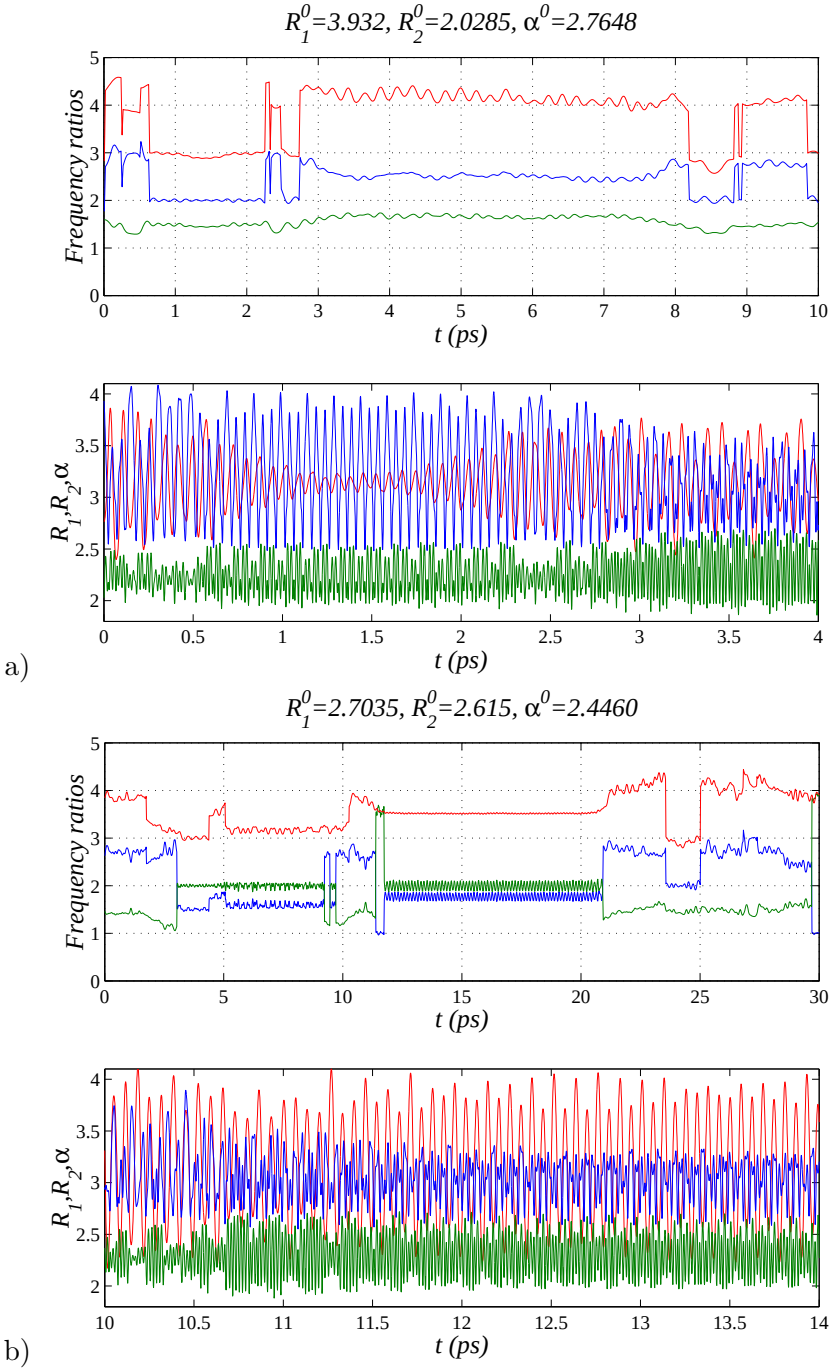

Figure 5.8: Examples of resonance trappings. The assignment of colors is the same as in Figure 5.3.

The time evolution of the frequencies can give us a very good idea of the transport occurring in the system: trajectories evolve through the phase space and can be trapped in a resonance junction, meaning that they are close to one of the periodic orbits living on the resonance junctions; therefore, we know the location in the phase space and how the trajectory exchanges between different regions. This sort of detailed analysis would have been impossible with other methods.

5.3.7 Histograms of resonance trappings

We note that the resonance trappings and resonance transitions persist even after long evolution of the system. The chaotic nature of the system prevails and as far as 30 ps, the system does not show relaxation in any of the variables of motion.

To see this more clearly, we have computed the number of trajectories that are trapped in the main resonance junctions (shown in Figure 5.5) per interval of time. The resonance junctions considered correspond to the most important resonance channels obtained as trajectories with low diffusion and with frequencies satisfying a double (hence triple) resonance equation.

We show the results of this computation in the first panel of Figure 5.10. We note characteristic asymptotic behavior: the junction corresponding to $4\omega_1 = \omega_2$, $\omega_1 = \omega_3$ and $\omega_2 = 4\omega_3$ (red crosses) tends to a constant value of about 2%. Similarly, the junction $\omega_1 = \omega_2$, $\omega_1 = 4\omega_3$ and $\omega_2 = 4\omega_3$ (green squares), tends to a value of about 1%.

We can observe that the most important resonance junction in terms of number of trappings corresponds to the channel $2\omega_1 = \omega_2$, $2\omega_1 = 3\omega_3$ and $\omega_2 = 3\omega_3$ (blue triangles). However, this channel is only present in two initial conditions in Figure 5.5. We have observed that trajectories nearby this initial condition drift away very soon; however, many other chaotic trajectories are trapped temporarily in this resonance junction, thus accounting for the initial rise.

Our analysis suggests that at long times, two types of trajectories can be distinguished: The quasiperiodic trajectories living right at the resonance channels

(with zero or very low diffusion), and the chaotic trajectories that can be trapped temporarily around the resonance junction. However, in these statements, we are limited by our 30 ps integration time.

Once we distinguished between quasiperiodic and chaotic trajectories, we can obtain the number of temporary trappings as a function of time. For this, we leave out the quasiperiodic trajectories, and we compute the percentage of chaotic trajectories trapped around each junction out of the total number of chaotic trajectories detected. The results are shown in the second panel of Figure 5.10.

It is interesting to note that the junction corresponding to $4\omega_1 = \omega_2$, $\omega_1 = \omega_3$ and $\omega_2 = 4\omega_3$ (red crosses) now has an asymptotic value close to zero, meaning that very few chaotic trajectories can be trapped by this resonance junction within our integration time, and the 2% value that we obtained in the previous calculation corresponds entirely to quasiperiodic trajectories living right at this junction.

On the other hand, the junction $\omega_1 = \omega_2$, $\omega_1 = 4\omega_3$ and $\omega_2 = 4\omega_3$ (green squares) tends to a value of about 1% when we leave out the quasiperiodic trajectories. Therefore, there is no decrease in the number of trappings at this junction.

The percentage of trajectories trapped at a resonance junction at a given time shows that the mechanism of resonance trappings may have a noticeable effect in the global dynamics of the system at long times.

5.3.8 "Stable chaos"?

We have established that some chaotic trajectories are trapped in single or double resonances for long periods of time (see Figure 5.11). There are trajectories which started nearby a resonant island, and remained there for long periods of time. We can compute the empirical Lyapunov exponents to check that effectively the trajectories are chaotic, but their frequencies remain close to a resonance. Related observations, mainly in asteroid orbits in celestial mechanics, go under the term "stable chaos" [46]. That we reproduce the hallmarks of stable chaos in a bona-fide 3-dof system rather than a near-integrable one is surprising and opens a new path of research along this line: there are regions in the phase space for which the

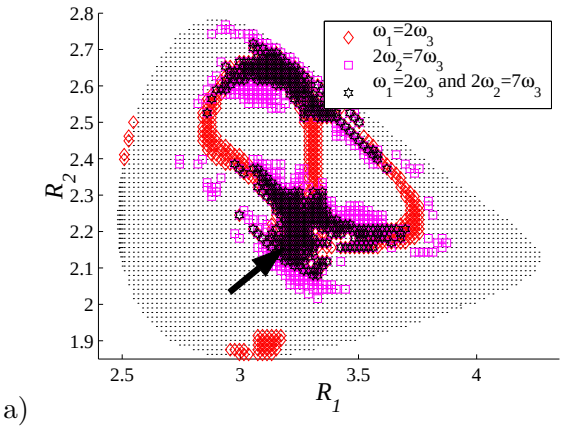

a)

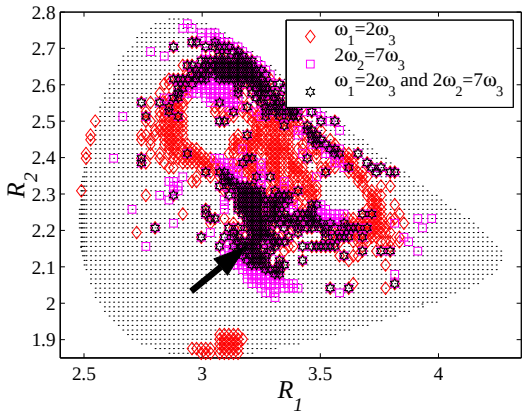

b)

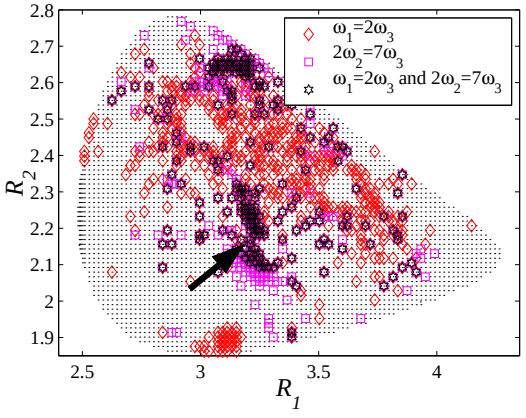

c)

Figure 5.9: Resonance trappings for different intervals of time: a) $0 < t < .5$, b) $1 < t < 1.5$ and c) $5 < t < 5.5$ (ps). The arrow points towards initial conditions living in this resonance junction up to 30 ps.

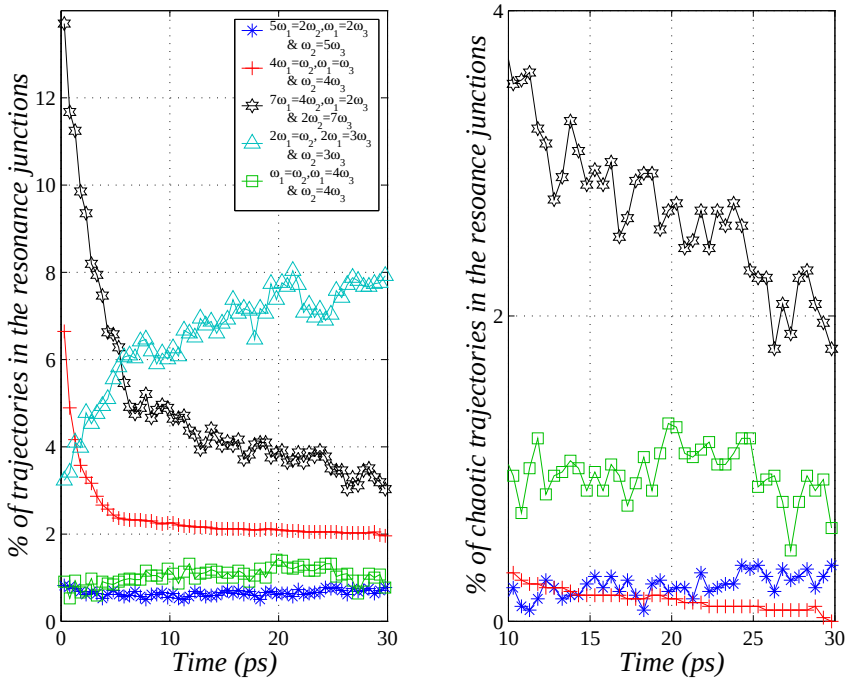

Figure 5.10: The first panel shows the percentage of trajectories that are trapped in the resonance junctions of Figure 5.5 as a function of time. In the second panel, we consider only temporary trappings, i.e. trappings of chaotic trajectories. See text.

trajectories behave in a quasi-regular way for a long time, and do not participate in the chaotic redistribution of energy. These trajectories should have a lifetime of $1/\lambda$ before leaving the region around the resonant torus, where λ is the largest Lyapunov exponent, but instead they remain close to the periodic orbit for much longer.

5.4 Conclusions and discussion

We have shown, based on intramolecular dynamics of OCS, that time-frequency analysis based on wavelets is a powerful tool to determine the global phase space structure of Hamiltonian systems beyond 2-dof. The introduction of the time variable in the analysis of the frequencies associated with trajectories in a convenient way was achieved by using the wavelet transform instead of the Fourier transform as it has been done so far in Hamiltonian systems. Our frequency map consists of the assignment of time-varying frequencies extracted from the numerical solutions, therefore including the chaotic trajectories in the analysis together with the quasiperiodic trajectories.

The automatic localization in time that the wavelets provide allows us to obtain a better resolution in the time-variation of the frequencies; therefore, we can locate with precision when a resonance trapping has occurred. This is very useful since it is easy to observe that resonance transitions are closely related to transport in the phase space.

The property of the wavelets to adapt automatically the time-window to the frequency range is the main advantage of the present analysis over the frequency analysis that has been performed before. For instance, in [34], a "short time" Fourier transform was used to extract the basic frequencies. They chose a time window of length 1.4 ps to obtain time-varying frequencies of three dynamical variables that have very different frequency ranges, and some rapid transitions in frequency were missed. Wavelet analysis avoids the arbitrary determination of the time-window, since it is chosen according to the frequency.

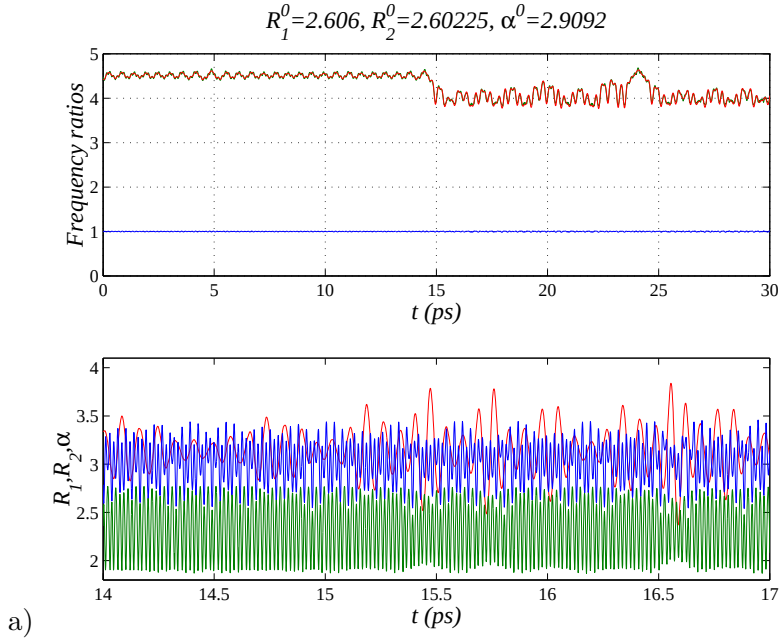

a)

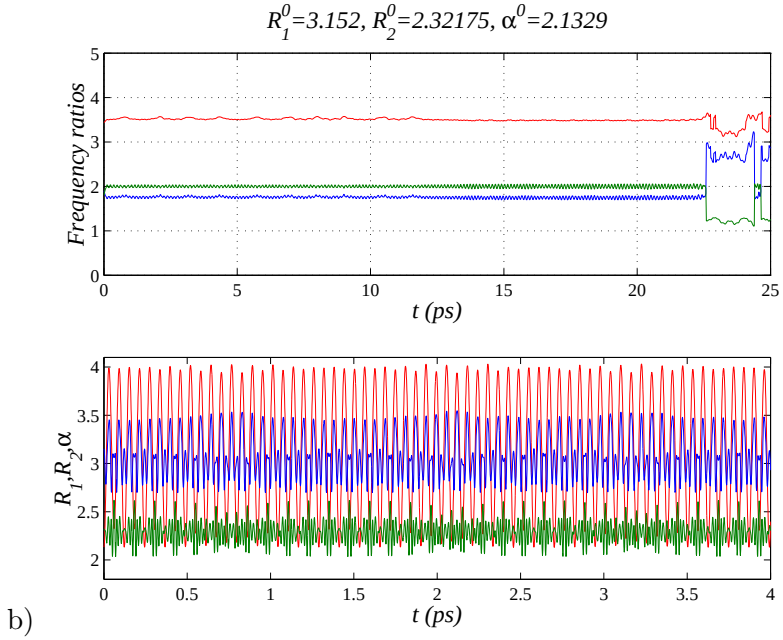

b)

Figure 5.11: Chaotic trajectories trapped in a resonance for long periods of time, illustrating "stable chaos." The assignment of colors is the same as in Figure 5.3.

Using time-frequency analysis we were able to locate quasiperiodic trajectories in the phase space, all of them lying on resonant islands. Therefore, we find no evidence of existence of KAM tori characterized by quasiperiodic motions with rationally independent frequencies other than the trajectories surrounding the resonances. For the OCS Hamiltonian, the resonant islands are surprisingly persistent at high levels of the energy.

Although it has been claimed that KAM tori might act as bottlenecks [34] for the dynamics, possibly as part of a higher dimensional invariant surface, it is well known that three-dimensional tori cannot be a barrier in the five-dimensional phase space. Furthermore, all the tori found in OCS at the energy level studied satisfy a single or double resonance condition up to a tolerance value. Therefore, all quasiperiodic motion occurs in resonant islands around a lower dimensional tori. Even when the dimension of a resonant torus is one or two, we see that they affect the dynamics of chaotic trajectories since resonance trappings are produced.

We have determined that some of the main resonances in a slice of the phase space, shown in Figure 5.5, turn out to be resonance junctions. Comparing with the results of [34], we see that we have detected all resonances mentioned by them like $2\omega_1 = 3\omega_3$, and $4\omega_1 = \omega_2$. We found some more resonances that are important in terms of the trappings, like $2\omega_1 = \omega_2$, $\omega_1 = 4\omega_3$, or $\omega_1 = 2\omega_3$; also there are higher order resonances like $7\omega_1 = 4\omega_2$ and $5\omega_1 = 2\omega_2$. A closer comparison with the results in [34] is not possible since the initial conditions in their analysis are not mentioned.

Since we have shown the existence of regions with quasiperiodic trajectories, the ergodicity assumption of intramolecular energy transfer is violated and we cannot expect that the trajectories have a random behavior: the resonance islands produce trappings that keep chaotic trajectories from participating in a uniform distribution through the phase space.

We found a prevalent pattern in the chaotic trajectories: at some point of the evolution, they can be trapped in a resonance, meaning that for some interval of time their frequencies satisfy approximately a resonance equation. In this sense,

we can think of the resonance channels as "sinks" (loosely speaking), since trajectories passing by the resonance channel are "attracted" by the resonance and remain there for a period of time, and leave afterwards to wander around chaotic areas or to get trapped again by another resonance. Although there is no theoretical justification at present, this mechanism has been related to the "stickiness" phenomenon of resonant islands [35, 36], and it has been observed in a large number of systems, especially in celestial mechanics [46]. The stickiness phenomenon has also been invoked to explain the existence of chaotic trajectories that remain nearby a resonance channel for long periods of time. Thus, there are trajectories that behave almost regularly, but that have positive Lyapunov exponents. So we have given evidence of existence of stable chaos in chemical physics.

We observed that diffusion in this energy level can occur very quickly, since there are trajectories that jump almost instantaneously from one resonance to another one. This of course does not resemble how Arnol'd diffusion takes place in nearly integrable Hamiltonian systems, in which trajectories diffuse slowly along the resonance channels.

Finally, we believe that the main contribution of time-frequency analysis based on wavelets is the inclusion of the chaotic trajectories in the analysis besides the quasiperiodic trajectories. The value of such a procedure for highly excited systems is obvious: Since we can extract the variation in time of the frequencies with a good accuracy, we can determine how trajectories are transported in the phase space. Also, the existence of resonance trappings of chaotic trajectories for large time values shows that the relaxation time can be very long if not infinite.

Chapter 6

General Conclusions

The main motivation for this work was the development of new techniques of analysis of higher dimensional Hamiltonian systems. The difficulty in analyzing these problems becomes clear from the dynamical differences that systems of 3-dof feature when compared with the well understood case of 2-dof. There are many open questions for non-integrable systems of 3 or more degrees of freedom, and we believe that the method we presented is an important tool in the search for answers.

We have presented the new method of time-frequency analysis based on wavelets. The method allows us not only to distinguish chaotic from quasiperiodic systems, but also to obtain a general description of the dynamics in the phase space.

By introducing the time variable in the analysis, our method allows us to characterize chaotic motion that is responsible for intrinsic transport in the phase space. We have shown close relation between resonance transitions and transport between different regions.

This analysis allows us to describe with much detail the main dynamical features of higher dimensional systems: quasiperiodic trajectories forming resonance channels can persist up to high values of the energy where chaos is thought to be widespread. Furthermore, the resonance channels affect greatly the dynamics of chaotic trajectories: chaotic trajectories can be trapped around a resonance

channel, or wander between different resonances.

Time-frequency analysis based on wavelets is a unique tool to determine resonance trappings and resonance transitions of chaotic trajectories; and we have shown their implications in the transport mechanism.

We have shown that the method is successfully applied to systems that vary from molecular dynamics to celestial mechanics. Time-frequency analysis is applicable to systems with any number of degrees of freedom.

Future applications of this method of analysis include the three-dimensional restricted three body problem, and rotational motion in molecules. We expect that the dynamics of these higher dimensional systems can be understood in terms of resonances produced by the coupling with the additional degrees of freedom.

The theoretical justification of the method will include a deeper understanding of the dependence of the analysis on the coordinate representation. Although in Hamiltonian systems there is a unique frequency vector for each quasiperiodic torus, transformations of variables might complicate the extraction of the basic frequencies.

But this is only the start. We believe that we have only just begun appreciating the power of this analytical tool.

Besides the previously mentioned applications, we are also planning to expand the use of this method for a broader class of problems: dissipative systems. The variation in time of the frequencies will still provide valuable information about the limit sets of trajectories of higher dimensional systems. This method is one of the very few that can extract the non-stationary properties of real physical systems.

By design, the extraction of instantaneous frequencies is not limited to Hamiltonian systems, not even to numerical trajectories. It can be applied to any time series. The possibilities of the time-frequency analysis of real data open the doors to a new field of study.

Appendix A

Appendix

A.1 Proof of Theorem 1

The structure of the proof is $1 \Rightarrow 2$, $2 \Rightarrow 3$ and $3 \Rightarrow 1$.

$1 \Rightarrow 2$. The Hilbert transform has a close relation with the Fourier transform. Remember, the Fourier transform of f is $\widehat{f}(\xi) = \mathrm{F}[f](\xi) = \int_{-\infty}^{\infty} f(t)e^{-2\pi i\xi t}dt$.

From the definition of convolution of functions, $f(t)*g(t) = \int_{-\infty}^{\infty} f(t-\lambda)g(\lambda)d\lambda$, the Hilbert transform can be expressed as

$$\nu(t) = H\,u(t) = \frac{1}{\pi t} * u(t) \quad \text{and } u(t) = H^{-1}\,\nu(t) = \frac{-1}{\pi t} * \nu(t).$$

Applying the convolution-multiplication theorem of the Fourier transform

$$\mathrm{F}[f * g] = \mathrm{F}[f]\ \mathrm{F}[g],$$

and since $\mathrm{F}[1/\pi t] = -i\,\mathrm{sgn}(\xi)$, we obtain that the Fourier transform of $H\,u(t)$ is

$$\mathrm{F}[H\,u](\xi) = \widehat{H\,u}(\xi) = -i\,\mathrm{sgn}(\xi)\mathrm{F}[u](\xi), \qquad \xi \in \mathbb{R}, \tag{A.1}$$

(where $\mathrm{sgn}(x) = 1$ if $x > 0$, 0 if $x = 0$, and -1 if $x < 0$).

From the last expression we deduce an alternative formula for the Hilbert

transform of $u \in L^1(\mathbb{R})$,

$$H\,u(t) = \mathrm{F}^{-1}\{-i\,\mathrm{sgn}(\xi)\mathrm{F}[u](\xi)\}.$$

Using (A.1) we can compute the Fourier transform of f,

$$\mathrm{F}[f](\xi) = \widehat{f}(\xi) = \widehat{u}(\xi) + i\,\widehat{\nu}(\xi) = (1 + \mathrm{sgn}(\xi))\widehat{u}(\xi), \tag{A.2}$$

and therefore, $\mathrm{F}[f](\xi) = 0$ for $\xi < 0$.

2 ⇒ 3. We need to prove that $f(\sigma)$ is an analytic function of the complex variable $\sigma = t + i\,\tau$ for $\tau \geq 0$. For this, we calculate the inverse Fourier transform of $\mathrm{F}[f]$ from Equation (A.2), and consider it as a function of the complex-time variable $\sigma = t + i\,\tau$:

$$f(\sigma) = \int_{-\infty}^{\infty} \widehat{f}(\xi)\, e^{i2\pi\sigma\xi}\, d\xi.$$

Since $\widehat{f}(\xi) = 0$ for $\xi < 0$, we can write

$$f(\sigma) = \int_{0}^{\infty} \widehat{f}(\xi)\, e^{i2\pi\sigma\xi}\, d\xi,$$

Replacing $s = -i2\pi\sigma$, we can write this integral as the Laplace transform of $\widehat{f}$,

$$\psi(s) = \int_{0}^{\infty} \widehat{f}(\xi)\, e^{-s\xi}\, d\xi$$

then $f(\sigma) = \psi(-i2\pi\sigma) = \psi(s)$.

We assume that $f(\xi)$ satisfies

$$|\widehat{f}(\xi)| \leq M\, e^{r\xi}, \qquad \xi \geq 0,$$

for some $M > 0$ and $r \leq 0$ (the proof works for any r, but for our purposes we take it negative).

Let ρ be such that $r < \rho \leq \mathrm{Re}(s)$. Then

$$|\widehat{f}(\xi)\, e^{-s\xi}| \leq M\, e^{r\xi} e^{\mathrm{Re}(s)\xi} \leq M\, e^{(r-\rho)\xi}.$$

We have that

$$\begin{aligned}\int_0^\infty |\widehat{f}(\xi)\, e^{-s\xi}|\, d\xi &\leq \lim_{T\to\infty} \int_0^T M\, e^{(r-\rho)\xi}\, d\xi \\ &= \lim_{T\to\infty} \frac{M}{\rho - r}\left(1 - e^{-(\rho-r)T}\right) = \frac{M}{\rho - r},\end{aligned}$$

and this implies that $\psi(s)$ is uniformly convergent in every compact subset of the right-half plane $\mathrm{Re}(s) > r$.

Since $\widehat{f}(\xi)\, e^{-s\xi}$ is analytic in s for each finite ξ, then we obtain that $\psi(s)$ is analytic for $\mathrm{Re}(s) > r$. (This is a consequence of a general theorem about the analyticity of functions defined as uniformly convergent integrals, see [14] p. 188).

But $f(\sigma) = \psi(s)$ with $s = -i2\pi\sigma = 2\pi(\tau + i\, t)$, then $f(t + i\,\tau)$ is analytic for $\tau > r/2\pi$. In particular, since we chose $r < 0$, $f(\sigma)$ is analytic in the upper half plane.

3 $\Rightarrow$ 1. We need some concepts regarding analytic functions. A useful representation of the function f analytic in a domain D is obtained with the Cauchy's integral formula,

$$f(z) = \frac{1}{2\pi i}\int_C \frac{f(\zeta)}{\zeta - z} d\zeta,$$

for any simple, closed, positively oriented curve C and every point z in the interior of C, provided that C and its interior belong entirely to D.

To obtain another representation that involves the restriction of f to the real axis, we consider the contour C as represented in Figure A.1.

We are assuming that $f(z)$ is analytic in the upper half plane, then for $t \in \mathbb{R}$, by Cauchy's theorem we have

$$\int_C \frac{f(\eta)}{\eta - t} d\eta \; = 0$$

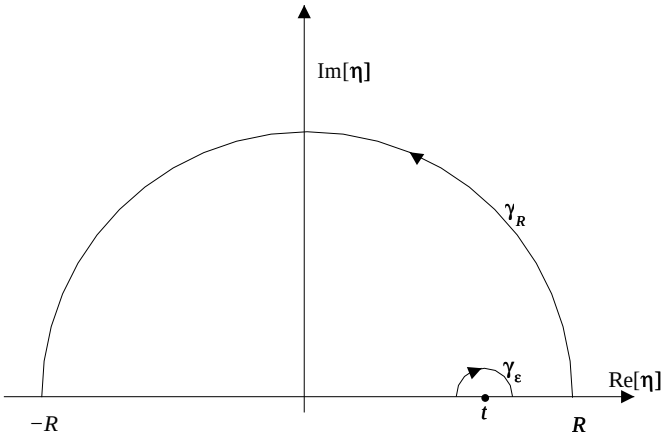

Figure A.1: Contour C.

(since t is not in the interior of C). Then we have

$$\int_C = \int_{\gamma_R} + \int_{\gamma_\epsilon} + \int_{-R}^{t-\epsilon} + \int_{t+\epsilon}^{R} = 0.$$

It can be shown that the integral on the half circle γ_R vanishes for $R \to \infty$. Also, as a consequence of the Residue theorem, we obtain

$$\lim_{\epsilon \to 0} \int_{\gamma_\epsilon} \frac{f(\eta)}{\eta - t} d\eta = -\pi i \text{Res}\left(\frac{f(\eta)}{\eta - t}, t\right) = -\pi i f(t).$$

Therefore, when $R \to \infty$ and $\epsilon \to 0$, the remaining two integrals are precisely the Cauchy principal value of the integral over the real line, denoted by $\text{P} \int_{-\infty}^{\infty} \frac{f(\eta)}{\eta - t} d\eta$. Therefore, we have

$$\text{P} \int_{-\infty}^{\infty} \frac{f(\eta)}{\eta - t} d\eta = \pi i f(t).$$

Substituting $f(\eta) = u(\eta, 0) + i\,\nu(\eta, 0)$ and equating the real and imaginary parts

on both sides of the previous equation, we obtain

$$\begin{aligned} u(t,0) =& \frac{1}{\pi}\mathrm{P}\int_{-\infty}^{\infty}\frac{\nu(\eta,0)}{\eta-t}d\eta, \\ \nu(t,0) =& -\frac{1}{\pi}\mathrm{P}\int_{-\infty}^{\infty}\frac{u(\eta,0)}{\eta-t}d\eta. \end{aligned}$$

These equations are equivalent to the definition of the Hilbert transform (2.10) and (2.11). Therefore, u and ν form a Hilbert pair, and the theorem follows.

A.2 The method of stationary phase

This method computes the asymptotic expansion of the integral

$$I = \int_{-\infty}^{\infty} M(t)\exp[i\lambda\phi(t)]dt.$$

Assume t_0 is a unique point (called stationary point) such that $\phi'(t_0) = 0$, and that $\phi(t_0) \neq 0$ and $\phi''(t_0) \neq 0$. Then we can expand ϕ and M in a Taylor series,

$$\begin{aligned} \phi(t) &= \phi(t_0) + \frac{1}{2}\phi''(t_0)(t-t_0)^2 + \dots \\ M(t) &= M(t_0) + M'(t_0) + \frac{1}{2}M''(t_0) + \dots \end{aligned}$$

and so

$$\begin{aligned} I \approx& M(t_0)\exp[i\lambda\phi(t_0)]\int_{-\infty}^{\infty}\exp\left[i\frac{\lambda}{2}\phi''(t_0)(t-t_0)^2\right]dt \\ &+ M'(t_0)\exp[i\lambda\phi(t_0)]\int_{-\infty}^{\infty}(t-t_0)\exp\left[i\frac{\lambda}{2}\phi''(t_0)(t-t_0)^2\right]dt \\ &+ \frac{1}{2}M''(t_0)\exp[i\lambda\phi(t_0)]\int_{-\infty}^{\infty}(t-t_0)^2\exp\left[i\frac{\lambda}{2}\phi''(t_0)(t-t_0)^2\right]dt \\ =& M(t_0)\exp[i\lambda\phi(t_0)]\sqrt{\frac{2\pi}{\lambda|\phi''(t_0)|}}\exp[i\,\mathrm{sgn}(\phi''(t_0))\pi/4] + O(\lambda^{-3/2}). \end{aligned}$$

Then, the contribution of an interval containing a stationary point is of the order $\lambda^{-1/2}$.

Note that if there is no stationary point in the interval $[\alpha, \beta]$, then integration by parts gives

$$\begin{aligned}\int_\alpha^\beta M(t)\exp[i\lambda\phi(t)]dt &= \frac{1}{i\lambda}\int_\alpha^\beta \frac{M(t)}{\phi'(t)}\frac{d}{dt}\left(e^{i\lambda\phi(t)}\right)dt \\ &= \frac{M(\beta)}{i\lambda\phi'(\beta)}e^{i\lambda\phi(\beta)} - \frac{M(\alpha)}{i\lambda\phi'(\alpha)}e^{i\lambda\phi(\alpha)} \\ &\quad -\frac{1}{i\lambda}\int_\alpha^\beta N(t)\,e^{i\lambda\phi(t)}dt,\end{aligned}$$

where $N(t) = \frac{d}{dt}\frac{M(t)}{\phi'(t)}$. Since N satisfies the same conditions as M, then the integral over an interval without stationary points is of the order $O(\lambda^{-1})$, as we see in the following expression,

$$\int_\alpha^\beta M(t)\exp[i\lambda\phi(t)]dt = \frac{M(\beta)}{i\lambda\phi'(\beta)}e^{i\lambda\phi(\beta)} - \frac{M(\alpha)}{i\lambda\phi'(\alpha)}e^{i\lambda\phi(\alpha)} + O(\lambda^{-2}).$$

In other words, the intervals with no stationary points contribute to the integral I in the order of λ^{-1}, and so they should be considered in the following term of the expansion.

A.3 Proof of Lemma 1

To compute the analytic signal $Z_u(t)$ associated with $u(t)$, we use the formula (A.2) relating the Fourier transform of Z_u with the Fourier transform of u,

$$Z_u(t) = \mathrm{F}^{-1}\{2\Theta(\xi)\mathrm{F}[u](\xi)\},$$

where Θ is the step function, $\Theta(t) = 1$ for $t \geq 0$, and zero otherwise.

In the computation of the Fourier transform of u, we use the stationary phase

method to obtain

$$\begin{aligned}
\mathrm{F}[u](\xi) =& \mathrm{F}\{A(t)\cos[\lambda\phi(t)]\} \\
=& \int_{-\infty}^{\infty} \frac{A(t)}{2}\left(e^{i\lambda\phi(t)} + e^{-i\lambda\phi(t)}\right) e^{i2\pi\xi t} dt \\
=& \int_{-\infty}^{\infty} \frac{A(t)}{2} e^{i(\lambda\phi(t)-2\pi\xi t)} dt + \int_{-\infty}^{\infty} \frac{A(t)}{2} e^{i(-\lambda\phi(t)-2\pi\xi t)} dt \\
=& \frac{A(t_0)}{2} e^{i(\lambda\phi(t_0)-2\pi\xi t_0)} e^{i\pi/4} \sqrt{\frac{2\pi}{\lambda\phi''(t_0)}} \\
&+ \frac{A(s_0)}{2} e^{i(-\lambda\phi(s_0)-2\pi\xi s_0)} e^{-i\pi/4} \sqrt{\frac{2\pi}{\lambda\phi''(s_0)}},
\end{aligned} \tag{A.3}$$

where $t_0 = t_0(\xi)$ and $s_0 = s_0(\xi)$ satisfy

$$\lambda\phi'(t_0) - 2\pi\xi = 0, \quad \lambda\phi'(s_0) + 2\pi\xi = 0,$$

and we are assuming that $\phi''(t_0) > 0$ and $\phi''(s_0) > 0$.

Now, we multiply the last expression in A.3 by $2\Theta(\xi)$ and compute the inverse Fourier transform using again the stationary phase method. The first integral to compute is

$$I_1 = \int_0^{\infty} A(t_0) \sqrt{\frac{2\pi}{\lambda\phi''(t_0)}} e^{i\Phi(\xi)} d\xi$$

with

$$\Phi(\xi) = \lambda\phi(t_0) - 2\pi\xi t_0 + \pi/4 + 2\pi t\xi.$$

This integral has a stationary point if

$$\Phi'(\xi) \;=\; (\lambda\phi'(t_0) - 2\pi\xi)t_0'(\xi) - 2\pi t_0 + 2\pi t \;=\; 0,$$

but the quantity in parentheses is zero for the definition of t_0. Therefore, if $t = t_0 = t_0(\xi_0)$ is the stationary point, the integral can be approximated as

$$I_1 = A(t)\sqrt{\frac{2\pi}{\lambda\phi''(t)}} e^{i\Phi(\xi_0)} e^{i\mathrm{sgn}(\Phi''(\xi_0))\pi/4} \frac{1}{2} \sqrt{\frac{2\pi}{|\Phi''(\xi_0)|}} + O(\lambda^{-3/2}).$$

Using the definition of t_0, we obtain that $t_0'(\xi_0) = \frac{2\pi}{\lambda\phi''(t_0)}$, and then

$$\begin{aligned}
\Phi(\xi_0) =& \lambda\phi(t) + \pi/4, \qquad \text{and} \\
\Phi''(\xi_0) =& \left(\lambda\phi''(t_0)t_0'(\xi_0) - 2\pi\right) t_0'(\xi_0) + (\lambda\phi'(t_0) - 2\pi\xi)t_0''(\xi_0) - 2\pi t_0'(\xi_0) \\
=& \lambda\phi''(t_0)[t_0'(\xi_0)]^2 - 4\pi t_0'(\xi_0) \\
=& \frac{-4\pi^2}{\lambda\phi''(t_0)}.
\end{aligned}$$

When evaluating at $t = t_0$, the integral is

$$I_1 = \frac{1}{2}A(t)e^{i\lambda\phi(t)} + O(\lambda^{-3/2}).$$

The second integral can be treated in the same way to obtain the desired result.

A.4 Computation of the instantaneous frequency. A pseudocode

For a time series z, we compute a series corresponding to the evolution in time of the fundamental frequency ω. The frequency is obtained from the scale producing the maximum modulus of the wavelet transform at each time point. This was done with the routine `Wavelet`.

Description of the `Wavelet` routines.

Routine `Wavelet`.

For each time point `b`:

First it computes two values of the scale `a1`, `a2` that approximate the largest modulus of the wavelet transform in a range of scales. It calls the function `abswav` to evaluate the modulus of the wavelet transform at given values of time `b` and scale `a`.

`a1` and `a2` are the input for the subroutine `fmnbrak` that brackets the maximum of `abswav`.

Then the subroutine `fmaxim` isolates the scale `a` that produces the maximum of `abswav`;

This scale is related to the frequency of `z` about the time `b` by $\omega = cons/a$.

The frequency is stored in `omega`. The information of `omega(j)` is used to obtain `omega(j+1)`, accelerating the procedure.

input:

`ti`, array that holds the time points of the time series,

`z`, array containing a complex time series evaluated at each time point in `ti`: `z(j)` is a point of the time series that corresponds to time `ti(j)`,

`n`, number of points in the time series.

output:

`omega`, array containing the frequency value at each point `b` in `ti`.

parameters:

`cons`, constant that relates the frequency with the scale: $\omega = cons/a$.

Function `Abswav`.

It computes the modulus of the continuous wavelet transform of z:

$$L_\psi z(a,b) \;=\; \langle z, \psi_{a,b} \rangle \;=\; a^{-1/2} \int_{-\infty}^{\infty} z(t) \overline{\psi} \left(\frac{t-b}{a} \right) dt.$$

The Morlet-Grossman wavelet is

$$\psi(t) = \frac{1}{\sigma\sqrt{2\pi}}\, e^{2\pi i \lambda t}\, e^{-t^2/2\sigma^2}.$$

The modulus of the continuous wavelet transform is computed at a given scale `a` and time `b`, for the complex time series `z` evaluated at the points in `ti`. The subroutine uses the Simpson formula for numerical integration of the product between z and $\overline{\psi}_{ab}$, over the time interval $[b-3\sqrt{2}\sigma a\,,\; b+3\sqrt{2}\sigma a]$ (effective support of the Morlet-Grossman wavelet.)

input:

`a`, scale,

`b`, time,

`ti`, `z`, `n`, time points, values and number of points of the time series.

output:

`abswav`, modulus of the wavelet transform.

parameters:

`sigma`, `lambda`, variance and frequency of the Morlet-Grossman wavelet.

Subroutine `fmnbrak`.

Routine that brackets the maximum of a function. Given two initial values a_1, a_2, the routine searches for the uphill direction and returns new points a_1, a_2, a_3 that bracket the maximum (i.e., $a_1 < a_2 < a_3$ and $f(a_2)$ is greater than both $f(a_1)$ and $f(a_3)$.)

It is used to find points of scale `a` that bracket the maximum of `abswav` at each time `b`.

input:

`a1`, `a2`, initial values of the scale a,

`b`, time,

`ti`, `z`, `n`, time points, values and number of points of the time series.

output:

`a1`, `a2`, `a3`, points of the scale that bracket the maximum,

`f1`, `f2`, `f3`, evaluation of `abswav` at the points `a1`, `a2`, `a3`.

Subroutine `fmaxim`.

Routine that finds the maximum of a function given three abscissas that bracket the maximum. This routine isolates the maximum to a fractional precision using Brent's method [42].

It finds the scale `a` producing the maximum modulus of the wavelet transform `abswav` for the time series `z` at each time point `b` with tolerance 10^{-8}.

input:

`a1`, `a2`, `a3`, points that bracket the maximum,

`b`, time,

`ti`, `z`, `n`, time points, values and number of points of the time series.

output:

`x`, point where the maximum is located,

`fx`, value of the maximum.

A.5 Reduction to two degrees of freedom of the Baggott Hamiltonian

The following transformations of variables were performed first to obtain a normal form of the Hamiltonian (3.1), and then to reduce the system to two degrees of freedom using the Polyad number (3.2).

With complex coordinates defined by the canonical transformation

$$z_k = \sqrt{2I_k}e^{i\theta_k}, \qquad \overline{z}_k = \sqrt{2I_k}e^{-i\theta_k},$$

the Hamiltonian function (3.1) can be rewritten as

$$H = H_0 + H_1 + H_2,$$

where

$$\begin{aligned}
H_0 =& \frac{\Omega_s}{2}(|z_1|^2 + |z_2|^2) + \frac{\Omega_b}{2}|z_3|^2 + \frac{\beta_{12}}{2}Re(z_1\overline{z}_2),\\
H_1 =& \frac{\beta_{sb}}{2^{3/2}}[Re(z_1\overline{z}_3^2) + Re(z_2\overline{z}_3^2)],\\
H_2 =& \frac{\alpha_s}{4}(|z_1|^4 + |z_2|^4) + \frac{\alpha_b}{4}|z_3|^4 + \frac{\varepsilon_{ss}}{4}|z_1|^2|z_2|^2 + \frac{\varepsilon_{sb}}{4}|z_3|^2(|z_1|^2 + |z_2|^2) +\\
& \Big(\frac{\lambda'}{2}(|z_1|^2 + |z_2|^2) + \frac{\lambda''}{2}|z_3|^2\Big)\frac{1}{2}Re(z_1\overline{z}_2) +\\
& \frac{\beta_{22}}{4}Re[(z_1\overline{z}_2)^2].
\end{aligned}$$

And the Equation (3.2) in this coordinates is

$$P = |z_1|^2 + |z_2|^2 + \frac{|z_3|^2}{2}.$$

In order to diagonalize the quadratic terms of this Hamiltonian, the following symplectic change of coordinates is defined:

$$\begin{aligned} z_1 &= \frac{1}{\sqrt{2}}(x_1 + x_2), \qquad & \overline{z}_1 &= \frac{1}{\sqrt{2}}(\overline{x}_1 + \overline{x}_2), \\ z_2 &= \frac{1}{\sqrt{2}}(x_1 - x_2), \qquad & \overline{z}_2 &= \frac{1}{\sqrt{2}}(\overline{x}_1 - \overline{x}_2), \\ z_3 &= x_3, & \overline{z}_3 &= \overline{x}_3. \end{aligned}$$

The expressions in the Hamiltonian become

$$\begin{aligned} H_0 =& (\frac{\Omega_s}{2} + \frac{\beta_{12}}{4})|x_1|^2 + (\frac{\Omega_s}{2} - \frac{\beta_{12}}{4})|x_2|^2 + \frac{\Omega_b}{2}|x_3|^2, \\ H_1 =& \frac{\beta_{sb}}{2}[Re(x_1\overline{x}_3^2)], \\ H_2 =& \frac{\alpha_s}{8}[(|x_1|^2 + |x_2|^2)^2 + 4(Re(x_1\overline{x}_2))^2] + \frac{\varepsilon_{ss}}{16}[(|x_1|^2 + |x_2|^2)^2 - \\ & 4(Re(x_1\overline{x}_2))^2] + \frac{\varepsilon_{sb}}{4}|x_3|^2(|x_1|^2 + |x_2|^2) + \frac{\alpha_b}{4}|x_3|^4 + \\ & \big(\frac{\lambda'}{2}(|x_1|^2 + |x_2|^2) + \frac{\lambda''}{2}|x_3|^2\big)\frac{1}{4}(|x_1|^2 - |x_2|^2) + \\ & \frac{\beta_{22}}{16}[(|x_1|^2 - |x_2|^2)^2 - 4(Im(x_1\overline{x}_2))^2], \end{aligned}$$

and

$$P = |x_1|^2 + |x_2|^2 + \frac{|x_3|^2}{2}.$$

Action-angle variables can be defined by

$$x_k = \sqrt{2J_k}e^{i\phi_k}, \qquad \overline{x}_k = \sqrt{2J_k}e^{-i\phi_k},$$

that yield to the following form of the Hamiltonian function:

$$H = H_0 + H_1 + H_2,$$

$$\begin{aligned}
H_0 =& a_1 J_1 + a_2 J_2 + a_3 J_3, \\
H_1 =& b_1 J_1^{1/2} J_3 \cos(\phi_1 - 2\phi_3), \\
H_2 =& b_2 J_1 J_2 \cos 2(\phi_1 - \phi_2) + \\
& b_3 J_1^2 + b_4 J_1 J_2 + b_5 J_2^2 + b_6 J_1 J_3 + b_7 J_2 J_3 + b_8 J_3^2,
\end{aligned}$$

where the coefficients are given by

$$\begin{aligned}
a_1 &= \Omega_s + \tfrac{\beta_{12}}{2} & b_1 &= \sqrt{2}\beta_{sb} \\
a_2 &= \Omega_s - \tfrac{\beta_{12}}{2} & b_2 &= \alpha_s - \tfrac{\varepsilon_{ss}}{2} + \tfrac{\beta_{22}}{2} \\
a_3 &= \Omega_b & b_3 &= \tfrac{\alpha_s}{2} + \tfrac{\varepsilon_{ss}}{4} + \tfrac{\lambda'}{2} + \tfrac{\beta_{22}}{4} \\
& & b_4 &= 2\alpha_s - \beta_{22} \\
& & b_5 &= \tfrac{\alpha_s}{2} + \tfrac{\varepsilon_{ss}}{4} - \tfrac{\lambda'}{2} + \tfrac{\beta_{22}}{4} \\
& & b_6 &= \varepsilon_{sb} + \tfrac{\lambda''}{2} \\
& & b_7 &= \varepsilon_{sb} - \tfrac{\lambda''}{2} \\
& & b_8 &= \alpha_b.
\end{aligned}$$

The Polyad number is expressed analogously:

$$P = 2(J_1 + J_2) + J_3.$$

The system in this form also exhibits 1:1 and 2:1 resonance couplings, but it is no more symmetric with respect to the indices. However, we have reduced the number of terms in the Hamiltonian and we are left with a diagonal quadratic part. Actually, this form corresponds to the so called "normal mode" Hamiltonian by Baggott [5].

We can obtain integrable limits of this Hamiltonian if we neglect either the

coefficient b_1 or b_2, i.e., when only one resonance coupling is considered. In this case, the system can be reduced to a 1-dof Hamiltonian, therefore integrable. For instance, the truncated Hamiltonian $H = H_0 + H_2$ is completely integrable with first integrals given by H, J_3 and $J_1 + J_2$; this is what we expect for the case of a single resonance.

To reduce the system to two degrees of freedom, we use the symplectic linear transformation $(J, \phi) \to (N, \psi)$ defined by

$$\psi = U\phi, \qquad N = (U^T)^{-1}J,$$

where

$$U = \begin{pmatrix} 1 & -1 & 0 \\ 1 & 0 & -2 \\ 0 & 0 & 1 \end{pmatrix}, \qquad (U^T)^{-1} = \begin{pmatrix} 0 & -1 & 0 \\ 1 & 1 & 0 \\ 2 & 2 & 1 \end{pmatrix}.$$

We obtain $N_3 = P$, the Polyad number. Then we are left with a two-degree-of-freedom system in the variables $(N_1, N_2, \psi_1, \psi_2)$. The Hamiltonian can be written as follows:

$$\begin{aligned} H &= H_0 + H_1 + H_2, \\ H_0 &= \alpha_1 N_1 + \alpha_2 N_2 + \alpha_3, \\ H_1 &= \beta_1 \sqrt{N_1 + N_2}(-2N_2 + P)\cos\psi_2, \\ H_2 &= -\beta_2(N_1^2 + N_1 N_2)\cos 2\psi_1 + \beta_3 N_1^2 + \beta_4 N_1 N_2 + \beta_5 N_2^2. \end{aligned}$$

Note that since $J_1 > 0$ and $J_2, J_3 \geq 0$, it turns out that the feasible region in the new variables is given by $0 \leq -N_1 < N_2 \leq P/2$.

Bibliography

[1] V.I. Arnold. Proof of a theorem by A.N. Kolmogorov on the persistence of quasiperiodic motions under small perturbations of the Hamiltonian. *Russian Math. Surveys*, 18(5):9–36, 1963.

[2] V.I. Arnold. Small denominators and problems of stability of motion in classical and celestial mechanics. *Russian Math. Surveys*, 18(6):85–191, 1963.

[3] V.I. Arnold. On the instability of dynamical systems with many degrees of freedom. *Sov. Math. Dokl.*, 5(3):581–585, 1964.

[4] V.I. Arnold. *Mathematical methods of classical mechanics*. Springer-Verlag, New York, 2nd. edition, 1989.

[5] J.E. Baggott. Normal modes and local modes in H_2X: beyond the x, K relations. *Mol. Phys.*, 65:739–749, 1988.

[6] J. Binney and D. Spergel. Spectral stellar dynamics. *Astrophys. J.*, 251(1):308–321, 1982.

[7] J. Binney and D. Spergel. Spectral stellar dynamics-II. The action integrals. *Mon. Not. R. Astron. Soc.*, 206:159–177, 1984.

[8] H.W. Broer, G.B. Huitema, and M.B. Sevryuk. *Quasi-periodic motions in families of dynamical systems*. Springer-Verlag, Berlin, 1996.

[9] R. Carmona, W. Hwang, and B. Torrésani. *Practical time-frequency analysis: Gabor and Wavelet transforms with an implementation in S*. Academic Press, San Diego, 1998.

[10] D. Carter and P. Brumer. Intramolecular dynamics and nonlinear mechanics of model OCS. *J. Chem. Phys.*, 77(7):4208–4221, 1982. Erratum: *J. Chem. Phys.* (78)4, 1983.

[11] G. Contopoulos and N. Voglis. A fast method for distinguishing between ordered and chaotic orbits. *Astron. Astrophys.*, 317(1):73–81, 1997.

[12] I. Daubechies. *Ten lectures on wavelets*. SIAM, Philadelphia, 1992.

[13] D. Delprat, B. Escudié, P. Guillemain, R. Kronland-Martinet, P. Thamitchian, and B. Torrésani. Asymptotic wavelet and Gabor analysis: Extraction of instantaneous frequencies. *IEEE T. Inform. Theory*, 38(2):644–664, 1992.

[14] J.W. Dettman. *Applied complex variables*. Macmillan, New York, 1965.

[15] A. Foord, J.G. Smith, and D.H. Whiffen. An anharmonic force field for carbonyl sulphide. *Mol. Phys.*, 29(6):1685–1704, 1975.

[16] F. Forstneric. Actions of $(\mathbb{R}, +)$ and $(\mathbb{C}, +)$ on complex manifolds. *Math. Z.*, 223:123–153, 1996.

[17] C. Froeschlé and E. Lega. Twist angles: A method for distinguishing islands, tori and weak chaotic orbits. Comparison with other methods of analysis. *Astron. Astrophys.*, 334:355–362, 1998.

[18] D. Gabor. Theory of communications. *J. IEE*, 93:429–57, 1946.

[19] C. Gasquet and P. Witomski. *Fourier analysis and applications*. Springer, New York, 1998.

[20] M.C. Gutzwiller. *Chaos in classical and quantum mechanics*. Springer, New York, 1991.

[21] S.L. Hahn. *Hilbert transforms in signal processing*. Artech House, Boston, 1996.

[22] S. Keshavamurthy and G. Ezra. Eigenstate assignments and the quantum-classical correspondence for highly excited vibrational states of the Baggott H_2O Hamiltonian. *J. Chem. Phys.*, 107:156–179, 1997.

[23] W.S. Koon, M.W. Lo, J.E. Marsden, and S.D. Ross. Heteroclinic connections between periodic orbits and resonance transitions in celestial mechanics. *CHAOS*, 10(2):427–469, 2000.

[24] J. Laskar. The chaotic motion of the solar system: A numerical estimate of the size of the chaotic zones. *Icarus*, 88:226–291, 1990.

[25] J. Laskar. Frequency analysis for multi-dimensional systems. Global dynamics and diffusion. *Physica D*, 67:257–281, 1993.

[26] J. Laskar. Introduction to frequency map analysis. C. Simo (Ed.) *Hamiltonian systems with three or more degrees of freedom*. Kluwer, 1999.

[27] J. Laskar, C. Froeschlé, and A. Celletti. The measure of chaos by the numerical analysis of the fundamental frequencies. Application to the standard mapping. *Physica D*, 56:253–269, 1992.

[28] A. Laubereau and W. Kaiser. Vibrational dynamics of liquids and solids investigated by picosecond light pulses. *Rev. Mod. Phys*, 50:607–665, 1978.

[29] A.J. Lichtenberg and M.A. Lieberman. *Regular and chaotic dynamics*. Springer - Verlag, New York, 1983.

[30] J.C. Losada, J.M. Estebaranz, and R.M. Benito. Local frequency analysis and the structure of classical phase space of the LiNC/LiCN molecular system. *J. Chem. Phys.*, 108:63–71, 1998.

[31] P.J. Loughlin and B. Tacer. On the amplitude- and frequency-modulation decomposition of signals. *J. Acoust. Soc. Am.*, 100(3):1594–1601, 1996.

[32] Z. Lu and M.E. Kellman. Phase space structure of triatomic molecules. *J. Chem. Phys.*, 107:1–15, 1997.

[33] C. Martens, M. Davis, and G. Ezra. Local frequency analysis of chaotic motion in multidimensional systems: energy transport and bottlenecks in planar OCS. *Chem. Phys. Lett.*, 142:519–528, 1987.

[34] C. Martens and G. Ezra. Classical and semiclassical mechanics of strongly resonant systems -A Fourier transform approach. *J. Chem. Phys.*, 86(1):279–307, 1987.

[35] J.D. Meiss and E. Ott. Markov-tree model of intrinsic transport in Hamiltonian-systems. *Phys. Rev. Lett.*, 55(25):2741–2744, 1985.

[36] J.D. Meiss and E. Ott. Markov tree model of transport in area-preserving maps. *Physica D*, 20(2-3):387–402, 1986.

[37] J. Moser. On the theory of quasiperiodic motions. *SIAM Review*, 8(2):145–172, 1966.

[38] P.M. Oliveira and V. Barroso. Instantaneous frequency of multicomponent signals. *IEEE Signal Proc. Let.*, 8(4):81–83, 1999.

[39] J.C. Owrutsky, D. Raftery, and R.M. Hochstrasser. Vibrational-relaxation dynamics in solutions. *Annu. Rev. Phys. Chem.*, 45:519–555, 1994.

[40] B. Picinbono. On instantaneous amplitude and phase of signals. *IEEE T. Signal Proc.*, 45(3):552–560, 1997.

[41] J.B. Pollack, J.B. Dalton, and *et al.* Near infrared light from Venus night side -A spectroscopic analysis. *Icarus*, 103(1):1–42, 1993.

[42] W.H. Press, S.A. Teukolsky, W.T. Vetterling, and B.P. Flannery. *Numerical recipes in Fortran*. Cambridge University Press, Cambridge, 1992.

[43] J.H. Seinfeld and S.N. Pandis. *Atmospheric chemistry and physics: from air pollution to climate change*. John Wiley, New York, 1998.

[44] C.L. Siegel and J. Moser. *Lectures on celestial mechanics*. Springer-Verlag, Berlin, 1971.

[45] V. Szebehely. *Theory of orbits*. Academic Press, New York, London, 1967.

[46] K. Tsiganis, H. Varvoglis, and J.D. Hadjidemetriou. Stable chaos in the 12:7 mean motion resonance and its relation to the stickiness effect. *Icarus*, 146:240–252, 2000.

[47] T. Uzer. Theories of intramolecular energy transfer. *Phys. Rep.*, 199(2):73–146, 1991.

[48] D. Vakman. On the analytic signal, the Teager-Kaiser energy algorithm, and other methods for defining amplitude and frequency. *IEEE T. Signal Proc.*, 44(4):791–797, 1996.

[49] L.V. Vela-Arevalo and S. Wiggins. Time-frequency analysis of classical trajectories of polyatomic molecules. *Int. J. Bifurcat. Chaos*, 11(5):1359–1380, 2001.

[50] J. Ville. Théorie et applications de la notion de signal analytique. *Cables Trans.*, 2:61–74, 1948.

[51] J. von Milczewski, D. Farrelly, and T. Uzer. Frequency analysis of 3D electronic 1/r dynamics: Turning between order and chaos. *Phys. Rev. Lett.*, 78:1436–1439, 1997.

[52] J. von Milczewski and T. Uzer. Mapping multidimensional dynamics using frequency analysis. D.L. Thompson (Ed.) *Modern methods for multidimensional dynamics computations in chemistry*, World Scientific, Singapore, 190-200, 1998.

[53] D. Wei and A.C. Bovik. On the instantaneous frequencies of multicomponent AM-FM signals. *IEEE Signal Proc. Lett.*, 5(4):84–86, 1998.

[54] L. Xiao and M.E. Kellman. Unified semiclassical dynamics for molecular resonance spectra. *J. Chem. Phys.*, 90:6086–6098, 1989.


CALIFORNIA INSTITUTE OF TECHNOLOGY
1891